

André Palóczy Filho

**Intrusions of South Atlantic Central Water
on the Espírito Santo Basin shelf (18°S–22°S, Brazil)**

A thesis submitted in partial fulfillment of the requirements for the degree of Master of Sciences in Oceanography, with emphasis in Physical Oceanography, *Instituto Oceanográfico, Universidade de São Paulo*.

Advisor:

Prof. Ilson Carlos Almeida da Silveira (IO/USP)

São Paulo

2015

Universidade de São Paulo

Instituto Oceanográfico

Intrusions of South Atlantic Central Water on the Espírito Santo Basin shelf (18°S–22°S, Brazil)

(Corrected version)

by

André Palóczy Filho

A thesis submitted in partial fulfillment of the requirements for the degree of
Master of Sciences in Oceanography, with emphasis in Physical Oceanography,
Instituto Oceanográfico, Universidade de São Paulo.

Evaluated in ____ / ____ / _____

Prof. Dr.

Grade

Prof. Dr.

Grade

Prof. Dr.

Grade

*“The scientists do not study nature because it is useful;
they study it because they delight in it, and they delight
in it because it is beautiful.”*

Henri Poincaré

Acknowledgements

My most heartfelt thanks go to my advisor, dear friend and primary mentor Professor Ilson Silveira. My achievements would not have been possible without his scientific guidance and energetic encouragement throughout the years. I feel truly fortunate and thankful for having been trained under his phenomenological approach to physical oceanography and to have been able to make that the core of my own passionate view of science. Thank you so much for everything you made possible and for being there for me at all times.

I am deeply thankful to Professor Kenneth Brink, who generously received me as a guest student at WHOI, and effectively co-advised this research. His encouraging and inspiring mentoring have helped shape the science student I am today. I am truly indebted to him for his kindness in receiving me in his office nearly every day of my time at WHOI, for his great ideas, and illuminating comments. I also thank him for letting me sit on his Fall course on data analysis and for encouraging me to present part of this work on a WHOI COFDL talk. My sincere thanks for making this rewarding experience possible.

I am indebted to many other people at WHOI. In particular, I thank Deepak Cherian for a great deal of numerical modeling-related help and for great scientific comments and suggestions, as well as other students of the MIT/WHOI Joint Program. Thanks are also due to Ke Chen for helpful suggestions with the model implementation and diagnosis. Technical support from the CIS helpdesk with the WHOI cluster was fundamental in running the numerical experiments. I also gratefully acknowledge helpful advice and suggestions from Professors Glen Gawarkiewicz, Anthony Kirincich, Magdalena Andres, Joseph Pedlosky and Steven Lentz. I am especially grateful to Professor Lentz for the dense and mind-bending conversations.

A special thanks to the entire WHOI community for nurturing such a welcoming and open environment. It makes so much difference. Living next door (literally) to Walsh Cottage for six months and being able to sit in Summer GFD lectures freely was not a privilege I could ever have dreamed of when I first visited Woods Hole in Winter/2012.

I gratefully acknowledge help regarding ROMS momentum balance diagnosis from Professor Jianping Gan (HKUST/China), during his visit to WHOI in Summer/2014 and later.

I Thank Professor Wilton Arruda (UFRJ/Brazil) for providing the outputs from the HYCOM numerical experiment and for much helpful input on its analysis. I also acknowledge his comments and suggestions on the simplified ROMS experiments and on the ATW analytical model.

Thanks to Professor Alberto Piola (SHN/Argentina), for helpful suggestions regarding the analyses of the observations and for the exciting lectures during the XIII Austral Summer Institute course "Circulation and Water Masses in the Southwest Atlantic", held in January/2013 at UdeC/Chile.

I am really fortunate to have had excellent instructors, and it is a pleasure to acknowledge their dedicated work. In particular, I thank Professors Belmiro Castro, Marcelo Dottori, Paulo Polito, Olga Sato, Alberto Piola, Kenneth Brink and Ilson Silveira for teaching me so much. Thanks are also due to Professors Márcia Bicego and Sueli Godoi for the encouragement throughout my undergraduate and graduate years at IO/USP.

I am also happy to thank all my lab colleagues and friends from the Ocean Dy-

namics Laboratory (LaDO–IO/USP) for many pleasant science and non–science moments. Special thanks go to César Rocha, Rafael Soutelino, Hermínio Folini, Filipe Fernandes, Ronaldo Mitsuo, Leandro Ponsoni, Leilane Passos, Márcio Yamashita, Pedro Calixto, Filipe Pereira, Ágata Braga, Hélio Almeida, Gilberto Watanabe, Dante Campagnoli, Iury Simões, Ana Paula Krelling and Tiago Biló.

A warm thanks also to my dear friends Hanna Vale, Renato Oliveira, Iole Orselli, Quek Yew Aun, Santiago Benavides, Laís Farina, Filipe Galiforni, Juliana Damasceno, Guilherme Castelão, Bia Melo, Olavo Marques, Natasha Hoff and Nancy Kazumi.

Administrative support from IO/USP and WHOI is also gratefully acknowledged.

The datasets used in this work come from a number of sources. Despite having participated in only one (AMBES 09, October/2012) of the five mesoscale cruises whose data were used in the present work, I gratefully acknowledge the hard work done by the crews of R/V *Wladimir Besnard* and R/V *Seward Johnson* in obtaining them. CTD and ADCP data from the AMBES 09 and AMBES 10 cruises was kindly provided by *Petróleo Brasileiro S/A* (PETROBRAS). The Abrolhos 1, Abrolhos 2 and PRO–ABROLHOS cruise data were obtained from the LaDO–IO/USP historical database. The World Ocean Atlas 2013 climatological data (WOA13) was downloaded from <https://www.nodc.noaa.gov/OC5/woa13/woa13data.html>. The SRTM30–plus bottom topography dataset was downloaded from http://topex.ucsd.edu/WWW_html/srtm30_plus.html. The Sea Surface Temperature climatology from the Pathfinder Project v5.0 was obtained at <http://www.nodc.noaa.gov/SatelliteData/pathfinder4km/>. The *Multiple–Satellite Blended Sea Surface Winds* product was downloaded from <http://www.ncdc.noaa.gov/thredds/dodsC/oceanwinds>.

Many thanks also go to my uncle Antônio, my aunt Cristina, and to my grandparents Maria and José for their love and friendship.

Finally, I profoundly and warmly thank my parents André Palóczy and Cristiane Ortiz for always being there for me, for their loving support, and for the encouragement and friendship that made this work possible.

This work is part of the “Characterization of the physical oceanography of the Espírito Santo Basin” Project (*Caracterização da Oceanografia Física da Baía do Espírito Santo*, AMBES), sponsored by *Petróleo Brasileiro S/A* (PETROBRAS).

Financial support for this work was provided by the São Paulo Research Foundation (*Fundação de Amparo à Pesquisa do Estado de São Paulo*, FAPESP), under fellowships 2013/11465-4 (MSc scholarship) and 2014/03451-6 (BEPE Research Internship Abroad scholarship).

Contents

	Page
Acknowledgements	i
List of figures	v
List of tables	xi
List of Acronyms	xii
Abstract	xiii
Resumo	xiv
1 Introduction to the thesis	1
1.1 On the thesis structure	1
1.2 Regional overview	1
1.3 The Taylor–Proudman constraint	4
1.4 Thesis hypotheses and objectives	7
2 Pathways and mechanisms of offshore water intrusions on the Espírito Santo Basin (18°S–22°S, Brazil)	9
Abstract	9
2.1 Introduction	10
2.2 Datasets	14
2.2.1 <i>In situ</i> quasi–synoptic hydrographic and velocity data	14
2.2.2 Climatological hydrographic data	15
2.2.3 Satellite data	15
2.3 Numerical models	15
2.3.1 Numerical and parametric modeling setup	15
2.3.2 Process–oriented simplified experiments	20
2.3.3 Realistic experiment	21
2.4 South Atlantic Central Water intrusion pathways	22
2.4.1 Observational setting	22
2.4.2 Model kinematics of SACW intrusions	27
2.5 Along–isobath momentum balance	31
2.5.1 Depth–dependent momentum balance along the shelf edge	31
2.5.2 Depth–averaged momentum balance	36
2.6 Deep–ocean forcing mechanisms	42
2.6.1 Pycnocline uplifting linked to the Brazil Current mean jet	42
2.6.2 Shelf encroaching of the Brazil Current by inertial overshooting	44
2.6.3 Meridional pressure gradient induced by the β effect	47
2.7 Summary and conclusions	51

3	Steady cross–shelf circulation induced by a periodic slope current: Analytical and numerical solutions for the Tubarão Bight (Southeast Brazil)	55
	Abstract	55
3.1	Introduction	56
3.2	The analytical model	57
3.3	Comparison with primitive–equation numerical solutions	64
3.4	Conclusions	68
4	Final remarks	69
4.1	Thesis summary	69
4.2	Future work	71

List of Figures

- 1.1 Schematic representation of the upper ocean circulation in the South Atlantic. The red arrow indicates the location of the Espírito Santo Basin (ESB) in the western boundary of the South Atlantic Subtropical Gyre (SASG). Adapted from *Talley et al. (2011)*. Original version available at <http://booksite.elsevier.com/DPO/>. 3
- 1.2 Schematic representation of the vertical structure of western boundary currents and water masses in the South Atlantic Subtropical Gyre (SASG). SEC, BC, NBUC, NBC, IWBC and DWBC stand for South Equatorial Current, Brazil Current, North Brazil Undercurrent, North Brazil Current, Intermediate Western Boundary Current and Deep Western Boundary Current, respectively. TW, SACW, AAIW and NADW stand for Tropical Water, South Atlantic Central Water, Antarctic Intermediate Water and North Atlantic Deep Water, respectively. The Espírito Santo Basin (ESB) is located in the northern end of the Southeast Sector (20°S–28°S) of the Brazil Current System, approximately at the bifurcation latitude of the SEC at pycnocline levels. Courtesy: Gilberto Watanabe (IO/USP). Modified from the original version published by *Soutelino et al. (2013)*. 4
- 2.1 Topographic map of the Espírito Santo Basin (ESB). The upper-left map insert marks the location of the study area off the coast of South America (red rectangle). The locations marked by the black stars are Cape Frio (CF), Cape São Tomé (CST), Marataízes (MRT), Vitória (V), Aracruz (ACZ) and Caravelas (CRV). The orange polygon indicates the limits of the ESB. The red line indicates the domain of the Tubarão Bight (TB). The gray lines are the 30 m, 500 m, 1000 m, 2000 m, 3000 m and 4000 m isobaths, and the black line is the 100 m isobath, derived from the 30-arcsecond SRTM30-plus dataset (updated from *Smith & Sandwell, 1997*). 13
- 2.2 Schematic representation of the regional circulation in the Espírito Santo Basin. The acronyms RCE, AE and VE stand for Royal-Charlotte Eddy, Abrolhos Eddy and Vitória Eddy, respectively. The black arrows indicate the prevailing flow pattern, and are not to scale. Adapted from *Lopes & Castro (2013)*. 14
- 2.3 Representation of the *in situ* synoptic datasets within the study region. The upper-left map insert marks the location of the study area off the coast of South America (red rectangle). The locations marked by the black stars are as in [Figure 2.1](#). The black lines are the 100 m and 2000 m isobaths, derived from the 30-arcsecond SRTM30-plus dataset (updated from *Smith & Sandwell, 1997*). 16
- 2.4 Bottom topographies used in the simplified model experiments. **(a)**: Rough (realistic) topography grid. **(b)**: Smooth (idealized) topography grid. Model grid details are shown on the right panel, and are identical for both grids, except for the hydrostatic consistency ratios $\Delta h/h$ and $\Delta z/z$ 18

- 2.5 Hydrographic observations in the ESB shelf. **(a)**: Sea Surface Temperature (SST) summer climatology. **(b)**: Scattered T - S diagram for two contrasting hydrographic snapshots: Cyan (magenta) dots correspond to a scenario with (without) South Atlantic Central Water (SACW) on the shelf. **(c)**: Near-bottom temperature map derived from all Conductivity, Temperature, Depth (CTD) casts of the five synoptic cruises. The black dots mark the locations of all CTD casts. The blue dots mark the casts shallower than 100 m where the near-bottom temperature was lower than 21°C (a qualitative evidence of water with high SACW content). **(d)**: Cross-shelf temperature section from the SEP04 survey (September/2004) along a transect at the narrowest part of the shelf. The black triangles along the top of the figure mark the along-transect positions of the CTD casts. The green dots on the map insert mark the position of the CTD casts within the ESB. The blue dashed line marks the approximate depth of the 21°C isotherm in a hypothetical scenario without the Brazil Current (BC). 26
- 2.6 Instantaneous maps of the thickness of the layer occupied by intruded water on the shelf. In red areas, the entire water column is occupied by water that was located offshore of the 70 m isobath (approximately the shelfbreak depth) in the initial conditions. In blue areas, no water originally offshore of the shelfbreak is present. **(a,c,e)**: Smooth topography experiments. **(b,d,f)**: Rough topography experiments. **(a,b)**: Wind-only experiments. **(c,d)**: Wind + Brazil Current experiments. **(e,f)**: Brazil Current-only experiments. In the wind-forced experiments **(a,b,c,d)** the instantaneous fields are shown for model day 8.2, near the end of the spinup of the shelf circulation. In the BC-only experiments **(e,f)**, the instantaneous fields are shown for the last model day (29.6), because the features in the dye fields take longer to develop. The thick gray lines represent the 70 m and 1000 m isobaths. 29
- 2.7 Instantaneous temperature (color shading) and velocity (vectors) at the surface and near the bottom. **(a,b)**: EXP-smoo-1 simplified experiment (wind-only). **(c,d)**: EXP-smoo-3 simplified experiment (wind+BC). **(e,f)**: Realistic experiment. **(a,c,e)**: Temperature and velocity at the surface. **(b,d,f)**: Temperature and velocity near the bottom. The red arrows in the right column panels indicate preferential pathways of onshore flow. The gray lines mark the 70 m and 1000 m isobaths. For clarity, every tenth (second) vector is drawn in the upper and middle rows (bottom row). 32
- 2.8 Run-averaged potential temperature (color shading) and cross-isobath velocity in cm s^{-1} (black contours) distribution along the 70 m isobath for the smooth topography scenarios. Solid (dashed) contours represent onshore (offshore) velocity. The heavy black line is the zero contour. **(a)**: EXP-smoo-1 (wind-only). **(b)**: EXP-smoo-3 (wind+BC). **(c)**: EXP-smoo-2 (BC-only). The red arrows indicate preferential pathways of onshore flow of cold SACW. The markers labelled 1-5 along the x -axis of the top panel indicate along-isobath locations, which correspond to the dots on the map insert. 33
- 2.9 Run-averaged potential temperature along three cross-shelf lines for the smooth topography experiments. **(a,b,c)**: EXP-smoo-1 (wind-only). **(d,e,f)**: EXP-smoo-3 (wind+BC). **(g,h,i)**: EXP-smoo-2 (BC-only). The left, middle and right columns each correspond to a different cross-shelf location, marked as a red line on the map inserts on the bottom panel of each column. 34

- 2.10 Run-averaged along-isobath pressure gradient force (PGF_{y^*}) along the 70 m isobath for the smooth topography scenarios. **(a)**: EXP-smoo-1 (wind-only). **(b)**: EXP-smoo-2 (BC-only). The heavy black line is the zero contour. The green arrows indicate preferential pathways of onshore flow, as in Figure 2.8. The markers labelled 1–5 along the x-axis of the top panel indicate along-isobath locations, which correspond to the dots on the map insert. 36
- 2.11 Run-averaged along-isobath residue between the along-isobath ageostrophic pressure gradient force ($AGEO_{y^*}$) and the net momentum advection term (NL_{y^*}). **(a)**: EXP-smoo-1 (wind-only). **(b)**: EXP-smoo-2 (BC-only). The heavy black line is the zero contour. The smallest residues are found away from the Ekman layers, within the nearly frictionless interior (areas indicated by the horizontal dashed lines). The markers labelled 1–5 along the x-axis of the top panel indicate along-isobath locations, which correspond to the dots on the map insert. 37
- 2.12 Run-averaged along-isobath residue between the along-isobath ageostrophic pressure gradient force ($AGEO_{y^*}$) and the vertical viscosity term ($VVIS_{y^*}$). **(a)**: EXP-smoo-1 (wind-only). **(b)**: EXP-smoo-2 (BC-only). The heavy black line is the zero contour. The smallest residues are found near the bottom, within the bottom Ekman layer (areas indicated by the horizontal dashed lines). The markers labelled 1–5 along the x-axis of the top panel indicate along-isobath locations, which correspond to the dots on the map insert. 38
- 2.13 Run-averaged and depth-averaged momentum balance terms in the along-isobath direction along the 70 m isobath. **(a)**: EXP-smoo-1 (wind-only). **(b)**: EXP-smoo-2 (BC-only). The blue shading marks areas of onshore flow ($U < 0$), which are indicated by the blue arrows on the map insert. The vertical lines labelled 1–5 indicate along-isobath locations, which correspond to the numbered dots on the map insert. 40
- 2.14 Time-averaged (2004–2009) and depth-averaged distributions of along-isobath pressure gradient force per unit mass ($-P_{y^*}$), Coriolis acceleration ($-fU$) and cross-isobath velocity (U) along the 70 m isobath for the realistic experiment. The blue shading marks areas of onshore flow ($U < 0$), which are indicated by the blue arrows in the map insert. The vertical lines labelled 1–5 indicate along-isobath locations, which correspond to the numbered dots on the map insert. 41
- 2.15 Horizontal distribution of run-averaged and depth-averaged along-isobath pressure gradient force per unit mass ($-P_{y^*}$, **a,c**) and Coriolis acceleration ($-fU$, **b,d**) for the smooth topography scenarios. **(a,b)**: EXP-smoo-1 (wind-only). **(c,d)**: EXP-smoo-2 (BC-only). The thick gray lines represent the 70 m and 1000 m isobaths. The color scale is the same for all panels and the heavy black line is the zero contour. The blue arrows on the right column indicate preferential pathways of onshore flow. 43

- 2.16 Model histories showing the effect of pycnocline uplifting by the BC. **(a)**: Comparison of the model minimum shelf SST histories (on the TB area) for EXP-smoo-1 (wind-only), EXP-smoo-2 (BC-only) and EXP-smoo-3 (wind+BC) experiments. The black dashed line indicates the observed climatological minimum SST (see Figure 2.5a). **(b)**: Comparison of the model shelf-averaged intruded dye volume histories (on the TB area) for the same experiments. The dashed lines are linear least-squares fits, and their slopes represent the mean onshore transport of slope water onto the shelf under each forcing scenario. τ indicates the mean flushing time of the shelf control volume, based on the slope of the linear fits. The negligible signal of the unforced scenario (solid black line) is a model sensitivity test, whose flow field is exclusively due to numerical horizontal pressure gradient errors. 45
- 2.17 Distributions of model velocity (run-averaged and depth-averaged in the upper 100 m) and centrifugal acceleration normalized by the Coriolis acceleration, $Ro_{\text{curv}} = V/(fR)$. **(a)**: Streamlines for simplified experiment EXP-smoo-2 (BC-only). The red line is the 100 m isobath, used to perform the Ro_{curv} calculations. **(b)**: Associated along-isobath velocity (blue) and curvature Rossby number Ro_{curv} as functions of latitude. The red arrows indicate areas of large curvature effects, which are found mostly where the along-isobath flow encounters sharp changes in isobath orientation. 47
- 2.18 Distributions of model velocity and relative vorticity normalized by the local inertial frequency, $Ro = |\zeta/f|$, demonstrating the proneness of shelf edge locations to the effect of shelf encroaching of the BC. **(a,b,c,d)**: Examples of observation-derived cross-transect velocity **(a,c)** and Ro **(b,d)** along two transects occupied in the OCT12 survey. The red lines on the map inserts indicate the location of the transects. **(e)**: 2004–2009 average of depth-averaged (within the upper 300 m) velocity (white streamlines) and Ro (color shading) from the realistic Hybrid Coordinate Ocean Model (HYCOM) simulation. The gray lines are the 30 m and 200 m isobaths. The arrows indicate areas of large relative vorticity, located mostly around the shelf edge, following the inshore lobe of the BC jet. 48
- 2.19 Schematic representation of a single-layer reduced gravity model for the BC. **(a)**: Geometry of the model, showing the cross-shelf (x), along-shelf (y) and vertical (z) coordinate axes, the variable thickness of the upper layer (h) and the densities of the upper (ρ_1) and lower (ρ_2) layers. **(b)**: Schematic representation of an equatorward along-shelf pressure gradient force (PGF_y) linked to an along-shelf gradient in the upper layer thickness induced by the planetary β -effect. . . 51
- 2.20 Climatological thermocline depth estimated from the World Ocean Atlas 2013 (WOA13) dataset. **(a)**: Depth of the 1025.7 kg m^{-3} isopycnal (black contours), chosen as representative of the main thermocline. The red arrows indicate the hypothetical south and north ends of the reduced gravity model. The magenta contours are the 100 m and 200 m isobaths. **(b)**: Horizontal map of number of observations at the depth of the 1025.7 kg m^{-3} isopycnal within each 0.25° square. Black means no data. The green contours are the 100 m and 200 m isobaths. . . 52

- 2.21 Schematic representation of the proposed South Atlantic Central Water (SACW) intrusion pathways and physical mechanisms in the Espírito Santo Basin (ESB). The solid black arrow indicates the direction of prevailing wind and shelf mean flow. The wiggly arrow indicates the direction of propagation of long Coastal Trapped Waves (Coastal Trapped Waves (CTWs)). The thick red line indicates the BC flow along the shelf edge and areas of local inertial overshooting. The blue arrows indicate preferential pathways for SACW intrusions. The dashed blue arrow indicates the possible pathway along the southern flank or the Abrolhos Bank (AB). The long (short) dashed black arrows over the shelf indicate areas of stronger (weaker) onshore flow. The green arrow indicates the direction of the total time–mean along–isobath pressure gradient force (PGF_{y^*}) on the shelf. . . . 54
- 3.1 Numerical time–averaged (30 days) depth–averaged along–isobath Pressure Gradient Force (PGF) at the shelf edge (70 m isobath) as a function of along–isobath distance. Each line represents a numerical solution for a different Brazil Current (BC) core velocity. The gray dashed line is a least–squares sinusoidal fit representing the idealized forcing prescribed at the shelf edge of the Arrested Topographic Wave (ATW) model. The vertical lines labelled 1–4 indicate along–isobath locations, which correspond to the numbered dots on the map insert. . . . 62
- 3.2 Solution to the Arrested Topographic Wave problem (Equation 3.16). (a): Pressure $p(x, y)$. (b): Streamlines. The red bar in the lower right corner indicates the cross–shore length scale of deep–ocean influence $\sqrt{-2r/(lfs)} = 10$ km predicted by the ATW model. (c): Cross–shelf velocity $u(x, y)$. (d): Along–shelf velocity $v(x, y)$. The red arrows indicate areas of onshore transport of water supplied at the shelf edge. 63
- 3.3 Time–averaged (30 days) flow fields from the numerical solution with a 60 cm s^{-1} BC. (a): Depth–averaged velocity streamlines. The blue arrows indicate closed–cell circulation features on the shelf. (b): Depth–averaged cross–isobath velocity U . Blue means onshore flow, red means offshore flow. Note the slant of the isotachs in the direction of long coastal trapped wave propagation (*i.e.*, equatorward). The green lines indicate the cross–shelf profiles used to estimate the numerical cross–shelf e –folding scales. 65
- 3.4 Examples of cross–shelf profiles of depth–averaged, cross–isobath velocity from the time–averaged (30 days) numerical solutions (blue lines) and associated exponential fits (dashed red lines). The numerical e –folding scales estimated with a nonlinear least–squares technique are shown. The range of e –folding scales $q = \sqrt{l/(2k)}$ predicted by the analytical model is $7.8 \times 10^{-5} \text{ m}^{-1} - 1.2 \times 10^{-4} \text{ m}^{-1}$, considering a canonical range for the linear bottom friction parameter $r = 2 - 5 \times 10^{-4} \text{ m s}^{-1}$. The map inserts show the location of each cross–shelf profile (green lines) and the spatial distribution of u (color shading). Blue means onshore flow, red means offshore flow. (a): 70 cm s^{-1} BC, south line. (b): 35 cm s^{-1} BC, north line. 66

- 3.5 Shelf-averaged cross-shelf e -folding scales for cross-shelf velocity (black dots) estimated from the numerical solutions as a function of forcing amplitude (Brazil Current core velocity). The error bars indicate one standard deviation above and below each mean. The blue shading marks the analytical predicted range of linear onshore penetration scales $q = \sqrt{l/(2k)} = \sqrt{-lfs/(2r)}$, considering a canonical range for the linear bottom friction parameter $r = 2\text{--}5 \times 10^{-4} \text{ m s}^{-1}$. The red dots mark the analytical curve of quadratic onshore penetration scales $q_{\text{quadratic}} = \sqrt{-lfs/(2C_D)} \times \sqrt{1/U_{\text{bot}}}$, where $C_D = 3.0 \times 10^{-3}$ is the quadratic bottom friction parameter used in the numerical solutions and U_{bot} is the magnitude of the near-bottom velocity (assumed to be equal to the model BC core velocity for simplicity). $q_{\text{quadratic}}$ represents increments relative to the first numerical e -folding scale ($U_{\text{bot}} = 20 \text{ cm s}^{-1}$) rather than absolute values. Representative values for the TB are used: Bottom slope $s = 2.68 \times 10^{-3}$, inertial frequency $f = -5.10 \times 10^{-5} \text{ s}^{-1}$, and an along-shelf wavenumber $l = 4.42 \times 10^{-5} \text{ m}^{-1}$ for the forcing at the shelf edge. 67

List of Tables

2.1	Outline of the process-oriented numerical experiments performed with Regional Ocean Modeling System (ROMS).	21
2.2	Shelf-averaged stratification frequency squared (N^2), slope Burger number ($S \equiv \alpha N/f$) and its square for the Tubarão Bight (TB) area (19.5°S–22°S).	25
3.1	Parameters used in the ATW model.	61

List of Acronyms

AB	Abrolhos Bank
ACR	Abrolhos–Campos Region
ADCP	Acoustic Doppler Current Profiler
AE	Abrolhos Eddy
ATW	Arrested Topographic Wave
BC	Brazil Current
CODAS	Common Ocean Data Access System
CTD	Conductivity, Temperature, Depth
CTW	Coastal Trapped Wave
EAC	East Australian Current
ESB	Espírito Santo Basin
FORMS	Feature–Oriented Regional Modeling System
HPGE	Horizontal Pressure Gradient Error
HYCOM	Hybrid Coordinate Ocean Model
NOAA	National Oceanic and Atmospheric Administration
RCE	Royal–Charlotte Eddy
ROMS	Regional Ocean Modeling System
SACW	South Atlantic Central Water
SASG	South Atlantic Subtropical Gyre
SEC	South Equatorial Current
SST	Sea Surface Temperature
TB	Tubarão Bight
TW	Tropical Water
VE	Vitória Eddy
VTR	Vitória–Trindade Ridge
WOA13	World Ocean Atlas 2013

Abstract

The intrusion pathways and physical mechanisms associated with intrusions of cold, nutrient-rich South Atlantic Central Water (SACW) onto the continental shelf of the Espírito Santo Basin (ESB), off southeast Brazil (18°S–22°S), are investigated. The approach consists of analyses of a set of simplified, process-oriented, primitive-equation numerical models supported by the analyses of an independent, more realistic numerical model and available observations. The cross-isobath circulation is found to be strongly dominated by wind-driving, consistent with previous findings. In the model experiments, SACW enters the ESB shelf through two preferential pathways along the Tubarão Bight area (TB, 19.5°S–22°S). These pathways are found to be locations where an equatorward along-isobath pressure gradient force (PGF_{y^*}) of $\approx 2 \times 10^{-6} \text{ m s}^{-2}$ develops in response to steady wind forcing. This equatorward PGF_{y^*} is essentially in geostrophic balance, and therefore induces onshore flow across the shelf edge and most of the shelf proper. The Brazil Current (BC) imparts an additional equatorward PGF_{y^*} on the shelf. The momentum budget reveals that the ageostrophic residue of the PGF_{y^*} is compensated mostly by momentum advection and bottom friction. Buoyancy arrest might be important under more intense SACW intrusion events, as suggested by the maximum observed values of the slope Burger number (0.32–0.92). Among the deep-ocean forcing mechanisms considered, the intrinsic pycnocline uplifting effect of the BC seems to be responsible for $\approx 1.4^\circ\text{C}$ colder upwelled water under steady, upwelling-favorable wind forcing, relative to a flat stratification scenario. The BC also seems to induce local intrusions by inertially overshooting the shelf edge, consistent with Rossby numbers of ≈ 0.3 – 0.5 , as estimated for the area along the TB shelf edge. Finally, the planetary β -effect is also related to a background equatorward PGF_{y^*} .

In addition, the steady response of the continental shelf to a periodic (in the along-shelf direction) pressure forcing at the shelf edge is compared with the BC-forced primitive-equation numerical solutions. A simple Arrested Topographic Wave (ATW) analytical model is found to be successful in representing the general features of the numerical solutions. The cross-shelf e -folding scales of the cross-shelf velocity estimated from the numerical solutions agree in order of magnitude with the cross-shelf penetration scale $q^{-1} = \sqrt{-2r/(lfs)} = 10 \text{ km}$ predicted by the ATW, where r is a linear bottom resistance parameter, l is the along-shelf wavenumber of the forcing at the shelf edge, f is the Coriolis parameter and s is the bottom slope. Furthermore, the use of quadratic bottom stress accounts for some of the relative increase in the numerical onshore penetration scales, which are predicted to be $q_{\text{quadratic}}^{-1} = \sqrt{-2C_D/(lfs)} \times \sqrt{U_{\text{bot}}}$, where C_D is a quadratic bottom friction parameter and U_{bot} is the near-bottom velocity magnitude. The kind of steady response to periodic deep-ocean forcing examined here may provide insight into other continental shelves under the influence of western boundary currents.

Keywords: *Ocean–shelf exchange, coastal dynamics, deep–ocean forcing, cross–shelf transport, Arrested Topographic Wave, Brazil Current, South Atlantic Central Water.*

Resumo

Os caminhos e os mecanismos físicos associados ao fenômeno de intrusão da Água Central do Atlântico Sul (ACAS) na plataforma continental da Bacia do Espírito Santo (BES) ao largo da costa sudeste (18°S–22°S) são investigados nesta dissertação. A abordagem consiste da análise de experimentos numéricos de equações primitivas simplificados, combinados com a análise de um modelo numérico mais completo, e com análise de observações disponíveis. Conclui-se que a circulação na direção perpendicular às isóbatas é fortemente dominada pelo vento, de acordo com resultados pretéritos. Nos experimentos numéricos, a ACAS ingressa na plataforma da BES através de dois caminhos preferenciais de intrusão no Embaiamento de Tubarão (ET, 19.5°S–22°S). Estes caminhos de intrusão coincidem com áreas em que uma Força do Gradiente de Pressão na direção paralela às isóbatas (PGF_{y*}), com magnitude de $\approx 2 \times 10^{-6} \text{ m s}^{-2}$, se forma em resposta ao vento. A PGF_{y*} se encontra essencialmente em balanço geostrófico, e impulsiona um escoamento na direção da costa. A Corrente do Brasil (CB) induz uma PGF_{y*} adicional favorável à intrusão. O balanço de *momentum* revela que o resíduo ageostrófico da PGF_{y*} é balanceado principalmente pela advecção de *momentum* e pelo atrito de fundo. O mecanismo de desligamento da camada de Ekman de fundo por empuxo¹ pode ser importante em eventos mais intensos de intrusão de ACAS, em razão das estimativas do número de Burger de inclinação² observado (0.32–0.92). O efeito de soerguimento da termoclina ligado à CB aparenta diminuir $\approx 1.4^\circ\text{C}$ a temperatura da água que aflora em eventos de ressurgência costeira. A CB também parece produzir intrusões locais na borda da plataforma por efeitos inerciais, de acordo com as estimativas de ≈ 0.3 – 0.5 para o número de Rossby ao longo da borda da plataforma. Por fim, o efeito β planetário também é associado a uma PGF_{y*} básica na direção do equador.

Adicionalmente, a resposta estacionária da plataforma continental a um campo de pressão periódico ao longo da borda da plataforma é comparada com as soluções numéricas. Um simples modelo analítico do tipo Onda Topográfica Aprisionada³ (OTA) representa as características gerais das soluções numéricas. As escalas de decaimento neperiano (e) na direção perpendicular à plataforma estimadas a partir das soluções numéricas são comparáveis à escala de penetração $q^{-1} = \sqrt{-2r/(lfs)} = 10 \text{ km}$ prevista pela OTA, onde r é um coeficiente linear de atrito de fundo, l é o número de onda da forçante, f é o parâmetro de Coriolis e s é a inclinação do fundo. O uso de uma parametrização quadrática para o atrito de fundo prevê parte da diminuição da e . A escala de penetração quadrática é $q_{\text{quadratic}}^{-1} = \sqrt{-2C_D/(lfs)} \times \sqrt{U_{\text{bot}}}$, onde C_D é um coeficiente quadrático de atrito de fundo e U_{bot} é a magnitude da velocidade próxima ao fundo. Este tipo de resposta estacionária da plataforma a uma forçante periódica ligada ao oceano profundo pode ajudar a elucidar processos físicos em outras plataformas continentais que se encontram sob a influência de correntes de limite oeste.

Descritores: Troca de propriedades entre o oceano profundo e a plataforma continental, dinâmica costeira, efeitos do oceano profundo sobre a plataforma continental, Circulação na direção perpendicular à plataforma, Onda Topográfica Aprisionada, Corrente do Brasil, Água Central do Atlântico Sul.

¹Tradução livre de *buoyancy arrest*.

²Tradução livre de *slope Burger number*.

³Tradução livre de *Arrested Topographic Wave*.

Chapter 1

Introduction to the thesis

1.1 On the thesis structure

The core of this thesis is composed of two chapters written in the form of self-contained manuscript drafts (Chapters 2 and 3), in which the pathways and the associated physical mechanisms of South Atlantic Central Water (SACW) intrusions in the Espírito Santo Basin (ESB, 18°S–22°S) are investigated. In the present Chapter, a brief regional overview of the western boundary of the South Atlantic Subtropical gyre is given in Section 1.2, followed by a statement of the dynamical constraints involved in cross-isobath flow in Section 1.3. The thesis hypotheses and objectives are posed in Section 1.4. Chapter 4 Summarizes the main findings of Chapters 2 and 3 and presents some of the open questions that could be addressed by future work.

1.2 Regional overview

The region of interest of this thesis is located in the western South Atlantic, in the western boundary of the anticyclonic large-scale feature known as the South Atlantic Subtropical Gyre (SASG, Figure 1.1). The SASG extends from the surface down to the base of the pycnocline, in the upper ≈ 1000 m of the water column. Its eastern and western boundary currents are the Benguela Current and the Brazil Current (BC), respectively. The quasi-zonal flows of the South Atlantic Current

and the South Equatorial Current (SEC) connect the eastern and western boundaries of the SASG (*e.g.*, [Talley et al., 2011](#)). The SASG encompasses the latitude band between $\approx 10^\circ\text{S}$ and $\approx 40^\circ\text{S}$, decreasing in meridional extent with increasing depth due to the southward shift of the SEC transport ([Schmid, 2014](#)).

As the western boundary current of the SASG, the BC flows poleward in the form of a Sverdrup return transport, analogous to *e.g.*, the Gulf Stream in the North Atlantic or the East Australian Current (EAC) in the South Pacific. The BC forms where the southern branch of the SEC impinges on the continental margin of South America. The bifurcation of the SEC has, however, a complicated depth dependence. At surface levels, in the domain of the Tropical Water (TW), the SEC bifurcates in the latitude range 13°S – 17°S . At pycnocline levels, in the domain of the South Atlantic Central Water (SACW), the bifurcation is located climatologically at $\approx 18.6^\circ\text{S}$ ([Figure 1.2](#), [Stramma & England, 1999](#); [Rodrigues et al., 2007](#); [Schmid, 2014](#)). As a result of this southward shift of the bifurcation with depth, the BC thickens downstream, increasing its vertical extension from 350 m at 22.7°S to 850 m at 27.9°S ([Rocha et al., 2014](#)).

The Espírito Santo Basin (ESB) is located in the northernmost part of the Southeast Sector (20°S – 28°S) of the Brazil Current System, close to the pycnoclinic bifurcation latitude of the SEC. In this region, the BC has a conspicuous mesoscale activity, with semi-permanent eddies steered by the complex regional topography ([Soutelino et al., 2011, 2013](#); [Arruda et al., 2013](#)). The ESB continental shelf is located in the coastal domain known as the Abrolhos–Campos Region (ACR, [Castro & Miranda, 1998](#)). In the archetypal coastal regime classification of [Loder et al. \(1998\)](#), the ESB shelf is as narrow, wind-driven shelf, with a Western Boundary Current at its edge. This type of shelf is usually expected to be oligotrophic, in contrast to the eutrophic eastern boundary coastal upwelling systems ([Walsh, 1988](#)). However, local areas of high biological productivity are known to exist (*e.g.*, [Gaeta et al., 1999](#)), and seasonal coastal upwelling of nutrient-rich SACW has long been observed in this region, mostly from satellite data (*e.g.*, [Schmid et al., 1995](#); [Rodrigues & Lorenzetti, 2001](#); [Castelão & Barth, 2006](#); [Castelão, 2012](#); [Mazzini](#)

& Barth, 2013).

Historically, the neighboring coastal upwelling system of Cape Frio (23°S) has received far more scientific attention (*e.g.*, *Allard, 1955; Emilsson, 1961; Ikeda et al., 1976; Carbonel, 2003; Franchito et al., 2008*). Although there has been some recent development on the understanding of the coastal kinematics and dynamics of the ESB on the basis of observations and analytical models (*Mazzini & Barth, 2013*) and primitive–equation numerical models (*Aguiar et al., 2014*), numerous basic questions remain. For instance, (i) *Through which pathways does SACW enter the shelf in the ESB?* and (ii) *What are the driving physical mechanisms of these intrusions, and more specifically what are the effects of bottom topography, wind–driving and the BC?* This thesis addresses these questions. An answer to (i) can contribute to the basic description of the regional hydrography, whereas an answer to (ii) is key in the understanding of the coastal dynamics and of the coupling of the coastal ocean and the deep–ocean.

1.3 The Taylor–Proudman constraint

The dynamical basis for understanding the mechanisms involved in exchange between the deep–ocean and the continental shelf are embodied in the Taylor–Proudman constraint. In this section, we follow the reasoning in *Brink (1998)* to arrive at this well–known result.

Assuming that the flow is steady, linear and inviscid, and that the meridional scale of the flow is not too large, the equations of motion under the hydrostatic and Boussinesq approximations are

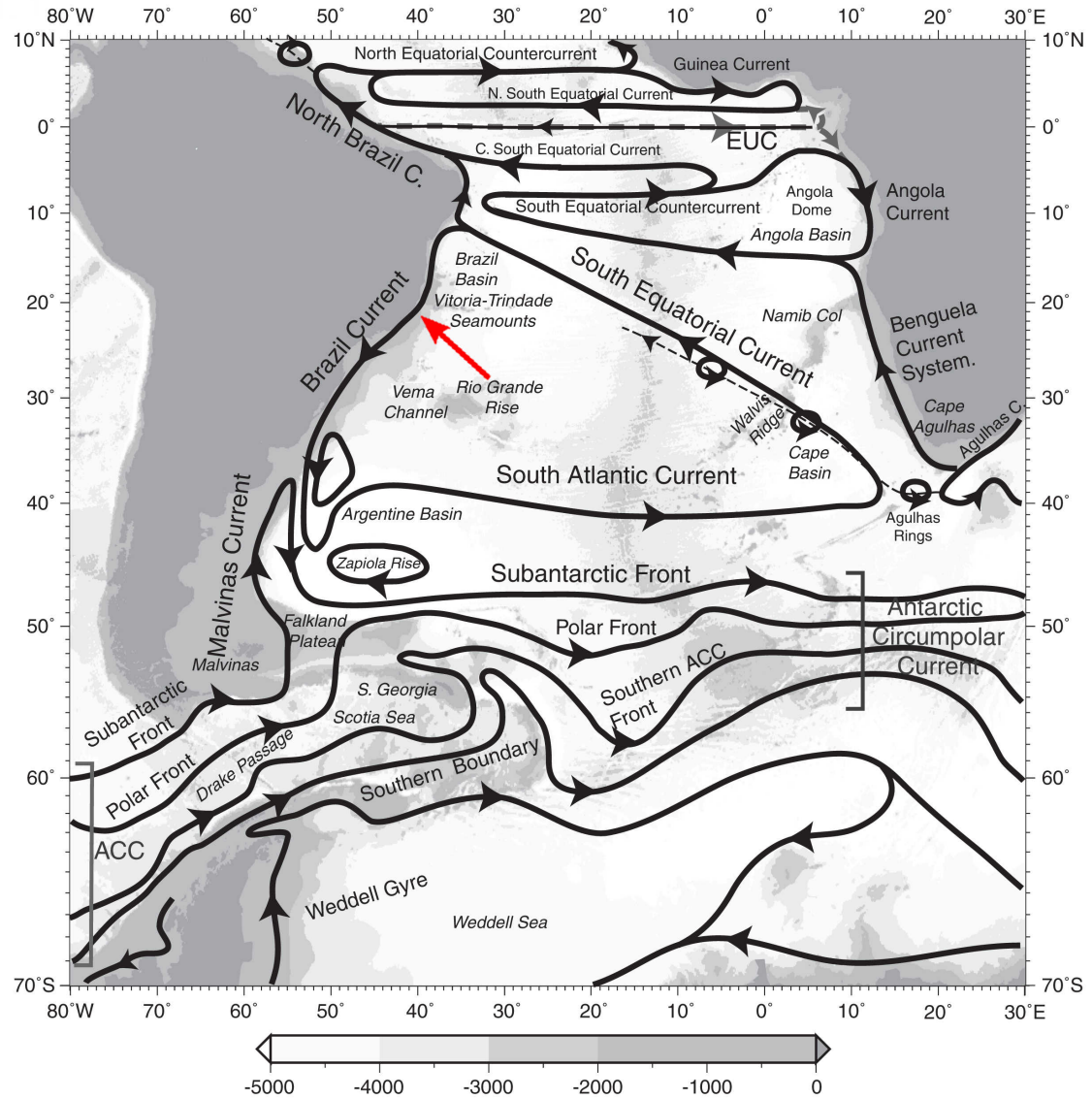


Figure 1.1: Schematic representation of the upper ocean circulation in the South Atlantic. The red arrow indicates the location of the Espírito Santo Basin (ESB) in the western boundary of the South Atlantic Subtropical Gyre (SASG). Adapted from *Talley et al. (2011)*. Original version available at <http://booksite.elsevier.com/DPO/>.

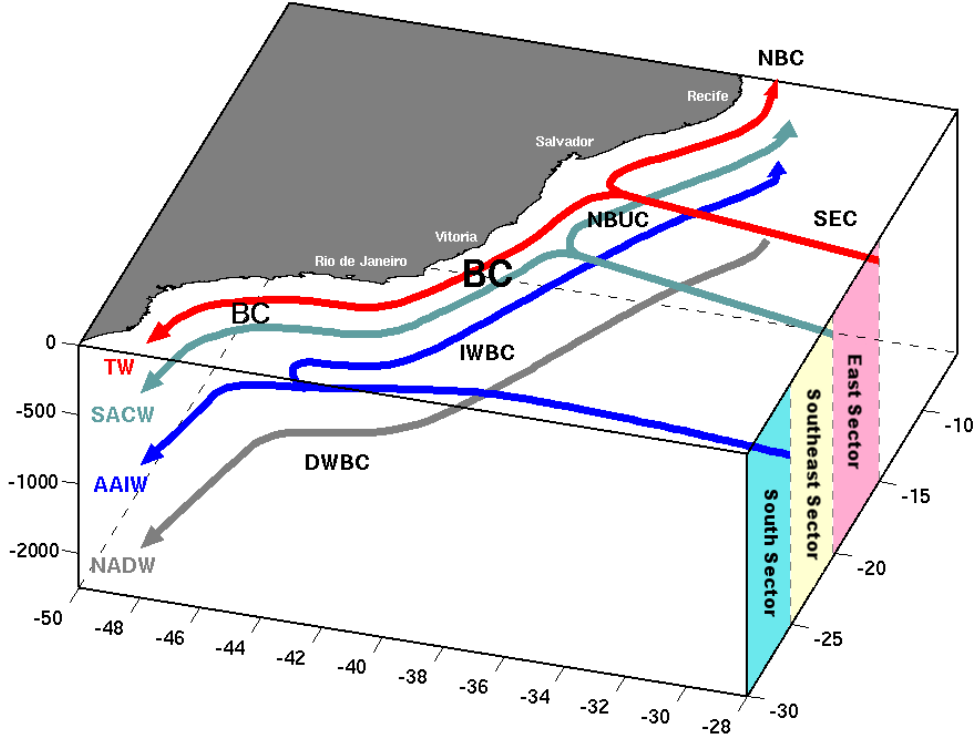


Figure 1.2: Schematic representation of the vertical structure of western boundary currents and water masses in the South Atlantic Subtropical Gyre (SASG). SEC, BC, NBUC, NBC, IWBC and DWBC stand for South Equatorial Current, Brazil Current, North Brazil Undercurrent, North Brazil Current, Intermediate Western Boundary Current and Deep Western Boundary Current, respectively. TW, SACW, AAIW and NADW stand for Tropical Water, South Atlantic Central Water, Antarctic Intermediate Water and North Atlantic Deep Water, respectively. The Espírito Santo Basin (ESB) is located in the northern end of the Southeast Sector (20°S – 28°S) of the Brazil Current System, approximately at the bifurcation latitude of the SEC at pycnocline levels. Courtesy: Gilberto Watanabe (IO/USP). Modified from the original version published by *Soutelino et al.* (2013).

$$fv = \frac{1}{\rho_0} p_x \quad (1.1a)$$

$$fu = -\frac{1}{\rho_0} p_y \quad (1.1b)$$

$$0 = -p_z - g\rho \quad (1.1c)$$

$$u_x + v_y + w_z = 0 \quad (1.1d)$$

$$u\rho_x + v\rho_y + w\rho_z = 0, \quad (1.1e)$$

where (x, y, z) are the cross-shelf, along-shelf and vertical directions, (u, v, w) are the velocity components in the (x, y, z) directions, f is the Coriolis parameter (assumed constant), $\rho_0(z)$ is the reference density, $\rho(x, y, z)$ is the total density, p is

pressure and g is the acceleration due to gravity. Subscripts with respect to the independent variables x , y and z indicate partial differentiation. Plugging Equations 1.1a and 1.1b into 1.1d yields

$$w_z = 0 \quad (1.2)$$

recognizing that flow must not pass through the bottom and assuming that the displacement of the free-surface is negligible (*i.e.*, the rigid-lid approximation) translates into

$$w = 0 \quad \text{at} \quad z = 0 \quad (1.3a)$$

$$w = -\mathbf{u} \cdot \nabla h \quad \text{at} \quad z = -h, \quad (1.3b)$$

where $\nabla \equiv \hat{\mathbf{x}}\partial_x + \hat{\mathbf{y}}\partial_y$ is the horizontal gradient operator and $\mathbf{u} \equiv \hat{\mathbf{x}}u + \hat{\mathbf{y}}v$ is the horizontal velocity vector. Combining the surface boundary condition (Equation 1.3a) with Equation 1.2 implies that $w = 0$ everywhere, such that Equation 1.3b becomes

$$\mathbf{u} \cdot \nabla h = 0 \quad \text{at} \quad z = -h. \quad (1.4)$$

Equation 1.4 says that there must be no flow against the topography at the bottom, or, equivalently, that bottom flow is constrained to always following isobaths. Differentiating Equations 1.1a and 1.1b with respect to z gives

$$(\rho_0 v)_z = \frac{(p_z)_x}{f} \quad (1.5a)$$

$$(\rho_0 u)_z = -\frac{(p_z)_y}{f} \quad (1.5b)$$

Plugging Equation 1.1c into Equations 1.5a and 1.5b to eliminate p yields

$$(\rho_0 v)_z = -\frac{g}{f} \rho_x \quad (1.6a)$$

$$(\rho_0 u)_z = \frac{g}{f} \rho_y \quad (1.6b)$$

Substituting Equations 1.6a and 1.6b in to Equation 1.1e gives the result

$$uv_z - vu_z = 0, \quad (1.7)$$

or, equivalently,

$$\hat{z} \cdot (\mathbf{u} \times \mathbf{u}_z) = 0, \quad (1.8)$$

where \hat{z} is the unit vector in the vertical direction. Equation 1.8 demonstrates that vertical shear in steady, linear, inviscid flow on an f -plane is always parallel to the flow¹, and flow is constrained to following isobaths, as stated by Equation 1.4. Therefore, relaxing any of the four assumptions made here leads to deviations from geostrophy and in turn to cross-isobath transport. This result holds both in the homogeneous and stratified cases, meaning that the existence of stratification alone is not related to cross-isobath flow.

1.4 Thesis hypotheses and objectives

In Chapter 2, we test the hypothesis that *The Espírito Santo Basin continental shelf is wind-driven at lowest order and modulated by multiple deep-ocean forcing mechanisms linked to the Brazil Current at next order*. Specifically, the objectives of Chapter 2 are:

- To characterize the hydrography of the South Atlantic Central Water (SACW) intrusion phenomenon in the Espírito Santo Basin (ESB);

¹An exception is when $\mathbf{u} = 0$ at some level, in which case the flow can decouple, allowing geostrophic flow above the depth of no motion to cross isobaths.

- To model the effects of bottom topography, wind forcing and the Brazil Current on the SACW intrusions in the ESB;
- To develop a physical understanding of the SACW intrusions in the ESB from kinematic and dynamical standpoints;
- To examine the momentum budget of the system in the along-isobath direction and to evaluate leading-order balances and hence cross-isobath transport mechanisms;
- To rationalize the core physics contained in the observations and numerical models in terms of simpler conceptual and analytical models.

To pursue these objectives, process-oriented, simplified, primitive-equation numerical models are used in concert with a more complete numerical model, available observations and simple theoretical ideas.

In [Chapter 3](#), we further examine the response of the ESB shelf to deep-ocean forcing. Specifically, we test the hypothesis that *the time-mean response of the ESB shelf circulation to the Brazil Current forcing at the shelf edge can be rationalized in terms of a modified form of the classic Arrested Topographic Wave model (Csanady, 1978)*. The objectives of [Chapter 3](#) are:

- To derive a simple modified form of the original Arrested Topographic Wave (ATW) model that includes periodic forcing at the shelf edge and
- To compare the theoretical predictions from the modified ATW model with simplified numerical solutions for the ESB, in particular with respect to the onshore extent of the Brazil Current influence.

The analytical ATW model and a subset of the simplified numerical solutions discussed in [Chapter 2](#) are combined to fulfill these objectives.

Chapter 2

Pathways and mechanisms of offshore water intrusions on the Espírito Santo Basin (18°S–22°S, Brazil)

Abstract

The intrusion pathways and physical mechanisms associated with intrusions of cold, nutrient-rich South Atlantic Central Water (SACW) onto the continental shelf of the Espírito Santo Basin (ESB), off southeast Brazil (18°S–22°S), are investigated. The approach consists of analyses of a set of simplified, process-oriented, primitive-equation numerical models supported by the analyses of an independent, more realistic numerical model and available observations. The cross-isobath circulation is found to be strongly dominated by wind-driving, consistent with previous findings. In the model experiments, SACW enters the ESB shelf through two preferential pathways along the Tubarão Bight area (TB, 19.5°S–22°S). These pathways are found to be locations where an equatorward along-isobath pressure gradient force (PGF_{y^*}) of $\approx 2 \times 10^{-6} \text{ m s}^{-2}$ develops in response to steady wind forcing. This equatorward PGF_{y^*} is essentially in geostrophic balance, and therefore induces onshore flow across the shelf edge and most of the shelf proper. The BC imparts an additional PGF_{y^*} on the shelf, which is about half as intense as the wind-driven PGF_{y^*} and alternates sign. The momentum budget reveals that the ageostrophic residue of the PGF_{y^*} is compensated mostly by momentum advection and bottom friction. Onshore bottom Ekman transport does not seem to have important leading-order effects, possibly due to buoyancy arrest under more intense SACW intrusion events, as suggested by the maximum observed values of the slope Burger number (0.32–0.92). Among the deep-ocean forcing mechanisms considered, the intrinsic pycnocline

uplifting effect of the BC seems to be responsible for $\approx 1.4^\circ\text{C}$ colder upwelled water under steady, upwelling–favorable wind forcing, relative to a flat stratification scenario. The BC also seems to induce local intrusions by inertially overshooting the shelf edge, consistent with Rossby numbers of $\approx 0.3\text{--}0.5$, as estimated for the area along the TB shelf edge. Finally, the planetary β –effect is also related to a background equatorward PGF_{y^*} .

Keywords: *Ocean–shelf exchange, coastal dynamics, cross–shelf transport, Brazil Current, South Atlantic Central Water.*

2.1 Introduction

The Espírito Santo Basin (ESB) is located in the western boundary of the South Atlantic, within the Abrolhos–Campos Region (ACR, *Castro & Miranda, 1998*), slightly to the south of the latitude at which the southern branch of the South Equatorial Current bifurcates, originating the Brazil Current (BC). At surface levels (0–200 m), within the domain of the warm and oligotrophic Tropical Water (TW), the bifurcation site migrates seasonally in the $13\text{--}17^\circ\text{S}$ range. At 200 m, within the domain of the cold and eutrophic South Atlantic Central Water (SACW), the bifurcation takes place climatologically at 18.6°S , slightly to the north of the Vitória–Trindade Ridge (*Figure 2.1, Stramma & England, 1999; Rodrigues et al., 2007*).

At mesoscales, offshore of the shelfbreak, the ESB is dominated by a rich eddy field. According to *Soutelino et al. (2011)*, three semi-permanent anticyclones occupy the surroundings of the Abrolhos Bank (AB, *Figure 2.2*). Furthermore, to the south of the VTR there is a transient cyclonic perturbation of the BC, known as the Vitória Eddy (VE, *Schmid et al., 1995; Arruda et al., 2013*). This scenario reveals a complex oceanic circulation in the ESB, which can be expected to be a possible forcing to the SACW intrusions onto the continental shelf. As pointed out by *Soutelino et al. (2013)*, the presence of cyclones or anticyclones could lead to different patterns of ocean–shelf exchange. Hereafter, SACW will be taken to mean relatively colder and fresher water on the shelf (compared to the warmer and saltier TW).

On the continental shelf, the main forcing in the banks area is the wind, which

is southwestward year-round, producing southwestward currents (Figure 2.2). Along-shelf current variability in the middle shelf is mostly driven by the wind in the subinertial band, and cross-shelf current variability in the middle shelf is mostly tidally-induced (Castro *et al.*, 2013). In the inner shelf, the along-shelf circulation is mostly driven by the subinertial along-shelf winds (Teixeira *et al.*, 2013). Shelfbreak upwelling induced by internal tides seems to be important along the southern flank of the AB (Pereira *et al.*, 2005), possibly contributing to the observed local nutrient enrichment (Gaeta *et al.*, 1999). North of the VTR, the newly-formed BC flows offshore, and has little effect on the shelf circulation. In contrast, to the south of 19°S, this current is well-defined and follows the shelf edge closely (Castro & Miranda, 1998). For example, Miranda & Castro (1982) have observed a BC transport of ≈ 1 Sv ($\text{Sv} \equiv 10^6 \text{m}^3 \text{s}^{-1}$) inshore of the shelfbreak at 19°S.

Coastal waters between the AB and Cape São Tomé are dominated by the influence of the warm and salty TW year-round. In the AB, the TW occupies most of the volume of the continental shelf. To the south of the AB (21°S), the influence of the relatively colder and fresher SACW close to the bottom is intermittent. Such influence is most intense in summer, when a strong seasonal thermocline is established in response to the penetration of this oceanic water mass onto the continental shelf (Castro & Miranda, 1998).

The first study to consider the dynamics of the coastal circulation under steady wind forcing in the ESB was carried out by Rodrigues & Lorenzetti (2001). The authors addressed the effects of coastline geometry and bottom topography on the coastal circulation, using a set of three process-oriented experiments with a two-layer numerical model. They suggest that bottom topography is more important than coastline geometry in controlling the time-averaged coastal upwelling response in the Tubarão Bight (TB) area (19.5°S–22°S). The more simplified analytical approach employed by Mazzini & Barth (2013) further clarified the upwelling mechanisms related to wind forcing and coastal geometry, by breaking down the vertical transport into two wind-forced components (coastal Ekman transport divergence and Ekman pumping) and two topographically-forced components

(shear vorticity and curvature vorticity). Specifically, they show that the TB region to the north of Vitória ($\approx 19.5^\circ\text{S}$ – 20.5°S , see [Figure 2.1](#)) is where the Ekman transport–forced upwelling is a maximum ($\approx 0.75 \text{ m}^2 \text{ s}^{-1}$). In addition, they estimate that wind–driven (topographically–driven) upwelling in the TB area is more than 75 % (less than 25 %) of the total upwelling, with the Ekman transport divergence accounting for nearly the entire wind–driven signal (80–100 %). This also substantiates earlier results from [Castelão & Barth \(2006\)](#), confirming that the contribution of Ekman transport divergence is far more important to vertical transport in the TB than Ekman pumping.

Although deep–ocean forcing mechanisms related to the BC seem to be relevant to coastal upwelling south of the ESB ([Calado et al., 2010](#); [Palóczy et al., 2014](#)), their effects within the ESB have only recently been examined in the study by [Aguiar et al. \(2014\)](#). The authors performed diagnostic analyses of a realistic primitive–equation numerical model to quantify the upwelling contributions from Ekman transport, Ekman pumping, encroaching of the BC¹ onto the shelf and cyclonic BC meandering². They found that BC encroaching is generally more effective than cyclonic meanders in driving SACW intrusions within the TB area. [Aguiar et al. \(2014\)](#) also point out that coastal Ekman transport divergence is the most effective forcing mechanism around 21°S , consistent with the previous findings of [Castelão & Barth \(2006\)](#) and [Mazzini & Barth \(2013\)](#).

The above review shows that much remains to be learned on the SACW intrusion processes within the ESB. The aim of this study is to answer the following questions:

1. Through which preferential pathways (if any) does SACW penetrate onto the continental shelf within the ESB?
2. What are the driving physical mechanisms of the cross–isobath circulation on the continental shelf? Specifically, what are the individual and combined

¹“Encroaching” is taken to mean the inertial overshooting of the BC jet onto the shelf as it encounters a sharp change in isobath orientation.

²Cyclonic meanders produce vertical transport either by uplifting the pycnocline and propagating along the shelf edge or by drawing water from the shelf, thereby producing an additional return flow.

effects of bottom topography, wind-driving, and the Brazil Current?

The approach chosen consists of analyses of a set of process-oriented experiments with a simplified primitive-equation numerical model, supported by analyses of an independent, more realistic numerical model and available observations. We first describe the datasets in [Section 2.2](#) and the numerical models in [Section 2.3](#). Next, in [Section 2.4](#), we analyze the pathways through which SACW may enter the ESB shelf. We then address the dynamics linked to the intrusion processes in [Section 2.5](#), and attempt to isolate and rationalize some of the physical mechanisms involved in [Section 2.6](#). We conclude by summarizing the primary results and presenting conclusions in [Section 2.7](#).

2.2 Datasets

2.2.1 *In situ* quasi-synoptic hydrographic and velocity data

The *in situ* data used in this study come from five quasi-synoptic oceanographic cruises: Abrolhos 1 (September/2004), Abrolhos 2 (March/2005), PRO-ABROLHOS (September/2007), AMBES 09 (October/2012) and AMBES 10 (May/2013). Hereafter we will refer to these surveys as SEP04, MAR05, SEP07, OCT12 and MAY13, respectively. Surveys SEP04, MAR05 and SEP07 were carried out on the R/V Prof. *Wladimir Besnard*, while surveys OCT12 and MAY13 were carried out on the R/V *Seward Johnson*. The geographic distribution of the Conductivity, Temperature, Depth (CTD) stations of each survey are shown in [Figure 2.3](#). Hydrographic data from the CTD casts were processed following standard procedures (e.g., [McTaggart et al., 2010](#)). Velocity data from underway Acoustic Doppler Current Profiler (ADCP) time-averaged profiles were processed with the Common Ocean Data Access System (CODAS) software, following the procedures described in [Firing et al. \(1995\)](#).

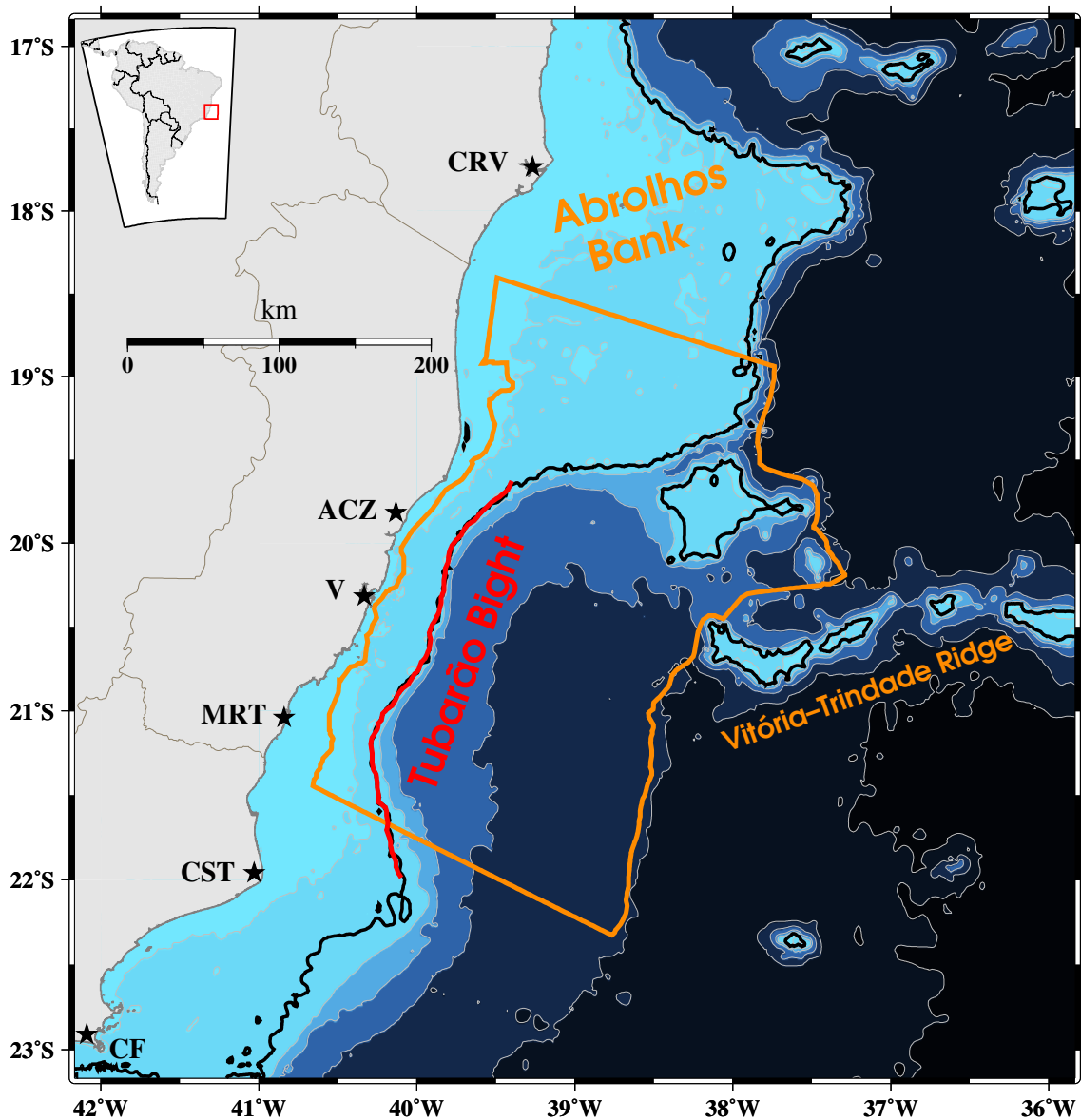


Figure 2.1: Topographic map of the Espírito Santo Basin (ESB). The upper-left map insert marks the location of the study area off the coast of South America (red rectangle). The locations marked by the black stars are Cape Frio (CF), Cape São Tomé (CST), Marataízes (MRT), Vitória (V), Aracruz (ACZ) and Caravelas (CRV). The orange polygon indicates the limits of the ESB. The red line indicates the domain of the Tubarão Bight (TB). The gray lines are the 30 m, 500 m, 1000 m, 2000 m, 3000 m and 4000 m isobaths, and the black line is the 100 m isobath, derived from the 30-arcsecond SRTM30-plus dataset (updated from *Smith & Sandwell, 1997*).

2.2.2 Climatological hydrographic data

Climatological data from the World Ocean Atlas 2013 (WOA13) were used in the elaboration of the initial conditions of the simplified numerical experiments and in the evaluation of one of the analytical models. The fields used in this study are the Temperature (*Locarnini et al., 2013*) and Salinity (*Zweng et al., 2013*) austral summer distributions, objectively-analyzed to a 0.25° grid with 102 vertical levels.

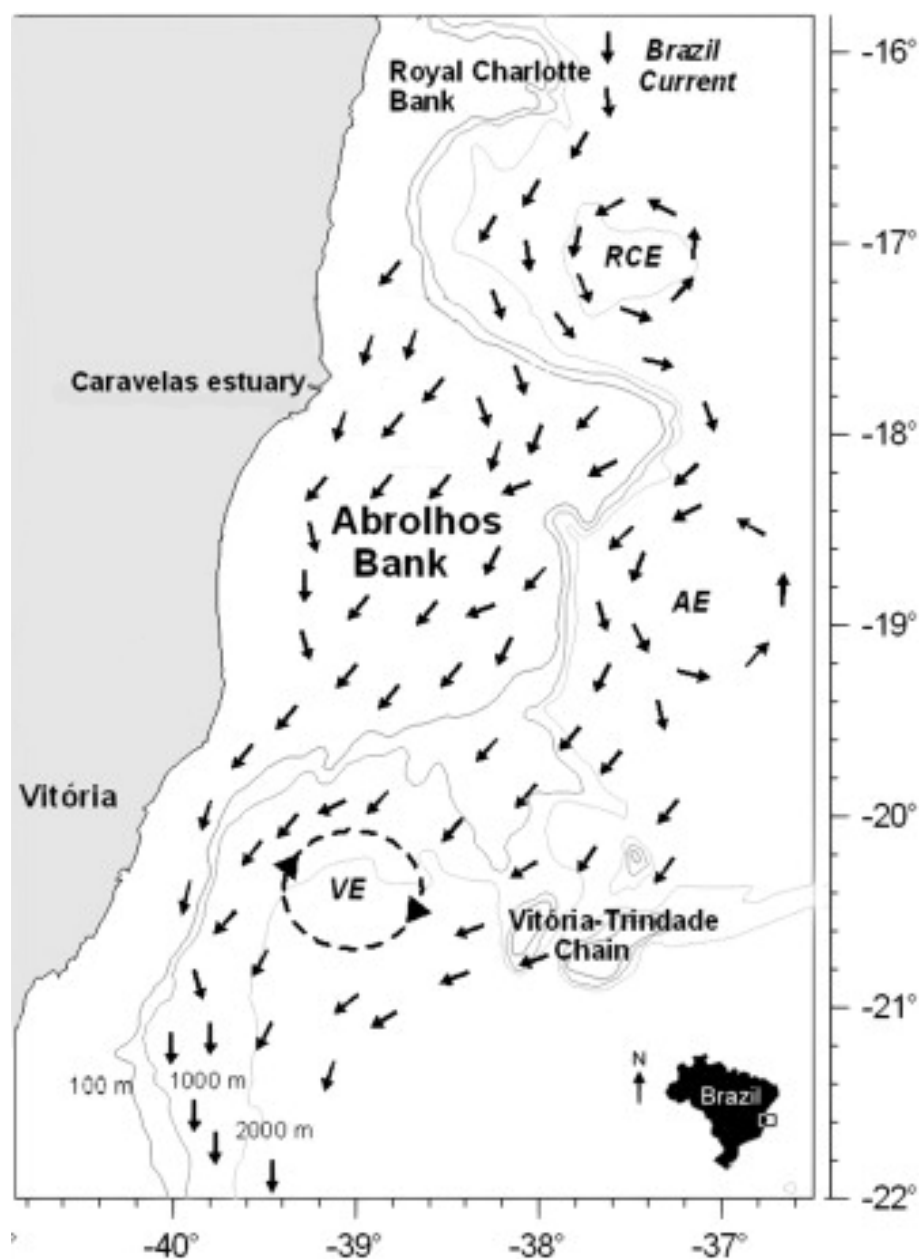


Figure 2.2: Schematic representation of the regional circulation in the Espírito Santo Basin. The acronyms RCE, AE and VE stand for Royal-Charlotte Eddy, Abrolhos Eddy and Vitória Eddy, respectively. The black arrows indicate the prevailing flow pattern, and are not to scale. Adapted from *Lopes & Castro (2013)*.

2.2.3 Satellite data

Satellite data were used to characterize the wind regime in the ESB and to map the mean Sea Surface Temperature (SST) signal of the coastal upwelling plume. Daily, 25 km-resolution wind stress data were derived from the *Multiple-Satellite Blended Sea Surface Winds* product, made available by the National Oceanic and Atmospheric Administration (NOAA, *Zhang et al., 2006*). The summer climatological (1982–2008), 4 km-resolution SST field was derived from the Pathfinder

Project (version 5.0), also made available by NOAA (*Casey et al., 2010*).

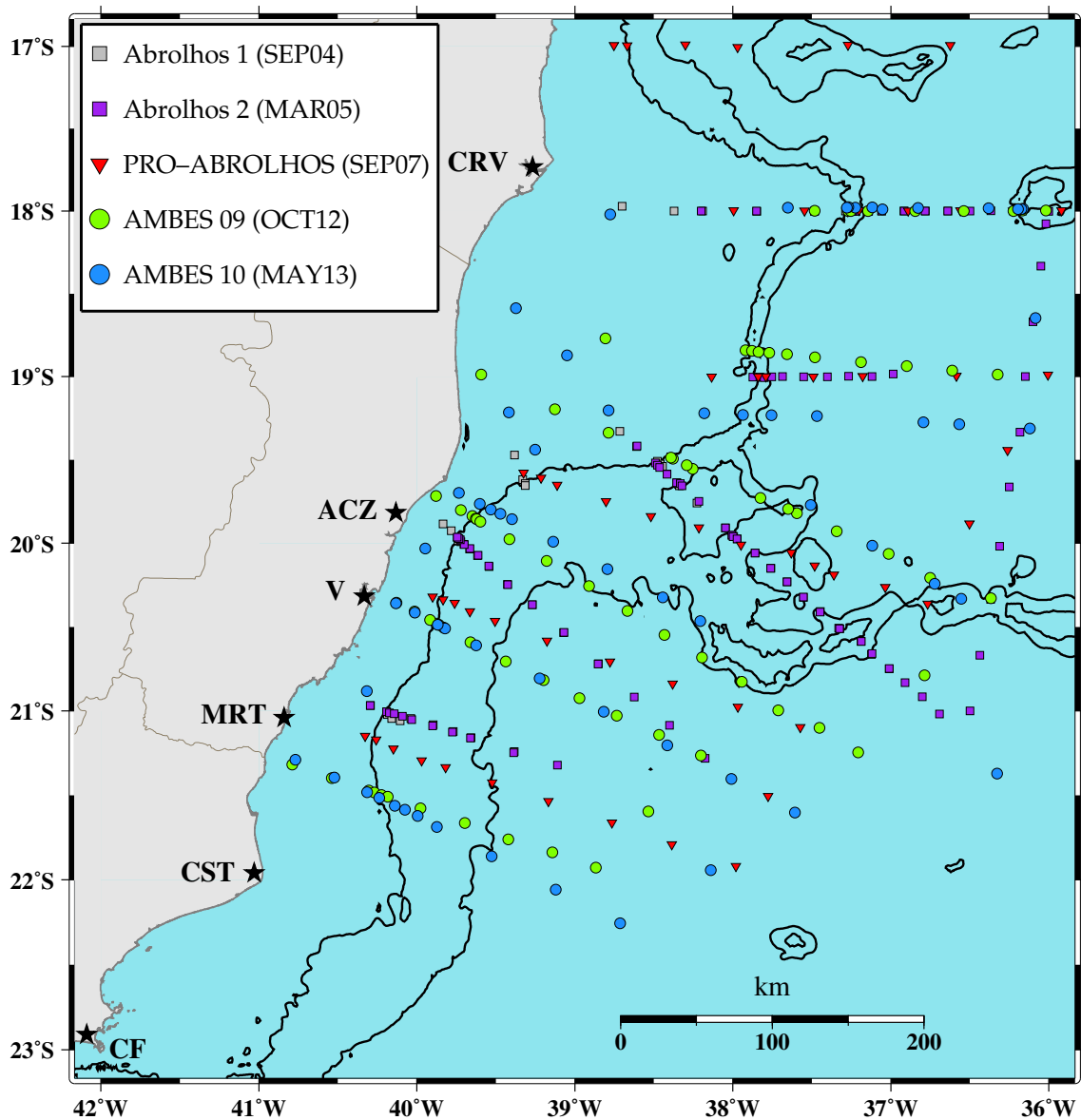


Figure 2.3: Representation of the *in situ* synoptic datasets within the study region. The upper-left map insert marks the location of the study area off the coast of South America (red rectangle). The locations marked by the black stars are as in Figure 2.1. The black lines are the 100 m and 2000 m isobaths, derived from the 30-arcsecond SRTM30-plus dataset (updated from *Smith & Sandwell, 1997*).

2.3 Numerical models

2.3.1 Numerical and parametric modeling setup

We employ the Regional Ocean Modeling System (ROMS, *Shchepetkin & McWilliams, 2005*), which has already been successfully implemented in the ESB (e.g., *Soutelino et al., 2013*). ROMS is a free-surface, terrain-following coordinate model that

solves the primitive equations of motion under the Boussinesq and hydrostatic approximations.

The west boundary is closed and the east, south and north boundaries are open. Different forms of radiation/nudging boundary conditions are used for the tracers and barotropic/baroclinic velocity components. Harmonic (*i.e.*, Laplacian) lateral mixing is used for momentum and tracers. Momentum (tracer) mixing is computed along S -surfaces (geopotential surfaces). A sponge layer with ≈ 15 grid points was used at the open boundaries, where the horizontal viscosity coefficient A_H was linearly ramped from its interior value of $10 \text{ m}^2 \text{ s}^{-1}$ to $100 \text{ m}^2 \text{ s}^{-1}$ at the open boundaries. The vertical viscosity coefficient A_V is found at each time step with the Mellor–Yamada level–2.5 turbulent closure scheme (*e.g.*, [Wijesekera et al., 2003](#)). Bottom stress was parameterized using a quadratic bottom drag law, with a canonical value of $C_D = 3 \times 10^{-3}$.

The horizontal grid is rectangular (spanning the 41.6°W – 36.1°W , 23.3°S – 18.2°S longitude–latitude box) and has an average resolution of ≈ 930 m. The form of the vertical stretching curve was chosen such that the spacing of the 50 vertical S -levels was no coarser than 45 m. Bottom topography from an updated version of the [Smith & Sandwell \(1997\)](#) dataset (SRTM30-plus dataset, available at http://topex.ucsd.edu/WWW_html/srtm30_plus.html) is used. The 30-arcsecond raw topography data was linearly interpolated to the model grid, and capped at 1200 m. The topography was then smoothed with a Hanning window.

The stretching curve, the number of vertical levels, the amount of smoothing applied and the maximum model depth were chosen to bring the spurious velocities produced by the Horizontal Pressure Gradient Errors (HPGEs) to a tolerable level, while maintaining a reasonable computational cost and retaining desired morphological features. The optimal combination of grid parameters was that which minimized the quantities $\Delta h/h$ ([Beckmann & Haidvogel, 1993](#)) and $\Delta z/z$ ([Haney, 1991](#)). These ratios quantify the hydrostatic consistency of the grid, by means of the maximum steepness of the bottom topography and inte-

rior S-surfaces, respectively. $\Delta h/h \equiv (h_i - h_{i-1})/(h_i + h_{i-1})$, where h is the depth of a grid cell and i is an index in either horizontal direction. $\Delta z/z \equiv (z_{i,k} - z_{i-1,k} + z_{i,k-1} - z_{i-1,k-1})/(z_{i,k} + z_{i-1,k} - z_{i,k-1} - z_{i-1,k-1})$ is like a three-dimensional version of $\Delta h/h$. The final value of each of these parameters is the absolute maximum found after iterating over all grid cells in both horizontal directions.

The effects of the seamount chain (the VTR) and the smaller-scale topographic features on the continental shelf were examined using two separate grids, different only with respect to bottom topography. On the first grid, the topography underwent the least possible smoothing, with the single purpose of decreasing the HPGEs. On the second grid, the seamount chain was totally removed, and the topography was further smoothed to filter out the smaller-scale topographic features of the continental margin. A comparison of the rough and smooth topographies is shown in [Figure 2.4](#).

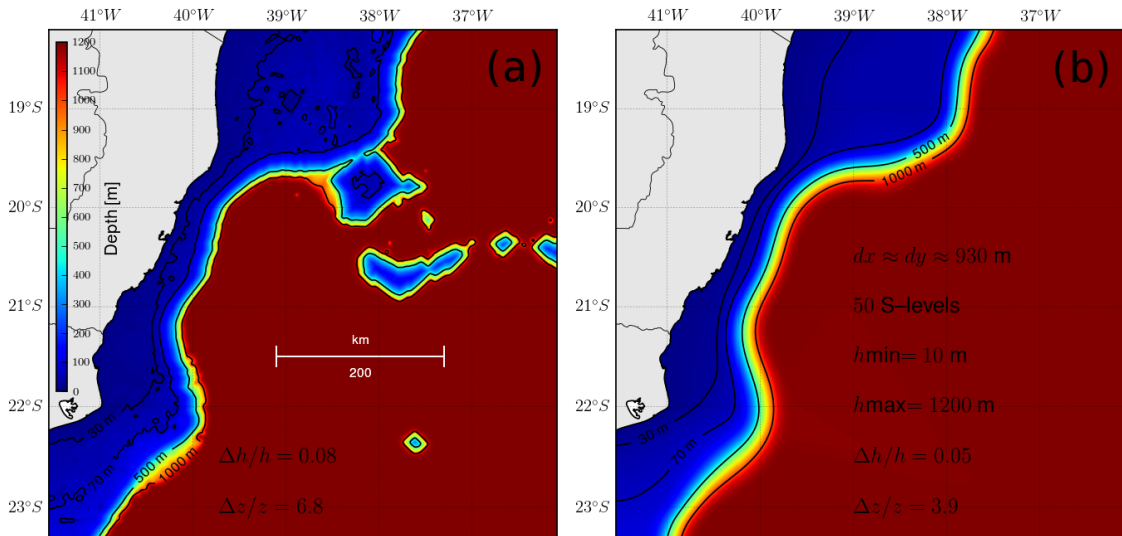


Figure 2.4: Bottom topographies used in the simplified model experiments. **(a)**: Rough (realistic) topography grid. **(b)**: Smooth (idealized) topography grid. Model grid details are shown on the right panel, and are identical for both grids, except for the hydrostatic consistency ratios $\Delta h/h$ and $\Delta z/z$.

Flat stratification scenario

The flat-stratification initial conditions were derived from the WOA13 temperature and salinity fields. First, the summer climatological profiles shallower than 200 m were averaged together over the ESB (22°S–18°S), to produce a rough rep-

resentation of the mean summer stratification on the continental shelf. Then, a rectangular area to the south of the VTR and away from the shelf edge was chosen to produce a second pair of spatially-averaged T-S profiles, meant to represent the deep-ocean stratification. The distance to the shelf edge was chosen to be 10 first-mode baroclinic radii of deformation (L_d), with $L_d \approx 40$ km (*Houry et al., 1987*). This choice was motivated by the desire to represent an ocean approximately at rest, where the stratification is not perturbed by the signal of a western boundary current in thermal wind balance. The shallow and deep profiles were then merged smoothly and interpolated to the vertical model grid at all horizontal grid points.

Brazil Current parameterization

The BC was parameterized using the methodology known in the literature as Feature-Oriented Regional Modeling System (FORMS, *Gangopadhyay & Robinson, 2002*). Briefly, FORMS consists of empirically-analytically parameterizing the water mass and velocity structures of regional synoptic features (*e.g.*, fronts or eddies) using parameters chosen on the basis of previous observational knowledge.

Within the FORMS framework, we chose the velocity-based backward approach (*Lozano et al., 1996; Gangopadhyay & Robinson, 2002*). This approach consists of parameterizing the velocity field of the chosen synoptic feature, and then deriving the tracer fields from it. The BC jet structure was parameterized as a surface-intensified, isobath-following Gaussian jet, using the formulation of *Soutelino et al. (2013)*. The mass structure (*i.e.*, the temperature and salinity fields) was calculated from the velocity field assuming that the jet is in thermal wind balance with the density field. Details of this methodology are found in *Soutelino et al. (2013)*.

The parameters chosen for the model BC jet are intended to represent the approximate core velocity, volume transport and geometry (width and vertical extent) of the real BC as observed within the ESB (*e.g.*, *Miranda & Castro, 1982; Evans et al., 1983; Stramma et al., 1990; Rodrigues et al., 2007; Silveira et al., 2008; Arruda*

et al., 2013). The transport (core velocity) was -3.2 Sv (-50 cm s $^{-1}$). The Gaussian width (depth) of the jet was 80 km (150 m).

Mass conservation was prescribed along the north (incoming flow) and south (outgoing flow) boundaries, with a variable Coriolis parameter in the thermal wind relation. No flow through the east boundary was prescribed. The Intermediate Western Boundary Current jet, whose core lies typically at ≈ 800 m (*e.g.*, *Boebel et al.*, 1999; *Legeais et al.*, 2013) was not parameterized, under the assumption that it is not a relevant direct forcing of the intrusions of SACW onto the continental shelf.

Model wind forcing

The steady wind forcing employed in the numerical experiments is spatially-uniform and upwelling-favorable (southwestward). The wind stress was linearly ramped to its full magnitude (0.072 N m $^{-2}$) over a local inertial period (≈ 34 h). The magnitude of the model wind forcing was chosen based on the time-mean of the along-shelf component of the wind stress (τ^{sy} , parallel to the $\approx 40.5^\circ$ coastline tilt) taken over the summer months (January–March), and averaged over the TB shelf area. The τ^{sy} series was derived from the time-average of the 1988–2013 daily scatterometer dataset, considering only upwelling-favorable (*i.e.*, $\tau^{sy} < 0$) snapshots. The wind stress vector $\vec{\tau}^s = (\tau^{sx})\hat{x} + (\tau^{sy})\hat{y}$ was derived from the wind velocity vector $\vec{U} = (U^x)\hat{x} + (U^y)\hat{y}$ 10 m above the sea surface using the standard bulk formula $\vec{\tau} = \rho_a C_{Da} \|\vec{U}\| \vec{U}$, where \hat{x} , \hat{y} are the unit vectors in the cross-shelf and along-shelf directions, respectively, ρ_a is the air density (assumed to be 1.226 kg m $^{-3}$) and C_{Da} is the drag coefficient. C_{Da} was parameterized using the traditional formula from *Large & Pond* (1981), modified for low wind speeds according to *Trenberth et al.* (1990).

2.3.2 Process-oriented simplified experiments

In this study, we chose a process-oriented approach, in which the responses of the system to different forcing scenarios are diagnosed and compared. A set of

semi-idealized numerical experiments was designed to investigate the individual and combined effects of bottom topography, wind forcing and deep-ocean forcing. Here, deep-ocean forcing is taken to mean the effects of the time-mean BC jet, without mesoscale eddies. Specifically, we performed each experiment with different combinations of the following features: 1) Either flat stratification (horizontal isopycnals) or BC stratification (tilted isopycnals); 2) Either smooth (idealized) or rough (realistic) topography and 3) Either no wind forcing or steady wind forcing.

In this process-oriented framework, we first sought a BC-free scenario with flat stratification, and then compared it with a stratification scenario typical of an idealized, mean BC jet. The comparison of the model results in both scenarios provided insight on the role of the mean baroclinic signal of the BC, *i.e.*, the intrinsic uplifting of isopycnals linked to the geostrophic shear of the current, and other effects related to the interaction of the BC flow with the continental shelf. **Table 2.1** summarizes the set of process-oriented experiments performed.

Each experiment was run for 21 local inertial periods (one local inertial period ≈ 34 h), or ≈ 30 days. Instantaneous outputs were averaged over half an inertial period. In the following sections, the model fields described are time-averages of the entire 30-day simulation, unless otherwise noted. The rationale for this choice is that experiments with the BC develop energetic instabilities along the continental slope, therefore introducing unwanted time-dependent biases on the instantaneous fields. This effect was minimized by averaging over the first 30 days of the simulation. The choice of averaging over this amount of time was motivated by the fact that, in runs where the idealized BC is present, the shelf-averaged horizontal kinetic energy completes approximately two periods in 30 days (not shown).

2.3.3 Realistic experiment

As an independent verification of our interpretations of the simplified, process-oriented ROMS experiments, we used outputs from a more complete regional

Table 2.1: Outline of the process-oriented numerical experiments performed with ROMS.

Experiment	Initial/boundary conditions	Topography	Wind forcing
EXP-smoo-1	Flat stratification	Smooth	Steady
EXP-smoo-2	Mean BC jet	Smooth	None
EXP-smoo-3	Mean BC jet	Smooth	Steady
EXP-real-1	Flat stratification	Rough	Steady
EXP-real-2	Mean BC jet	Rough	None
EXP-real-3	Mean BC jet	Rough	Steady

nested implementation of the Hybrid Coordinate Ocean Model (HYCOM), originally analyzed by *Arruda et al. (2013)*. First, the coarser ($1^\circ/4$ horizontal resolution) parent simulation was run for the entire Atlantic Basin (65°S – 60°N) from 1948 through 2009, initialized with climatological fields and forced with monthly means of atmospheric reanalysis fields. Next, a finer ($1^\circ/24$ horizontal resolution) child grid for the western South Atlantic region (54°W – 32°W and 34°S – 12°S) was run from 2004 through 2009, forced with the same atmospheric products as the parent simulation and with lateral boundary conditions derived from the parent simulation fields. For details, the reader is referred to *Arruda et al. (2013)*.

2.4 South Atlantic Central Water intrusion pathways

In this section, we examine the pathways through which SACW may enter the shelf. We begin with simple analyses of the hydrographic observations, and then seek more detailed evidence in the simplified and realistic numerical solutions.

2.4.1 Observational setting

One of the striking features of the ESB is seasonal coastal upwelling. This process is relevant to the present study because it is well-known that the cold water that outcrops during coastal upwelling events has a high SACW content. Therefore, investigating the surfacing of the thermocline in the ESB is likely to provide insight on the intrusion processes we are ultimately concerned with.

Satellite-derived SST images found in previous studies reveal a SST minimum on the shelf centered at $\approx 21^\circ\text{S}$, which is most intense during summer (e.g., *Mazz-*

ini & Barth, 2013, their Figure 5). The summer climatological SST field shown in **Figure 2.5a** supports these observations, depicting a signal that is likely the result of the averaging of transient coastal upwelling plumes. This climatological plume has a minimum temperature of $\approx 24.5^{\circ}\text{C}$, originates at $\approx 19.5^{\circ}\text{S}$ and widens downstream, reaching the shelf edge at $\approx 21^{\circ}\text{S}$.

The wind regime is, on average, strongly upwelling–favorable. Considering the time series derived from the daily scatterometer dataset, the along–shelf component of the wind stress vector τ^{sy} was upwelling–favorable 80 % of the time in the period 01/01/2002–09/02/2013. This result highlights the likely leading–order effect of the wind forcing in coastal upwelling in the ESB. A similar conclusion was reached for the Cape São Tomé area (22°S), where τ^{sy} was upwelling–favorable 78 % of the time between 2000 and 2011 (*Palóczy et al., 2014*).

The question of how the SACW gets to the coast before outcropping then arises. Does it penetrate on the shelf locally or upstream (north) of the SST minimum? As a first attempt to answer this question, a simple analysis of the near–bottom temperature observations was done, as the cold SACW signal is observed roughly in the lower half of the water column, and is bottom intensified. **Figure 2.5b** shows a map of near–bottom temperature, indicating stations where SACW was observed. The 21°C isotherm was chosen as a tracer for SACW. This choice was based on the knowledge that the average SST observed during upwelling events within the ESB is $\approx 21^{\circ}\text{C}$ (*Castro et al., 2006*). During four of the five synoptic scenarios analyzed, SACW was observed at least once at every alongshore location sampled between 19.5°S and 21.5°S . The only exception was the MAY13 survey, when no water colder than 22.3°C was observed inshore of the 100 m isobath. SACW was not observed to the north of 19.5°S (**Figure 2.5c**). The lowest temperature observed on the shelf was 16.4°C , around the 50 m isobath at the southernmost transect of the OCT12 survey. Evidently, this result does not mean that SACW never enters the shelf north of 19.5°S . Rather, it suggests that intrusion events tend to be more common to the south of the seamount chain (the Vitória–Trindade Ridge, VTR), all along the Tubarão Bight (TB) and the southern flank of the wide Abrolhos

Bank (AB).

The scattered Temperature–Salinity (T – S) diagram in [Figure 2.5b](#) highlights the typical water mass structure on the ESB shelf. Warm and salty TW in the mixed layer interfaces with cold and fresh SACW advected onshore from the oceanic pycnocline, with little evidence of a modified (fresher) coastal water mass. This stresses the point made in the previous paragraph, as the water with highest SACW content (coldest and freshest) is observed to the south of the seamount chain (VTR) rather than to the north of it.

The cross–shelf structure of the temperature field in the ESB ([Figure 2.5d](#)) reveals the well–known presence of the BC jet. The thermocline (and the pycnocline) is uplifted near the shelf edge, and a layer of relatively cold, fresh and dense water occupies the shelf. There is a variety of possible physical mechanisms related to the BC that may play a role in the intrusions of SACW. Perhaps the simplest of those is the fact that colder branches of SACW are available at the shelf edge simply due to the presence of the BC there. It will be argued that this uplifting of the main thermocline is one of the leading–order deep–ocean mechanisms involved in the problem, as previously pointed out for other nearby upwelling systems such as the Cape São Tomé (22°S, [Palóczy et al., 2014](#)) and Cape Frio (23°S, [Cerdeira & Castro, 2014](#)) areas.

Buoyancy arrest and frictional spindown predictions

If along–shelf scales are assumed to be much larger than cross–shelf scales, the nature of the response of the shelf circulation to wind forcing in the low–frequency band (*i.e.*, days to weeks³) is expected to be dominated by the barotropic mode when the quantity $S^2 = \alpha^2 N^2 / f^2$ is small (where α , N and f are representative values for the bottom slope, buoyancy frequency and Coriolis parameter, respectively). Furthermore, the wind–driven flow fluctuations at the shelf edge are expected to be negligible compared to fluctuations near the coast when $S = \alpha N / f$ is small ([Clarke & Brink, 1985](#)), meaning that the entire wind–driven flow is trapped within the shelf and has little effect on the circulation in the shelf edge area. It is

³Synoptic–scale atmospheric systems, in the so–called “weather band”.

therefore insightful to estimate S from the CTD data.

Table 2.2 shows shelf-averaged (stations shallower than 100 m) values for each of the five surveys within the TB area. The average bottom slope in the TB area is $\alpha = 2.3 \times 10^{-3}$, and a reference absolute value for the Coriolis parameter is $f = 5.1 \times 10^{-5} \text{ s}^{-1}$. S^2 varied between 0.10 and 0.85, and S between 0.32 and 0.92. This implies that a significant baroclinic response is predicted throughout the shelf, and that the low-frequency wind-driven circulation at the shelf edge is expected to have a non-negligible amplitude. This picture stands in contrast with regions where S^2 is much smaller and the shelf response is quasi-barotropic, such as the wintertime South Brazil Bight ($S^2 = 1.6 \times 10^{-4} - 1.9 \times 10^{-2}$, *Stech & Lorenzetti, 1992*), the São Paulo Continental Shelf ($S^2 = 2.2 \times 10^{-4} - 3.0 \times 10^{-4}$, *Dottori & Castro, 2009*)⁴ or the wintertime West Florida Shelf ($S^2 = 5.0 \times 10^{-5}$, *Clarke & Brink, 1985*). The baroclinic response to low-frequency wind forcing in the TB shelf is not expected, however, to be as energetic as in other regions, such as the Peruvian shelf ($S^2 = 1.10 - 2.25$, *Clarke & Brink, 1985; Lentz & Chapman, 2004*).

Another implication of the size of S is how effective buoyancy arrest is expected to be. In a stratified, sloping bottom Ekman layer, cross-shelf buoyancy advection produces a horizontal density gradient, which brings the near-bottom along-shelf velocity (hence along-shelf bottom stress) to rest through thermal wind shear. The absence of bottom stress implies no bottom Ekman transport. This mechanism is known as buoyancy arrest (*e.g.*, *Garrett et al., 1993; Brink & Lentz, 2010*). A rough estimate of the timescale T_{buoyancy} over which this phenomenon is expected to occur is given by the quantity $(S^2 f)^{-1}$ (*Garrett et al., 1993*). For the five datasets considered here, T_{buoyancy} varies from 55 h to 7 h, with a mean value of 15 h. This suggests that buoyancy arrest may happen fast enough in the strongest SACW intrusion events, where the shelf-averaged N^2 is largest, and T_{buoyancy} is shortest. However, a more thorough examination of the potential importance of buoyancy arrest would have to account for its along-shelf scale (*Brink, 2012*).

⁴The São Paulo Continental Shelf ($\approx 23^\circ\text{S} - 26^\circ\text{S}$) is located in the central part of the South Brazil Bight ($\approx 22^\circ\text{S} - 28.5^\circ\text{S}$). In fact, *Dottori & Castro (2009)* applied *Clarke & Brink (1985)*'s numerical model to this region, showing that it effectively predicts moored velocity observations.

Alternatively, the wind-driven flow may simply undergo frictional adjustment before buoyancy arrest takes place. A first estimate of the frictional adjustment timescale T_{friction} is given by the quantity H/r (e.g., [Brink, 1998](#)), where H is the local depth and r is a linear bottom resistance coefficient. Assuming a canonical value of $3 \times 10^{-4} \text{ m s}^{-1}$ for r , T_{friction} is 65 h at the 70 m isobath, and 19 h at the 20 m isobath. Compared to the 7 h–55 h estimated range for T_{buoyancy} , it seems that a combination of buoyancy- and friction-induced adjustment of the flow should be expected, with the buoyancy effects possibly being more important during stronger SACW intrusion events.

Table 2.2: Shelf-averaged stratification frequency squared (N^2), slope Burger number ($S \equiv \alpha N/f$) and its square for the Tubarão Bight (TB) area (19.5°S–22°S).

Survey	N^2 [10^{-4} s^{-2}]	$\alpha^2 N^2 / f^2$	$\alpha N / f$
SEP04	1.03	0.22	0.46
MAR05	4.10	0.85	0.92
SEP07	0.49	0.10	0.32
OCT12	2.10	0.44	0.66
MAY13	1.16	0.24	0.49
Average	1.78	0.37	0.57

2.4.2 Model kinematics of SACW intrusions

While the synoptic observations discussed in the previous section yield some qualitative conclusions on the SACW intrusions, a more detailed examination of the pathways and physical mechanisms involved require a numerical approach. We start by looking at the passive tracer (dye) fields from the process-oriented numerical experiments.

Passive tracer distributions

The dye fields were initialized by setting the dye concentration (in kg m^{-3}) to be numerically equal to the local depth (in meters) at each grid point. [Figure 2.6](#) presents snapshots of horizontal distributions of the fractional thickness of the layer occupied by water initially offshore of the 70 m isobath (approximately the shelfbreak depth). In other words, it shows the thickness of the layer occupied by

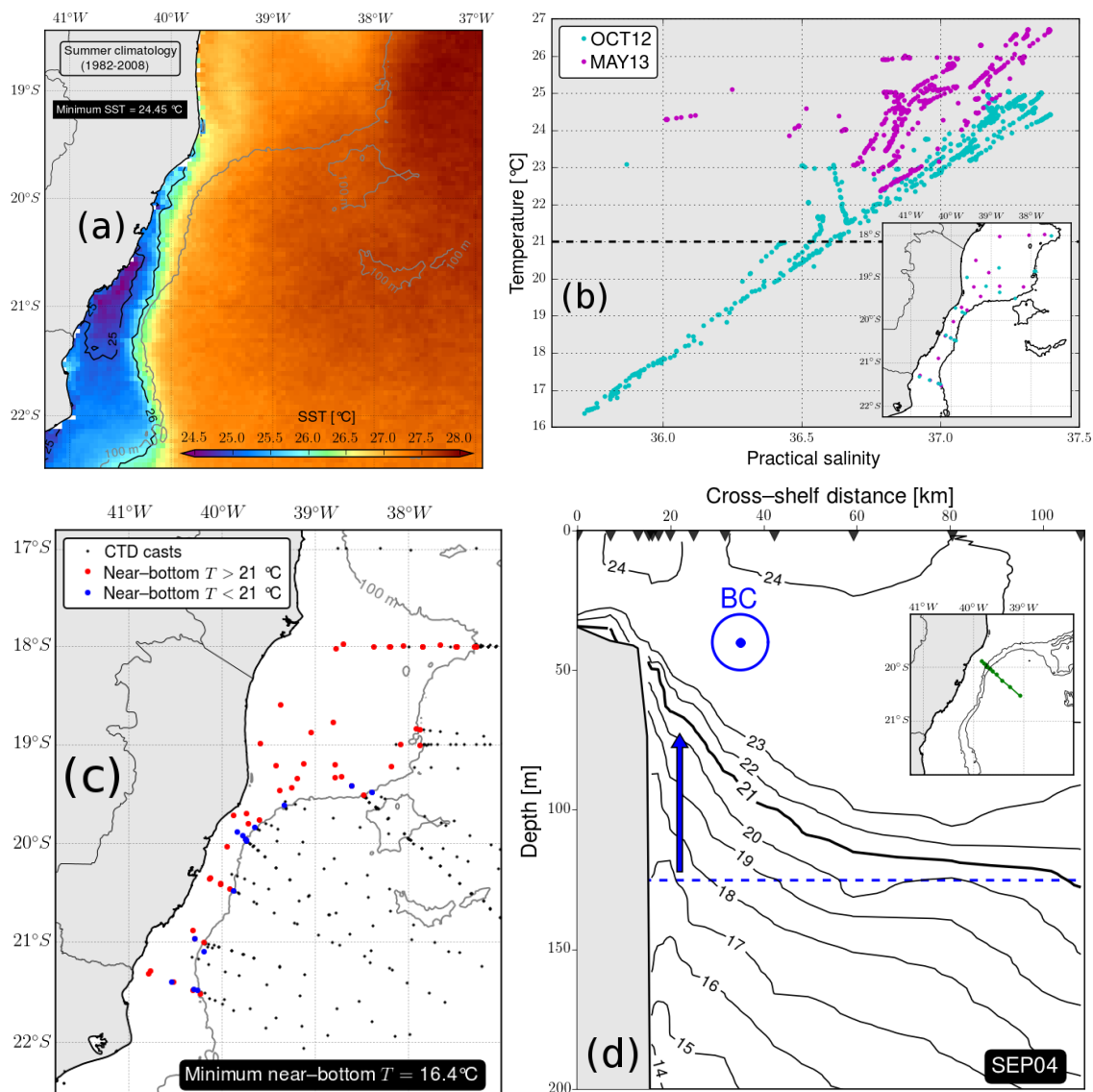


Figure 2.5: Hydrographic observations in the ESB shelf. **(a)**: Sea Surface Temperature (SST) summer climatology. **(b)**: Scattered $T-S$ diagram for two contrasting hydrographic snapshots: Cyan (magenta) dots correspond to a scenario with (without) SACW on the shelf. **(c)**: Near-bottom temperature map derived from all CTD casts of the five synoptic cruises. The black dots mark the locations of all CTD casts. The blue dots mark the casts shallower than 100 m where the near-bottom temperature was lower than 21°C (a qualitative evidence of water with high SACW content). **(d)**: Cross-shelf temperature section from the SEP04 survey (September/2004) along a transect at the narrowest part of the shelf. The black triangles along the top of the figure mark the along-transect positions of the CTD casts. The green dots on the map insert mark the position of the CTD casts within the ESB. The blue dashed line marks the approximate depth of the 21°C isotherm in a hypothetical scenario without the BC.

water with dye concentration equal to or greater than 70 kg m^{-3} , divided by the local depth.

Figure 2.6 shows that slope water tends to penetrate the shelf mostly within the TB area, in agreement with the qualitative picture suggested by the observations. This intrusion area is active under all forcing scenarios (wind-only, BC-only and wind+BC), although clearly only wind forcing is capable of driving slope water all the way to the inner shelf. The rough topography scenarios show more irregular distributions, although the overall spatial patterns are similar to those in their smooth topography counterparts. We therefore discuss only the smooth topography experiments in the following sections. However, there seems to be an additional intrusion spot on the southern flank of the AB, which is more evident in the wind-driven rough topography scenarios (Figure 2.6b,d). This suggests that some kind of local mean flow-topography interaction process could be relevant there, in addition to the tide-topography interaction mechanisms suggested by *Pereira et al. (2005)*.

Unlike the wind-driven intrusions, the BC-driven intrusions occupy the entire water column, and are therefore likely to cause TW to penetrate the outer shelf along with the SACW in certain parts of the TB area. This point is demonstrated by the slope water layer thickness distributions in the BC-only scenarios, which are equal to the local depth near the shelfbreak (Figure 2.6e,f). In contrast, the wind-driven experiments show bottom-intensified SACW intrusions farther onshore on the TB shelf, followed by a top-bottom slope water layer within the coastal upwelling plume (Figure 2.6a,b,c,d).

Velocity and temperature distributions

The surface and near-bottom temperature and velocity distributions from both EXP-smoo-1 (wind-only) and EXP-smoo-3 (wind+BC) show minor differences (Figure 2.7, upper and middle rows). Both realistically reproduce the shape of the coastal upwelling plume, as noted by their similarity with the observed climatological SST pattern (Figure 2.5a). The primary difference is that EXP-smoo-3

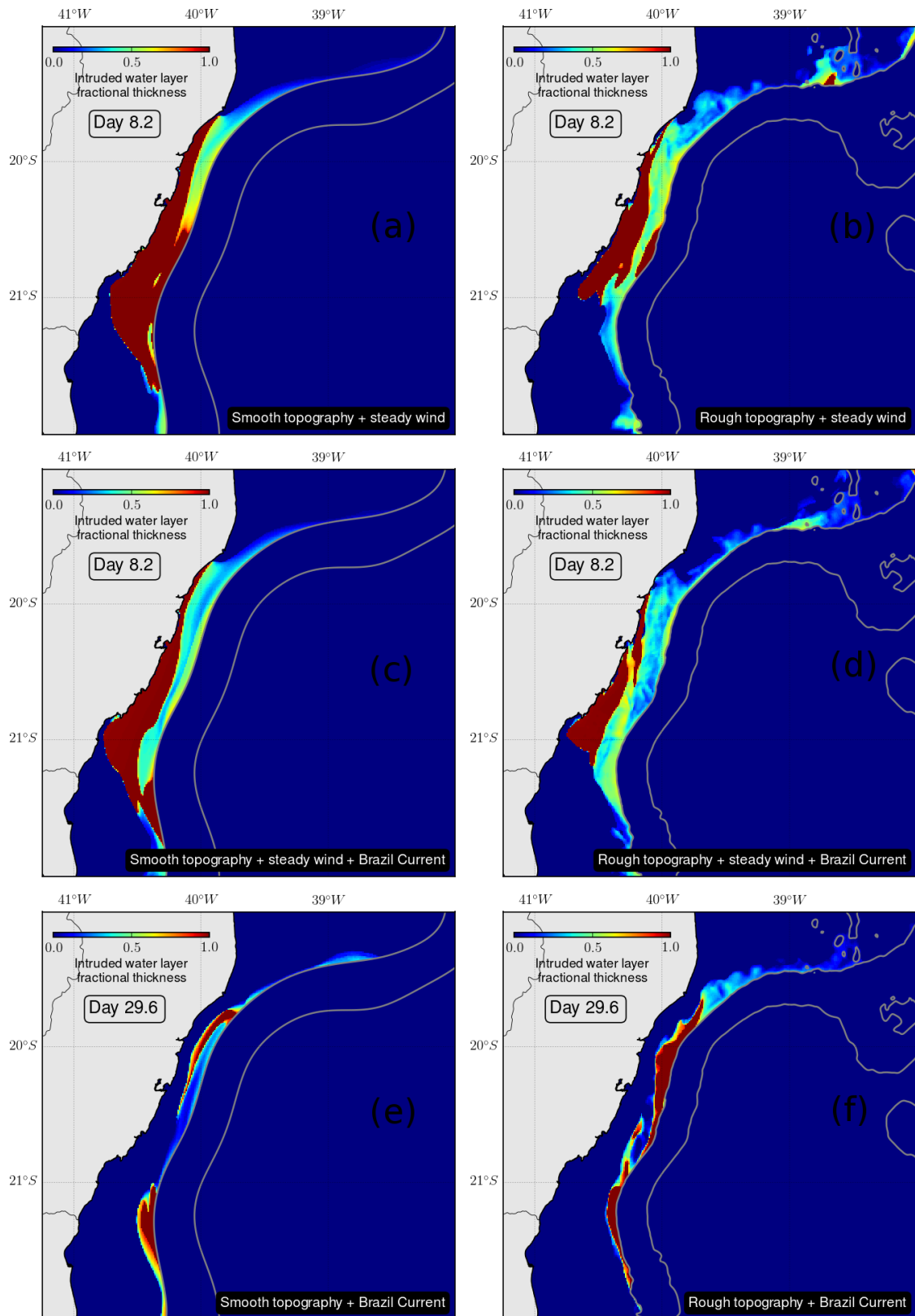


Figure 2.6: Instantaneous maps of the thickness of the layer occupied by intruded water on the shelf. In red areas, the entire water column is occupied by water that was located offshore of the 70 m isobath (approximately the shelfbreak depth) in the initial conditions. In blue areas, no water originally offshore of the shelfbreak is present. **(a,c,e)**: Smooth topography experiments. **(b,d,f)**: Rough topography experiments. **(a,b)**: Wind-only experiments. **(c,d)**: Wind + Brazil Current experiments. **(e,f)**: Brazil Current-only experiments. In the wind-forced experiments **(a,b,c,d)** the instantaneous fields are shown for model day 8.2, near the end of the spinup of the shelf circulation. In the BC-only experiments **(e,f)**, the instantaneous fields are shown for the last model day (29.6), because the features in the dye fields take longer to develop. The thick gray lines represent the 70 m and 1000 m isobaths.

produces colder SACW intrusions.

The near-bottom temperature and velocity distributions from the simplified experiments reveal two major pathways of SACW intrusion within the TB and one in the southern flank of the AB (Figure 2.7b,d). The realistic Hybrid Coordinate Ocean Model (HYCOM) simulation has a coarser horizontal resolution (≈ 4.5 km) than the simplified ROMS experiments, and therefore is not expected to represent the coastal circulation as well as the deep-ocean circulation⁵. Despite this limitation, some snapshots from the realistic simulation do represent similar intrusion pathways (e.g., Figure 2.7f).

The model temperature and cross-isobath velocity vertical structures along the TB shelfbreak are consistent with the dye distributions, in that the onshore flow occupies the lower half of the water column in the wind-driven scenarios, but spreads throughout the water column and is surface-intensified in EXP-smoo-2 (BC-only, Figures 2.8 and 2.9). This again suggests that standard cross-shelf surface Ekman transport divergence may be the lowest order mechanism responsible for the SACW intrusions in the TB. The maximum onshore velocity is ≈ 9 cm s⁻¹ and ≈ 7 cm s⁻¹ in EXP-smoo-3 and EXP-smoo-1, respectively, but only ≈ 2 cm s⁻¹ in the EXP-smoo-2. In both wind-driven scenarios, the maximum onshore velocity is not found near the bottom, as classic, homogeneous Ekman Theory suggests. Rather, it is found at mid-depth (≈ 30 – 40 m), consistent with the theoretical predictions of *Lentz & Chapman (2004)* for the parameter range $S \equiv \alpha N/f \approx 1$ ($S \approx 1$ in the estimates for the most strongly stratified cases observed in the TB, see Table 2.2). In the theory of *Lentz & Chapman (2004)*, this mid-depth intensification of onshore flow is linked to the divergence of nonlinear cross-isobath momentum advection. Besides this mechanism, local acceleration or an along-isobath pressure gradient force can also produce an additional onshore return flow.

The maximum onshore velocity is located at the narrowest part of the shelf ($\approx 20^\circ\text{S}$). It is there that the thermocline is shallowest in both wind-driven scenarios, where water as cold as 22°C and 19.5°C is found in EXP-smoo-1 (wind-only)

⁵details on the model verification are found in *Arruda et al. (2013)*.

and EXP-smoo-3 (wind+BC), respectively. This difference also suggests that the effect of thermocline uplifting by the BC is important in modifying the source water temperature, causing colder branches of SACW to enter the shelf.

Another point worth stressing is the qualitative similarity between the cross-isobath velocity sections in both wind-driven scenarios. The local maxima and minima in the EXP-smoo-3 scenario (wind+BC) seems to be very similar to the sum of the EXP-smoo-1 (wind-only) and EXP-smoo-2 (BC-only) scenarios (Figure 2.8). In fact, the normalized root mean square difference between EXP-smoo-3 and the sum of EXP-smoo-1 and EXP-smoo-2 is only 7.8 %. This indicates that, in the shelfbreak area, the total model cross-isobath circulation is almost a linear combination of the individual effects of the wind and BC forcings.

The cross-shelf temperature distributions further stress the depth-dependent character of the SACW intrusions within the TB. For both wind-driven scenarios, the three cross-shelf lines in Figure 2.9 show different regimes. The southernmost line reflects the well-mixed character of the shelf and the offshore displacement of the coastal upwelling plume all the way to the shelf edge (Figure 2.9a,d). The middle line is located at the narrowest part of the shelf, where the maximum on-shore velocity is found, and where the thermocline is shallowest (Figure 2.8a,b). In this area, a mature coastal upwelling plume is found at ≈ 8 km from the coast (Figure 2.9b,e). The northernmost line reveals a clear bottom-trapped temperature front, but no coastal upwelling plume. The intrusions in EXP-smoo-2 (BC-only) are also consistent with the interpretation suggested by the dye distributions. No upwelling plume develops, and the uplift of the isotherms in the bottom-trapped temperature front is much gentler than in the wind-driven scenarios (Figure 2.9g,h,i).

2.5 Along-isobath momentum balance

At this point we have presented evidence that SACW tends to enter the ESB shelf at preferential along-shelf locations. But what are the physical mechanisms involved? We begin to address this question by examining the momentum budget

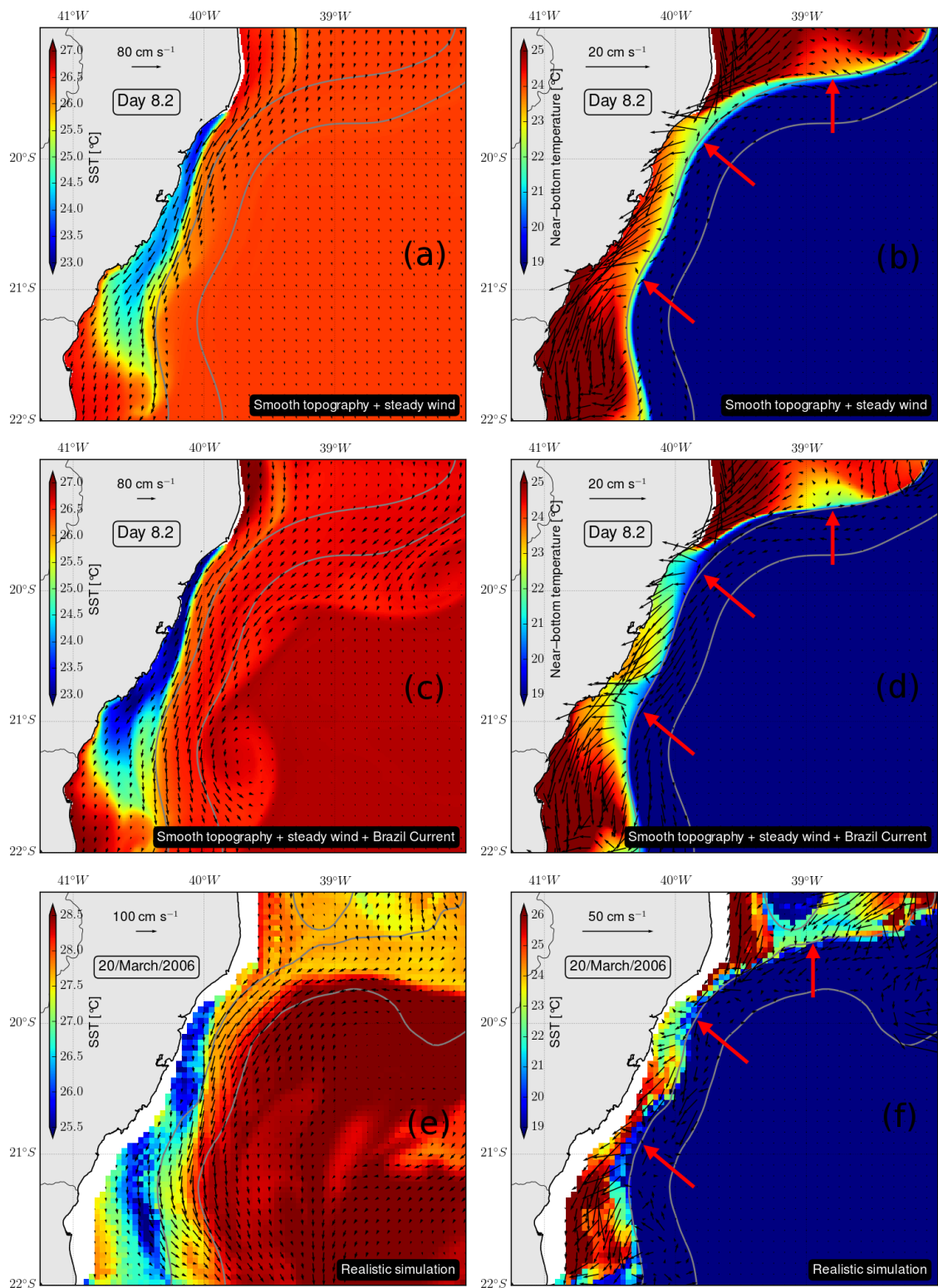


Figure 2.7: Instantaneous temperature (color shading) and velocity (vectors) at the surface and near the bottom. (a,b): EXP-smoo-1 simplified experiment (wind-only). (c,d): EXP-smoo-3 simplified experiment (wind+BC). (e,f): Realistic experiment. (a,c,e): Temperature and velocity at the surface. (b,d,f): Temperature and velocity near the bottom. The red arrows in the right column panels indicate preferential pathways of onshore flow. The gray lines mark the 70 m and 1000 m isobaths. For clarity, every tenth (second) vector is drawn in the upper and middle rows (bottom row).

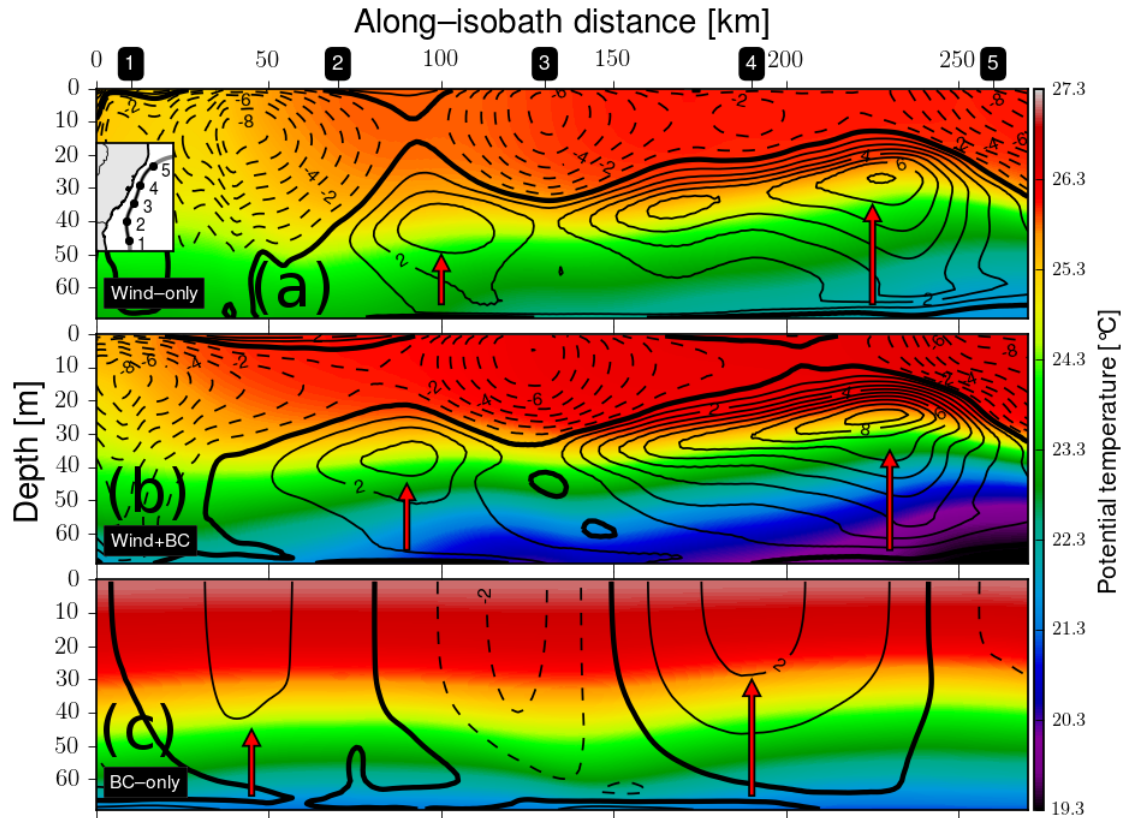


Figure 2.8: Run-averaged potential temperature (color shading) and cross-isobath velocity in cm s^{-1} (black contours) distribution along the 70 m isobath for the smooth topography scenarios. Solid (dashed) contours represent onshore (offshore) velocity. The heavy black line is the zero contour. (a): EXP-smoo-1 (wind-only). (b): EXP-smoo-3 (wind+BC). (c): EXP-smoo-2 (BC-only). The red arrows indicate preferential pathways of onshore flow of cold SACW. The markers labelled 1–5 along the x-axis of the top panel indicate along-isobath locations, which correspond to the dots on the map insert.

in the simplified numerical solutions.

2.5.1 Depth-dependent momentum balance along the shelf edge

First, we locally rotate each of the momentum balance terms to an isobath-following coordinate system, using the procedure described in *Gan et al. (2009)*. In this new coordinate system, \hat{y}^* (\hat{x}^*) is the along-isobath (cross-isobath) direction. \hat{y}^* (\hat{x}^*) is positive equatorward (offshore). The rationale for using this transformed framework of reference is that it is a more exact approach to the study of flows that deviate from geostrophy and transport mass across isobaths, breaking the Taylor–Proudman constraint. The along-isobath component of the momentum budget, with pressure in kinematic units (*i.e.*, divided by the Boussinesq reference

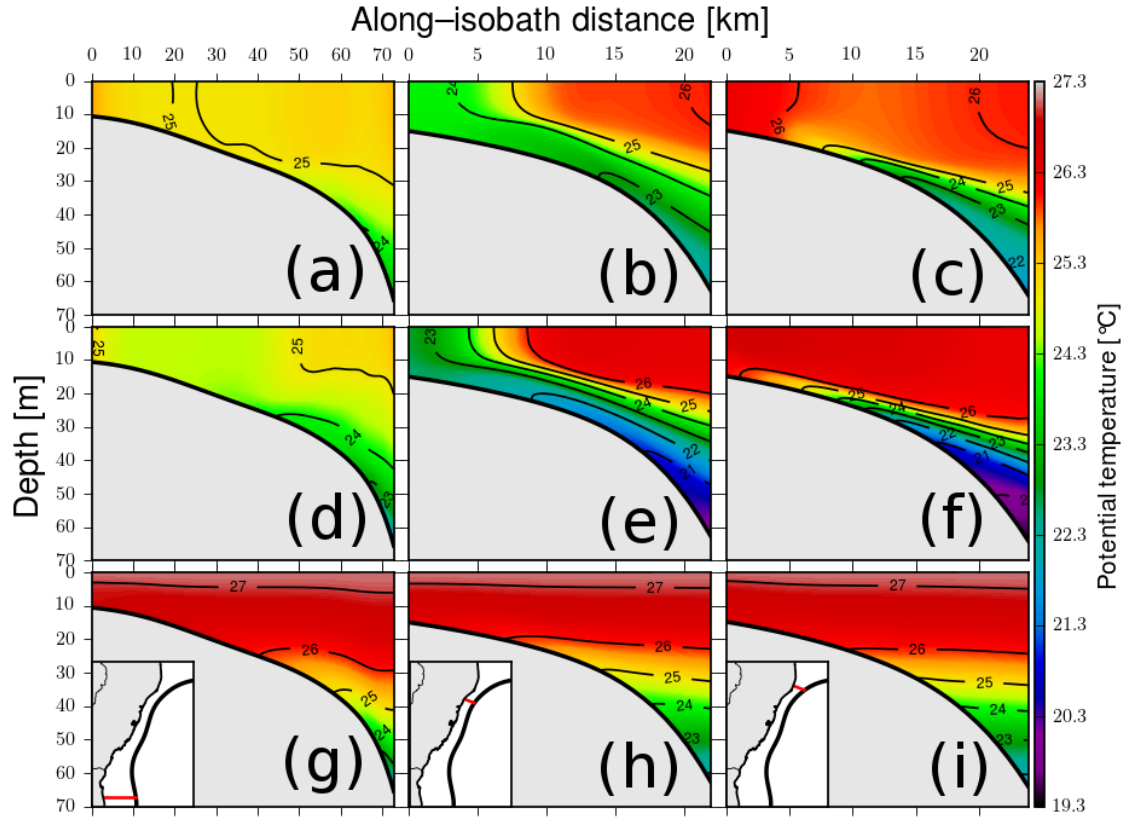


Figure 2.9: Run-averaged potential temperature along three cross-shelf lines for the smooth topography experiments. (a,b,c): EXP-smoo-1 (wind-only). (d,e,f): EXP-smoo-3 (wind+BC). (g,h,i): EXP-smoo-2 (BC-only). The left, middle and right columns each correspond to a different cross-shelf location, marked as a red line on the map inserts on the bottom panel of each column.

density $\rho_0 = 1025 \text{ kg m}^{-3}$) is

$$\underbrace{\frac{\partial v}{\partial t}}_{\text{ACCEL}_{y^*}} + \underbrace{u \frac{\partial v}{\partial x^*} + v \frac{\partial v}{\partial y^*} + w \frac{\partial v}{\partial z}}_{\text{NL}_{y^*}} + \underbrace{fu}_{\text{COR}_{y^*}} = \underbrace{-\frac{\partial p}{\partial y^*}}_{\text{PGF}_{y^*}} + \underbrace{\frac{\partial}{\partial z} \left(A_V \frac{\partial v}{\partial z} \right)}_{\text{VVIS}_{y^*}} + \underbrace{A_H \left(\frac{\partial^2 v}{\partial x^{*2}} + \frac{\partial^2 v}{\partial y^{*2}} \right)}_{\text{HVIS}_{y^*}}, \quad (2.1)$$

where u , v and w are the cross-isobath, along-isobath and vertical velocity components, respectively, f is the local inertial frequency, p is pressure and A_V (A_H) is the vertical (horizontal) turbulent viscosity coefficient. $\text{PGF}_{y^*} \equiv \frac{g}{\rho_0} \int_{\eta}^z \frac{\partial \rho}{\partial y^*} dz' - g \frac{\partial \eta}{\partial y^*}$ is the total along-isobath pressure gradient force per unit mass, with g being the acceleration due to gravity, ρ the total density and η the free-surface displacement and η the free-surface displacement. The along-isobath momentum balance relates directly to the cross-isobath circulation, and geostrophy was found to dominate the cross-isobath momentum balance in all experiments, as consistently supported by observational evidence for the subtidal mean flow on

most continental shelves (e.g., *Lentz & Chapman, 2004*, and references therein). For these reasons, only the along-isobath momentum balance is discussed here. In addition, due to the similarity between the wind+BC experiment (EXP-smoo-3) and the wind-only experiment (EXP-smoo-1), we restrict ourselves to comparing results from the wind-only (EXP-smoo-1) and BC-only (EXP-smoo-2) experiments.

Along the 70 m isobath (approximately the shelfbreak depth), there are areas where PGF_{y^*} is positive (i.e., equatorward, *Figure 2.10*). Part of this equatorward PGF_{y^*} gives rise to a geostrophically-balanced onshore flow, which has been found to be an important source of onshore transport in many continental shelves (e.g., *Scott & Csanady, 1976; Palma & Matano, 2009; Pringle & Dever, 2009; Gan et al., 2009, 2013; Xu et al., 2015; McCabe et al., 2015*). The PGF_{y^*} is surface-intensified in both EXP-smoo-1 (wind-only) and EXP-smoo-2 (BC-only), and tends to not change sign vertically. The EXP-smoo-2 scenario features a more clearly periodic pattern, with alternating areas of equatorward PGF_{y^*} (onshore geostrophic flow) and poleward PGF_{y^*} (offshore geostrophic flow). Finally, the amplitude of the PGF_{y^*} in EXP-smoo-1 is greater than the amplitude of the PGF_{y^*} in EXP-smoo-2 by a factor of ≈ 3 . This proportion is similar to the proportion between onshore velocities across the shelfbreak (*Figure 2.8a,b*).

The spatial patterns of the individual momentum advection terms ($u \frac{\partial v}{\partial x^*}$, $v \frac{\partial v}{\partial y^*}$ and $w \frac{\partial v}{\partial z}$) are qualitatively similar and nearly balance each other (not shown), leaving a net momentum advection NL_{y^*} that is $O(10^{-6}) \text{ m s}^{-2}$ or smaller. In all experiments, the local acceleration (ACCEL_{y^*}) and horizontal viscosity terms (HVIS_{y^*}) are everywhere $O(10^{-7}) \text{ m s}^{-2}$ or smaller, which is at least one order of magnitude smaller than the next-largest terms.

To close the momentum budget, it is helpful to examine the part of the PGF_{y^*} that is left unbalanced by the Coriolis acceleration, i.e., $\text{AGEO}_{y^*} \equiv -\frac{\partial p}{\partial y^*} - fu$. Within the geostrophic interior, this ageostrophic pressure gradient force is approximately balanced by net nonlinear momentum advection NL_{y^*} (*Figure 2.11*).

Therefore, away from the Ekman layers, the simplified momentum balance is

$$fu \approx -\frac{\partial p}{\partial y^*} - \text{NL}_{y^*}, \quad (2.2)$$

or geostrophic balance modified by net momentum advection. Considering the wind-driven case, the combination of this result with the mid-depth position of the maximum onshore return flow (Figure 2.8a) alludes to the dynamical regime predicted by *Lentz & Chapman (2004)* under strong stratification. Within the bottom Ekman layer, AGEO_{y^*} is approximately balanced by the vertical viscosity VVIS_{y^*} (Figure 2.12). The simplified momentum balance within the bottom Ekman layer is then

$$fu \approx -\frac{\partial p}{\partial y^*} + \frac{\partial}{\partial z} \left(A_V \frac{\partial v}{\partial z} \right), \quad (2.3)$$

or an Ekman-like balance modified by the PGF_{y^*} . This leading-order balance in the bottom Ekman layer has been found in other studies (e.g., *Palma et al., 2008; Palma & Matano, 2009*). The surface Ekman layer (in the wind-driven scenarios) appears to have a more complicated balance, requiring both NL_{y^*} and PGF_{y^*} to compensate the residue of the Ekman balance (not shown).

The picture that emerges from this model analysis is that of an energetic, geostrophic leading-order cross-isobath circulation at the shelf edge. The non-negligible PGF_{y^*} at the shelf edge is consistent with the predictions from *Clarke & Brink (1985)* for the observed values of the slope Burger number (Table 2.2). At next order, nonlinear effects and bottom stress seem to be important.

2.5.2 Depth-averaged momentum balance

A question now worth examining is what are the leading-order momentum and mass balances in a depth-averaged sense. Neglecting the highest-order terms (local acceleration and horizontal viscosity), the depth-averaged, along-isobath momentum balance with stresses in kinematic units (*i.e.*, divided by the Boussi-

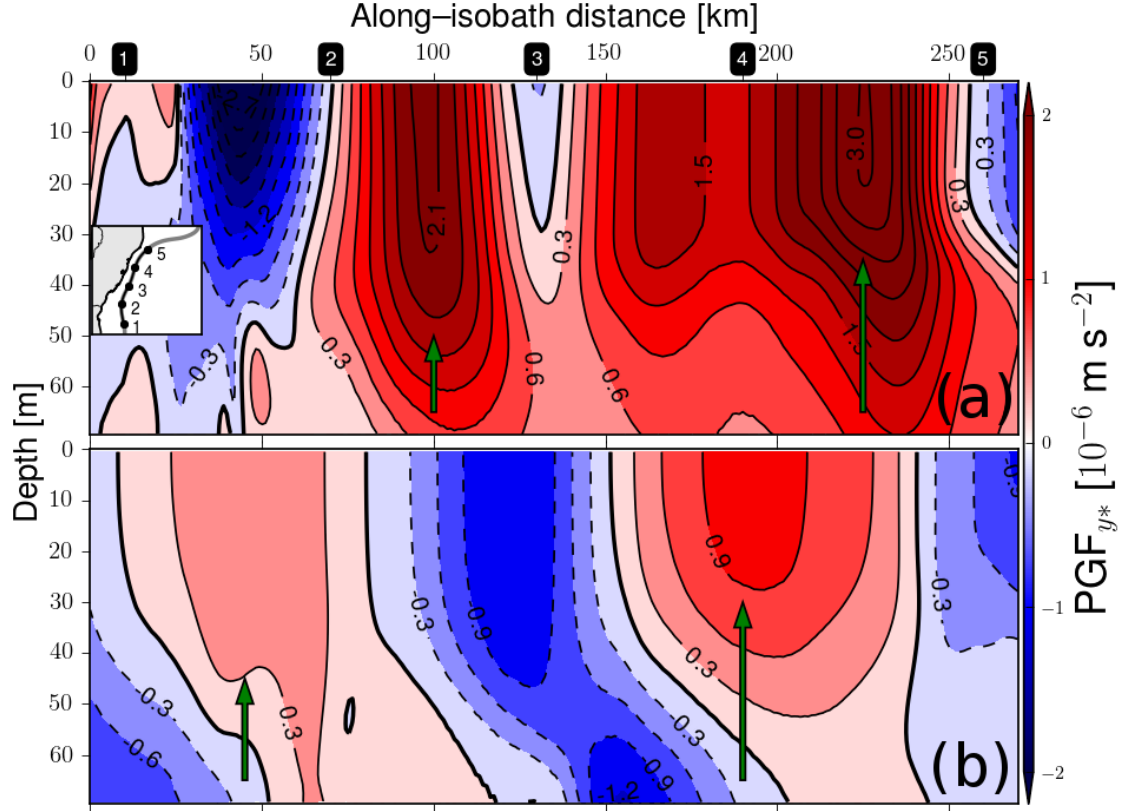


Figure 2.10: Run-averaged along-isobath pressure gradient force (PGF_{y^*}) along the 70 m isobath for the smooth topography scenarios. (a): EXP-smoo-1 (wind-only). (b): EXP-smoo-2 (BC-only). The heavy black line is the zero contour. The green arrows indicate preferential pathways of onshore flow, as in Figure 2.8. The markers labelled 1–5 along the x-axis of the top panel indicate along-isobath locations, which correspond to the dots on the map insert.

nesq reference density $\rho_0 = 1025 \text{ kg m}^{-3}$) is:

$$0 = \underbrace{-\frac{\partial(UV)}{\partial x^*} - \frac{\partial(VV)}{\partial y^*}}_{-\overline{\text{NL}}_{y^*}} \underbrace{-fU}_{-\overline{\text{COR}}_{y^*}} \underbrace{-P_{y^*}}_{\overline{\text{PGF}}_{y^*}} \underbrace{+\frac{\tau^{sy^*}}{H}}_{\overline{\text{SSTR}}_{y^*}} \underbrace{-\frac{\tau^{by^*}}{H}}_{\overline{\text{BSTR}}_{y^*}} \quad (2.4)$$

where $(U, V) \equiv \frac{1}{H} \int_{-H}^{\eta} (u, v) dz$ are the depth-averaged velocity components in the cross-isobath and along-isobath directions, respectively, τ^{sy^*} (τ^{by^*}) is the surface (bottom) stress, H is the local depth and $\overline{\text{PGF}}_{y^*} \equiv \left(\frac{g}{H\rho_0} \int_{\eta}^{-H} \int_{\eta}^z \frac{\partial \rho}{\partial y^*} dz' dz - g \frac{\partial \eta}{\partial y^*} \right)$ is the depth-averaged total pressure gradient force per unit mass in the along-isobath direction.

Along-shelfbreak patterns

We now evaluate the terms in Equation 2.4 to determine what dynamics dominates the flow and the net cross-isobath transport along the shelf edge. Figure 2.13 shows that in areas of onshore flow the water column is approximately in

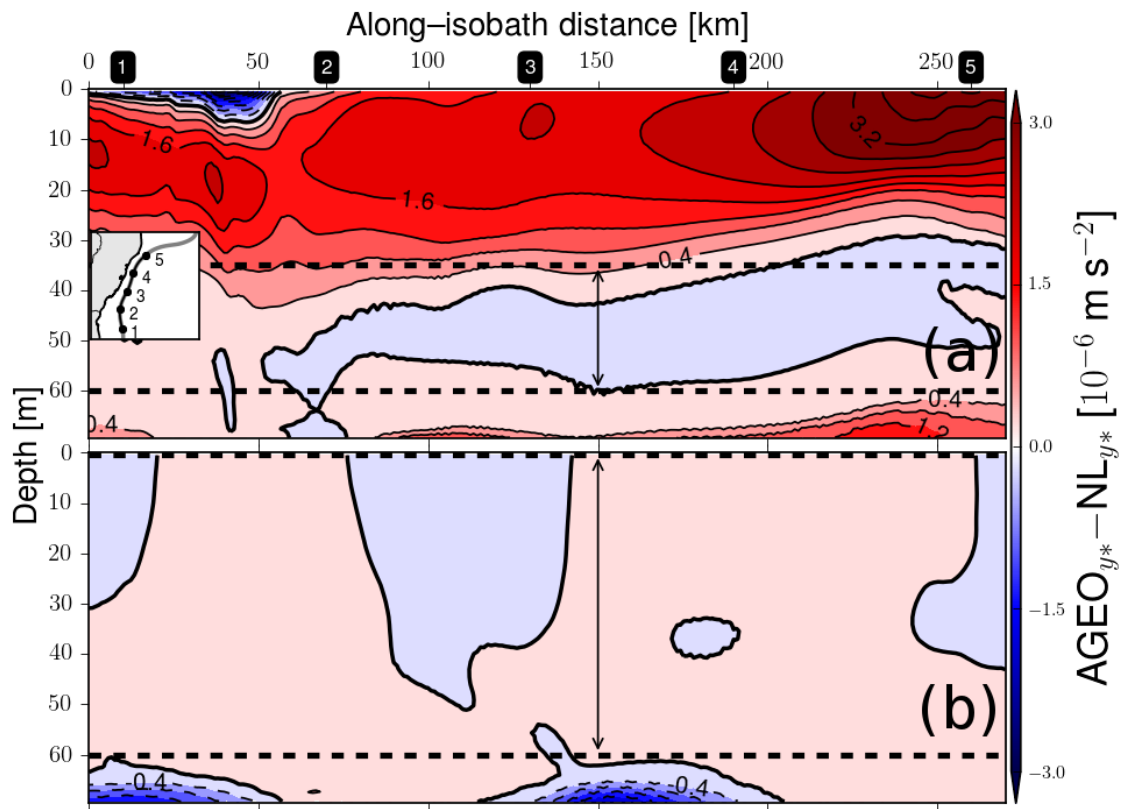


Figure 2.11: Run-averaged along-isobath residue between the along-isobath ageostrophic pressure gradient force (AGEO_{y^*}) and the net momentum advection term (NL_{y^*}). (a): EXP-smoo-1 (wind-only). (b): EXP-smoo-2 (BC-only). The heavy black line is the zero contour. The smallest residues are found away from the Ekman layers, within the nearly frictionless interior (areas indicated by the horizontal dashed lines). The markers labelled 1–5 along the x-axis of the top panel indicate along-isobath locations, which correspond to the dots on the map insert.

geostrophic balance in the along-isobath direction. Momentum advection is the next-largest term, and is particularly important in the north of the TB ($\approx 20.5^\circ\text{S}$ – 19.5°S) in EXP-smoo-1 (wind-only), as the depth-dependent momentum balance suggests (Figure 2.11a). In both EXP-smoo-1 and EXP-smoo-2 (BC-only) scenarios, bottom stress is the smallest of the terms considered. Part of the relative ineffectiveness of the bottom Ekman transport along the shelfbreak may be due to buoyancy arrest (see Section 2.4.1). The ratio τ^{by^*}/τ^{sy^*} in the wind-only experiment is 0.12 or smaller, indicating that, along the shelf edge, the offshore transport in the surface Ekman layer is at least 9–10 times larger than the onshore transport in the bottom Ekman layer. Inshore of the shelfbreak, the median (maximum) of this ratio at the location of maximum onshore flow is 0.37 (0.67), showing that the contribution of the bottom Ekman transport to the mass balance increases toward the coast. This range of τ^{by^*}/τ^{sy^*} values agrees with estimates derived from observations in different coastal upwelling systems (Lentz & Chap-

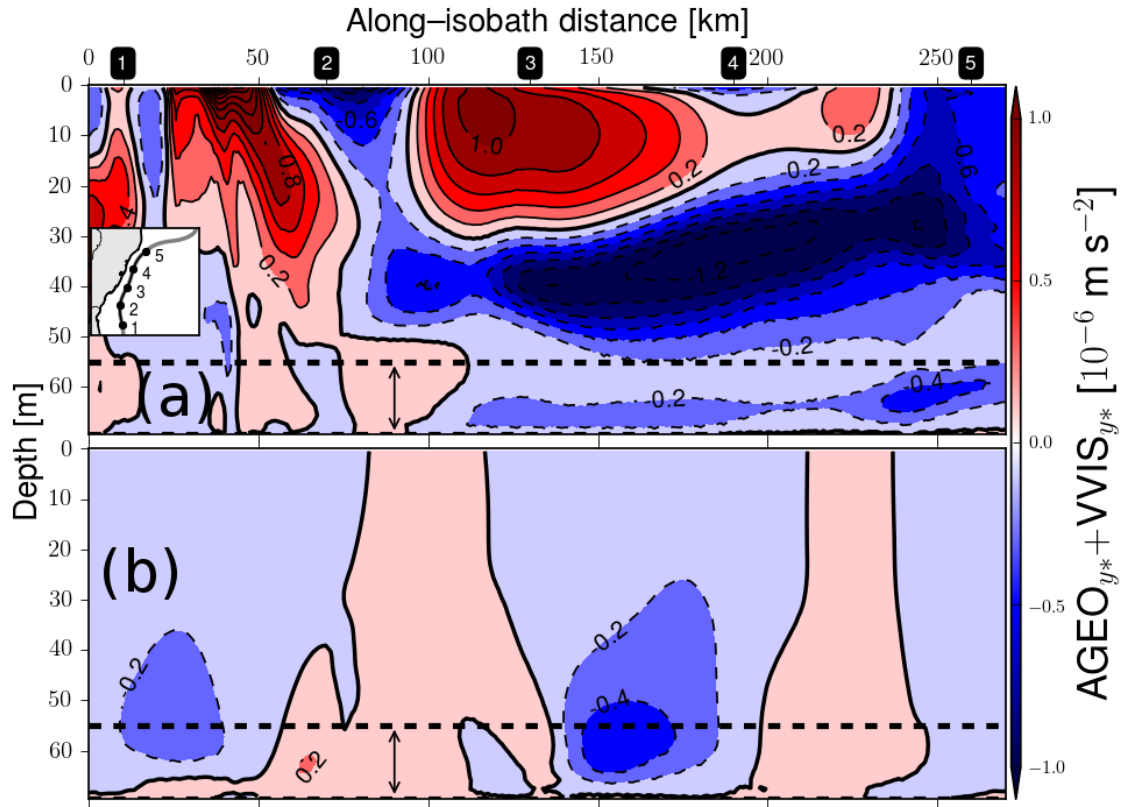


Figure 2.12: Run-averaged along-isobath residue between the along-isobath ageostrophic pressure gradient force ($AGEO_{y^*}$) and the vertical viscosity term ($VVIS_{y^*}$). **(a)**: EXP-smoo-1 (wind-only). **(b)**: EXP-smoo-2 (BC-only). The heavy black line is the zero contour. The smallest residues are found near the bottom, within the bottom Ekman layer (areas indicated by the horizontal dashed lines). The markers labelled 1–5 along the x -axis of the top panel indicate along-isobath locations, which correspond to the dots on the map insert.

man, 2004).

The depth-averaged balance in EXP-smoo-2 is mostly between the pressure gradient force, the Coriolis acceleration and the net momentum advection. In the wind-driven scenarios (EXP-smoo-1 and EXP-smoo-3) the wind stress is also important at leading order. Simplifying Equation 2.4 using this result, and multiplying it through by H/f yields

$$UH = \frac{\tau^{sy^*}}{f} - \frac{H}{f} P_{y^*} - \frac{H}{f} \overline{NL_{y^*}}. \quad (2.5)$$

This can be seen as a form of the parallel transport model (Csanady, 1982). The physical content of Equation 2.5 is that the net cross-isobath volume transport per unit length (in the along-isobath direction) is a balance between offshore surface Ekman transport and onshore geostrophic transport induced by the equatorward PGF_{y^*} throughout the water column (with a smaller contribution from momen-

tum advection), as shown in the previous section. This depth-averaged analysis confirms that the leading-order balance is geostrophic-like under the three forcing scenarios, especially in the BC-only case (EXP-smoo-2, Figure 2.13b). Moreover, the previous conjectures on the importance of the model nonlinear cross-isobath momentum advection (Lentz & Chapman, 2004) are also confirmed.

The realistic HYCOM solution reveals encouraging similarities with the simplified ROMS solutions. Specifically, the time-mean, depth-averaged flow across the shelfbreak is partly in geostrophic balance, and is onshore at the same preferential intrusion locations suggested by the results presented previously (blue shaded areas in Figure 2.14). In the areas where the $\overline{\text{PGF}_{y^*}}$ is equatorward (*i.e.*, preferential intrusion sites), its magnitude is $\approx 2-3 \times 10^{-6} \text{ m s}^{-2}$. This magnitude is comparable to the values obtained in the simplified experiments (Figure 2.13). The onshore velocities in the realistic experiment (simplified experiments) are typically $3-5 \text{ cm s}^{-1}$ ($1-4 \text{ cm s}^{-1}$).

The net transport across the TB shelf in the realistic experiment (EXP-smoo-3 experiment) is -0.13 Sv (-0.05 Sv). The difference is certainly in part due to the contribution of more energetic BC frontal eddies in the realistic experiment (see Arruda *et al.*, 2013 for details), since the BC sought in the simplified experiments is meant to represent a hypothetical state of the current with minimal eddy kinetic energy, *i.e.*, least mesoscale activity.

Horizontal patterns

After having examined the momentum budget along the shelf edge, a relevant question is: Is the equatorward PGF_{y^*} also the primary forcing of the model intrusions inshore of the shelfbreak? To answer this, we examine the spatial distribution of the PGF_{y^*} and the along-isobath Coriolis acceleration in the simplified experiments.

The onshore depth-averaged flow extends over large areas of the shelf in both EXP-smoo-1 (wind-only) and EXP-smoo-2 (BC-only) cases (Figure 2.15). These areas are consistent with the preferential intrusion sites discussed previously. The

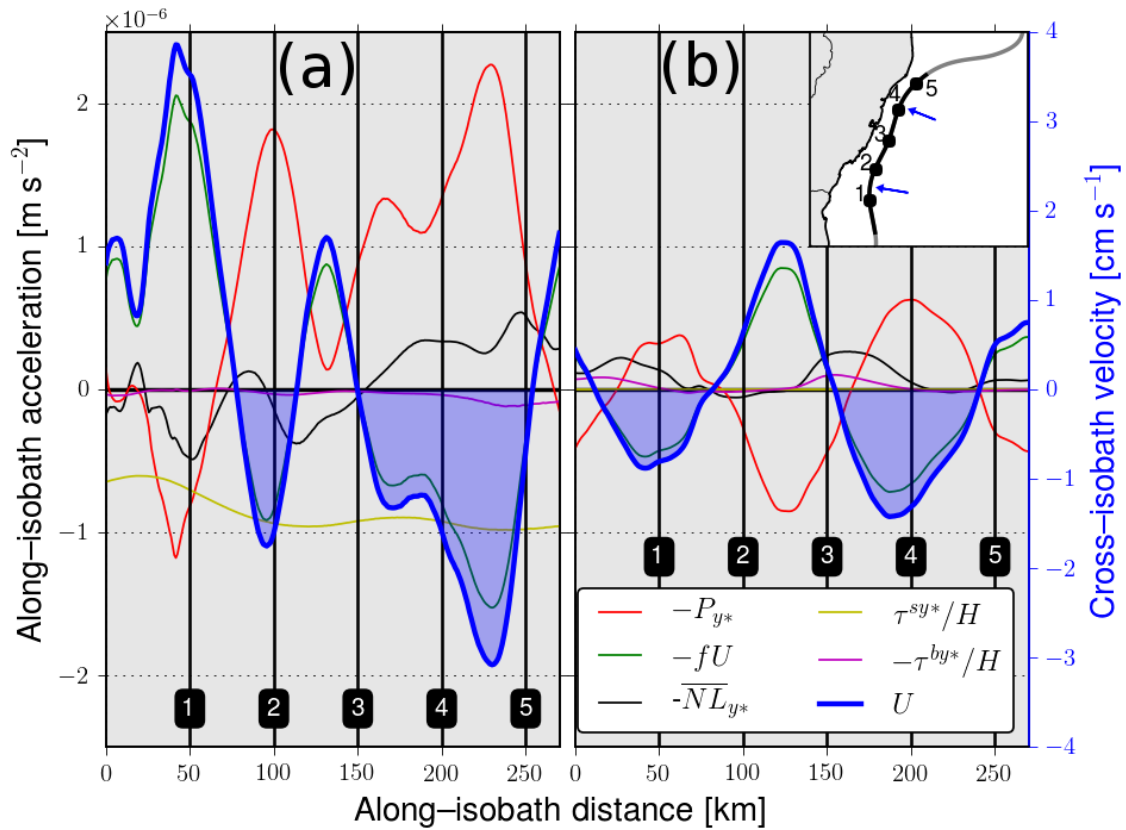


Figure 2.13: Run-averaged and depth-averaged momentum balance terms in the along-isobath direction along the 70 m isobath. (a): EXP-smoo-1 (wind-only). (b): EXP-smoo-2 (BC-only). The blue shading marks areas of onshore flow ($U < 0$), which are indicated by the blue arrows on the map insert. The vertical lines labelled 1–5 indicate along-isobath locations, which correspond to the numbered dots on the map insert.

equatorward PGF_{y^*} is partly balanced by the Coriolis acceleration, producing an onshore geostrophic flow. We also point out that the areas of onshore flow are roughly the same in both scenarios, once again suggesting that the effects of both forcings favor the SACW intrusions (Figure 2.15b,d), underneath the surface Ekman layer. The normalized root mean square difference between EXP-smoo-3 (wind+BC) and the sum of EXP-smoo-1 and EXP-smoo-2 is 2.7 % and 4.8 % for the $-P_{y^*}$ and $-fU$ fields, respectively.

Other studies have shown that preferential locations for offshore water intrusions and coastal upwelling may be associated with the combined effects of a western boundary current, upwelling-favorable winds and shelf geometry. Specifically, *Palma & Matano (2009)* show that a large area of geostrophically-balanced equatorward PGF_{y^*} forms in their numerical experiments in the South Brazil Bight area (22°S–28.5°S), producing onshore flow. At the south end of this region, *Campos et al. (2013)* show that the combination of intermittent upwelling-

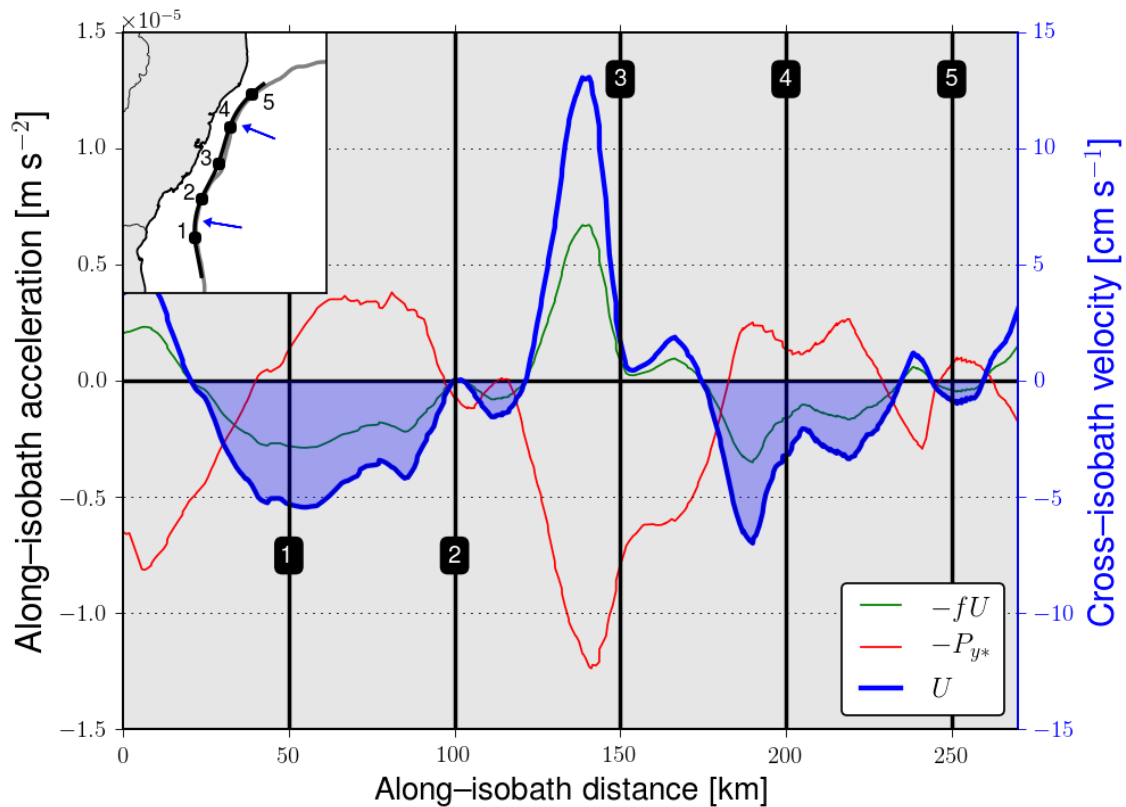


Figure 2.14: Time-averaged (2004–2009) and depth-averaged distributions of along-isobath pressure gradient force per unit mass ($-P_{y^*}$), Coriolis acceleration ($-fU$) and cross-isobath velocity (U) along the 70 m isobath for the realistic experiment. The blue shading marks areas of onshore flow ($U < 0$), which are indicated by the blue arrows in the map insert. The vertical lines labelled 1–5 indicate along-isobath locations, which correspond to the numbered dots on the map insert.

favorable winds and the BC-related PGF_{y^*} is a plausible explanation for the observed prevalence of coastal upwelling off a particular location around Cape Santa Marta (28.5°S). In addition, the cape geometry also has an important local effect in producing vertical transport through flow–topography interaction mechanisms (Mazzini & Barth, 2013). The ESB area also features dramatic along-shelf changes in shelf geometry and coastline orientation, which have been shown to be important on a smaller scale by Mazzini & Barth (2013). The present study suggests conclusions consistent with this perspective, as both the wind and the BC forcings add up to produce onshore motion at the preferential locations indicated by the blue arrows in Figure 2.15.

One of the effects related to along-shelf geometric changes is that onshore transport is expected to be enhanced in regions where the shelf narrows in the direction that long Coastal Trapped Waves (CTWs) propagate (Pringle, 2002). The downwave direction in the present case is equatorward, and therefore it could be

asked whether the sharp change in shelf width at $\approx 22^\circ\text{S}$ has any effect on the pressure (and flow) field at the north end of the ESB ($\approx 19.5^\circ\text{S}$). As shown by [Pringle \(2002\)](#), the scale of influence L_{fric} of a geometric perturbation in the downwave direction (in the barotropic and linear limits) is predicted to be $L_{\text{fric}} = (fH^2)/(\alpha r)$, where H is the local depth and f , α and r are typical absolute values for the Coriolis parameter, bottom slope and a linear bottom friction coefficient. Plugging in representative values⁶ for the TB yields $L_{\text{fric}} = 360$ km at the 70 m isobath. This is longer than the along-shelf extension of the TB ([Figure 2.1](#)). Therefore, we argue that this effect could remotely set up part of the PGF_{y^*} found in the wind-driven experiments, and therefore enhance SACW intrusions within the TB.

2.6 Deep-ocean forcing mechanisms

In this section, we attempt to isolate some of the deep-ocean physical processes involved in the SACW intrusions. We begin by quantifying the change in the upwelling source water caused by the thermal wind signal of the BC. Next, we investigate the shelf encroaching of the BC by inertial overshooting. Finally, we examine the along-shelf pressure gradient associated with the planetary β -effect with a simple analytical model.

2.6.1 Pycnocline uplifting linked to the Brazil Current mean jet

Perhaps the simplest mechanism through which a boundary current can influence coastal and shelfbreak upwelling is by changing the properties of the water available at the shelf edge. This is just a consequence of the fact that the current is in thermal wind balance, and therefore the pycnocline has to be either deeper or shallower (as in the present case) relative to its depth in the Sverdrup interior.

We quantified the change in the upwelling source water induced by the BC uplifting by comparing the minimum SST histories on the TB shelf in the simplified model experiments. [Figure 2.16a](#) shows that both wind-driven scenarios

⁶ $f = 5.1 \times 10^{-5} \text{ s}^{-1}$, $\alpha = 2.3 \times 10^{-3}$ and $r = 3.0 \times 10^{-4} \text{ m s}^{-1}$.

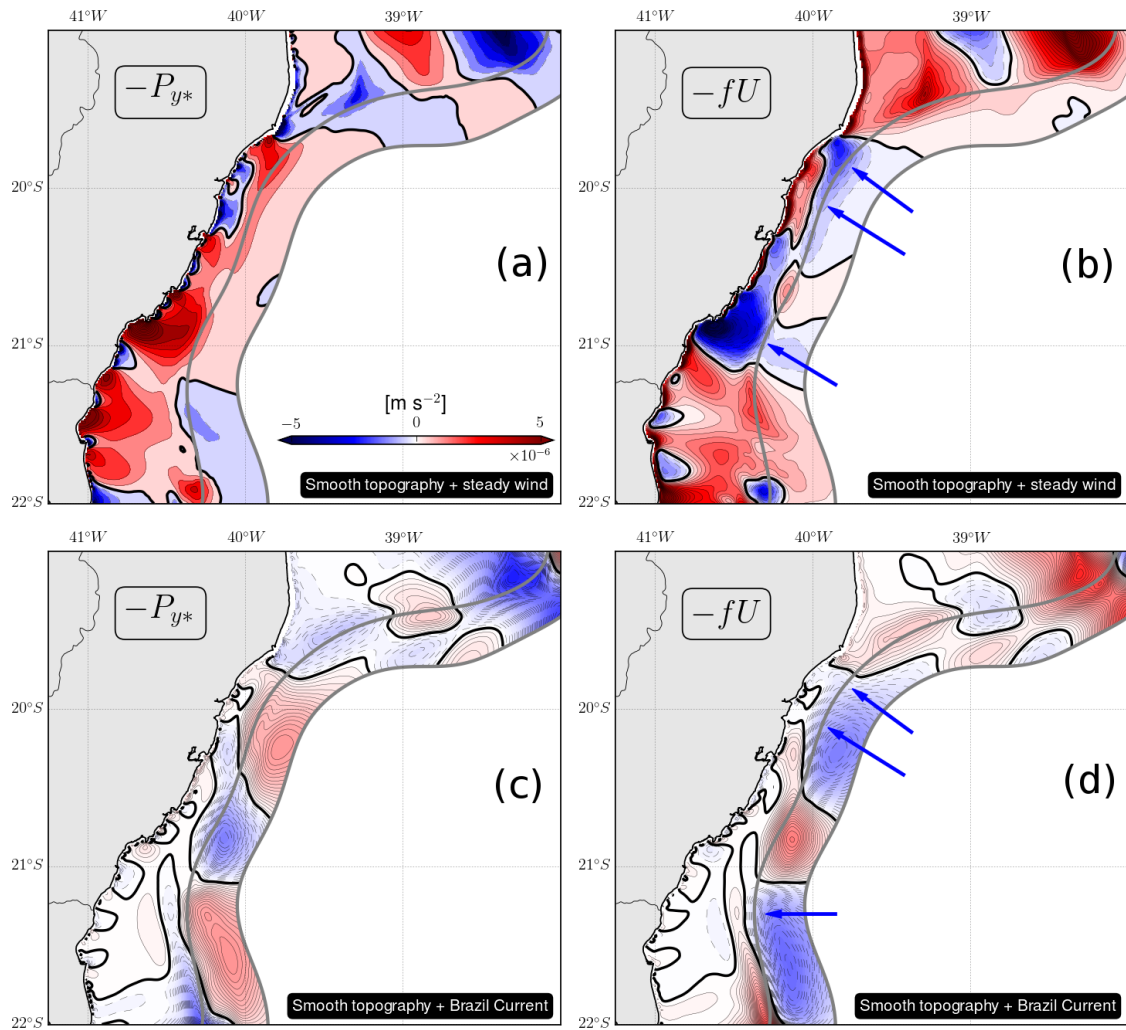


Figure 2.15: Horizontal distribution of run-averaged and depth-averaged along-isobath pressure gradient force per unit mass ($-P_{y*}$, **a,c**) and Coriolis acceleration ($-fU$, **b,d**) for the smooth topography scenarios. (**a,b**): EXP-smoo-1 (wind-only). (**c,d**): EXP-smoo-2 (BC-only). The thick gray lines represent the 70 m and 1000 m isobaths. The color scale is the same for all panels and the heavy black line is the zero contour. The blue arrows on the right column indicate preferential pathways of onshore flow.

undergo a spinup phase and attain a quasi-steady minimum shelf SST. In EXP-smoo-3 (wind+BC), however, the minimum SST is ≈ 1.4 °C colder than in EXP-smoo-1 (wind-only). As wind forcing has been shown to dominate the flow on the entire model shelf, we argue that the change in SST is mostly a consequence of the uplifting of colder isotherms due to the presence of the BC along the shelf edge.

Figure 2.16b shows the evolution of the intruded water volume on the TB shelf for the simplified experiments. This was measured by calculating the total volume instantaneously occupied by offshore water within a control volume of 1245

km^3 in the TB shelf⁷. Surprisingly, the mean onshore transport in EXP–smoo–3 is 0.10 Sv , 30 % smaller than in EXP–smoo–1. Consequently, the mean flushing time τ is also shorter in EXP–smoo–1 (97 days). In the wind–driven experiments with realistic topography τ is $\approx 50\text{--}60$ days (not shown).

It can be seen that intruded water (mostly SACW) eventually occupies $\approx 25\%$ of the TB shelf volume, considering a typical volume of 300 km^3 of intruded water on the shelf (Figure 2.16b). South of the ESB, in the northern South Brazil Bight, SACW has been estimated to occupy a larger fraction of the total shelf volume (37–56 %, *Cerda & Castro, 2014*).

We conclude from the present analyses that the amount of intruded water in EXP–smoo–3 (wind+BC) is slightly smaller than in EXP–smoo–1 (wind–only), but the minimum SST on the shelf is colder. In other words, total mass exchange is slightly smaller when the BC is present, but the additional uplift of the thermocline causes the upwelling source water to be colder.

2.6.2 Shelf encroaching of the Brazil Current by inertial overshooting

When flow in exact geostrophic balance encounters a change in bottom topography, its ability to continue to follow isobaths depends on its amount of inertia. As it flows along the ESB shelfbreak, the BC is expected to locally overshoot it in some areas, thereby advecting SACW and TW onto the outer part of the continental shelf.

This effect is expected to be more important where the curvature R^{-1} of the isobaths is large enough to cause the centrifugal acceleration V^2/R experienced by a water parcel moving with an along–isobath velocity V to become comparable to the Coriolis acceleration fV . The ratio

$$Ro_{\text{curv}} = \frac{V}{fR} \quad (2.6)$$

⁷See Section 2.4.2 for an explanation on the initialization and interpretation of the passive tracer (dye) fields in the simplified experiments.

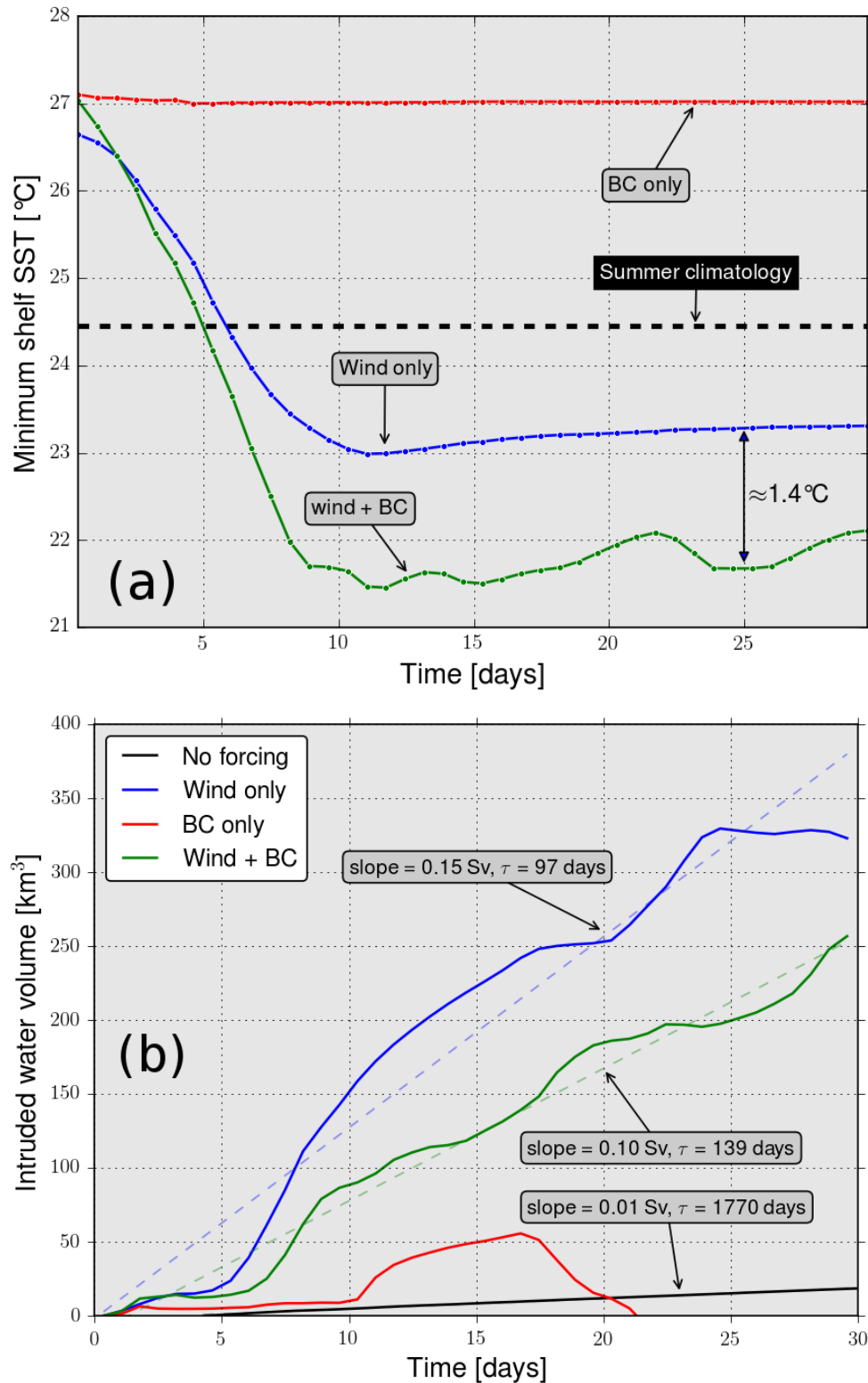


Figure 2.16: Model histories showing the effect of pycnocline uplifting by the BC. **(a)**: Comparison of the model minimum shelf SST histories (on the TB area) for EXP-smoo-1 (wind-only), EXP-smoo-2 (BC-only) and EXP-smoo-3 (wind+BC) experiments. The black dashed line indicates the observed climatological minimum SST (see Figure 2.5a). **(b)**: Comparison of the model shelf-averaged intruded dye volume histories (on the TB area) for the same experiments. The dashed lines are linear least-squares fits, and their slopes represent the mean onshore transport of slope water onto the shelf under each forcing scenario. τ indicates the mean flushing time of the shelf control volume, based on the slope of the linear fits. The negligible signal of the unforced scenario (solid black line) is a model sensitivity test, whose flow field is exclusively due to numerical horizontal pressure gradient errors.

can therefore be defined to measure the importance of the contribution of curvature effects. [Figure 2.17](#) shows Ro_{curv} along the 100 m isobath in EXP-smoo-2 as a function of latitude. The mean (maximum) value of Ro_{curv} is 0.02 (0.18), and the local maxima coincide with the areas of maximum isobath curvature. Away from the maxima, Ro_{curv} is everywhere smaller than 0.05. The smallness of Ro_{curv} reflects the relatively weak mean along-isobath flow represented by EXP-smoo-2, which is everywhere slower than 26 cm s^{-1} . If a typical synoptic along-isobath velocity of 0.6 m s^{-1} is considered instead (as observed during the OCT12 survey, [Figure 2.18a,c](#)), the mean (maximum) Ro_{curv} increases to 0.11 (0.51). Curvature effects are therefore more relevant in the south and north ends of the TB, especially when the incoming BC jet is most energetic.

Areas of high relative vorticity ζ clearly exist along the TB shelf edge, and a convenient measure of the relative importance of the total (curvature + shear) nonlinear effects is given by the quantity $Ro = |\zeta/f|$ ([Figure 2.18](#)). It is seen that both the time-mean realistic model fields and direct velocity observations indicate typical (maximum) values of Ro of ≈ 0.3 (≈ 0.5), spreading over large areas of the TB slope and shelf edge. Therefore it seems that it is horizontal shear (rather than the more localized and episodic curvature effects) that account for the bulk of the nonlinearities at the shelf edge in a time-mean sense.

The Kuroshio is perhaps one of the best documented examples of the inertial overshooting process (*e.g.*, [Hsueh et al., 1996](#); [Vélez-Belchí et al., 2013](#)), with $Ro \approx 0.5$ ([Brink, 1998](#)). The size of Ro estimated in the present analyses therefore predicts shelf encroaching to be locally important along the shelf edge of the TB.

Off southeast Australia, encroaching of the East Australian Current (EAC) has been shown to occasionally precondition the water mass field on the shelf with colder offshore water, which may in turn reach the coast under the influence of persistent upwelling-favorable winds. This interaction has been shown to cause more intense coastal upwelling events than the ones observed without encroaching or other favorable EAC-related processes (*e.g.*, [Gibbs et al., 1998](#); [Roughan & Middleton, 2002](#); [Schaeffer et al., 2013](#)). Events when the BC is more energetic are

thus probably associated with stronger shelf encroaching, and therefore more significant preconditioning of the shelf water mass structure to wind-driven upwelling.

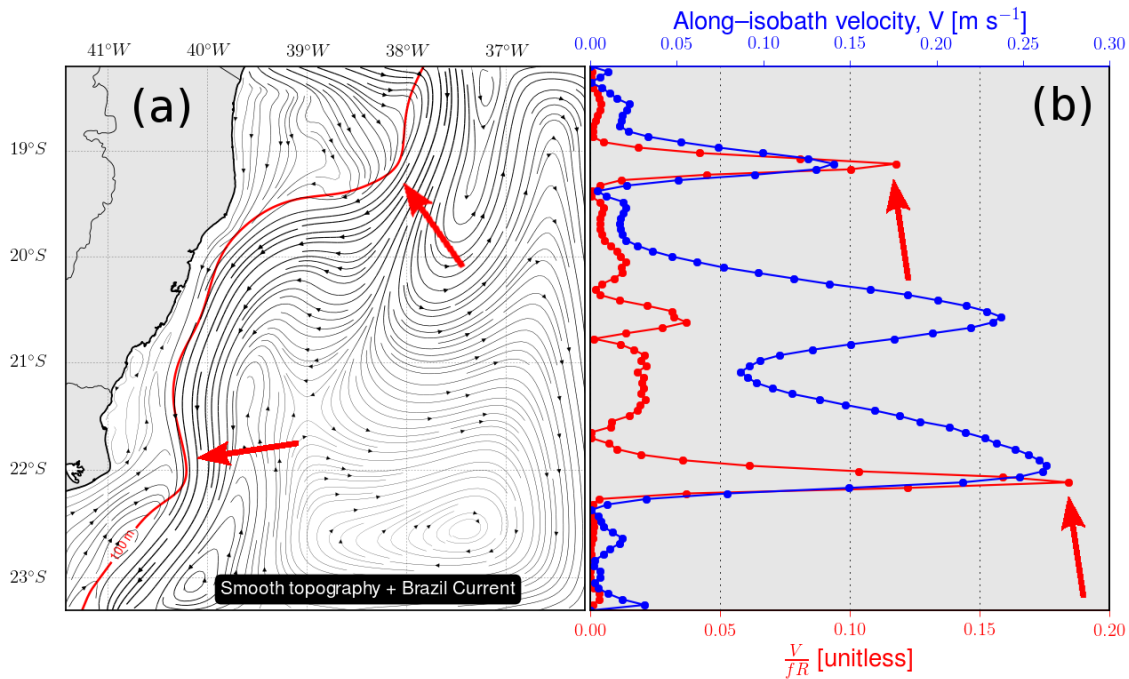


Figure 2.17: Distributions of model velocity (run-averaged and depth-averaged in the upper 100 m) and centrifugal acceleration normalized by the Coriolis acceleration, $Ro_{\text{curv}} = V/(fR)$. (a): Streamlines for simplified experiment EXP-smoo-2 (BC-only). The red line is the 100 m isobath, used to perform the Ro_{curv} calculations. (b): Associated along-isobath velocity (blue) and curvature Rossby number Ro_{curv} as functions of latitude. The red arrows indicate areas of large curvature effects, which are found mostly where the along-isobath flow encounters sharp changes in isobath orientation.

2.6.3 Meridional pressure gradient induced by the β effect

Although safely neglected in models of coastal circulation where the f -plane approximation is valid, the planetary β -effect is perhaps an overlooked mechanism in the context of shelfbreak upwelling. In the following we examine the meridional (*i.e.*, along-shelf) pressure gradient force PGF_y^β induced by the planetary β -effect. We employ a single-layer reduced gravity model⁸ as in [Charney \(1955\)](#). The dynamically active (upper) layer ([Figure 2.19](#)) is assumed to be in geostrophic balance, *i.e.*,

$$-fv = -g'h_x, \quad (2.7)$$

⁸Also referred to in the literature as a 1.5-layer equivalent-barotropic model.

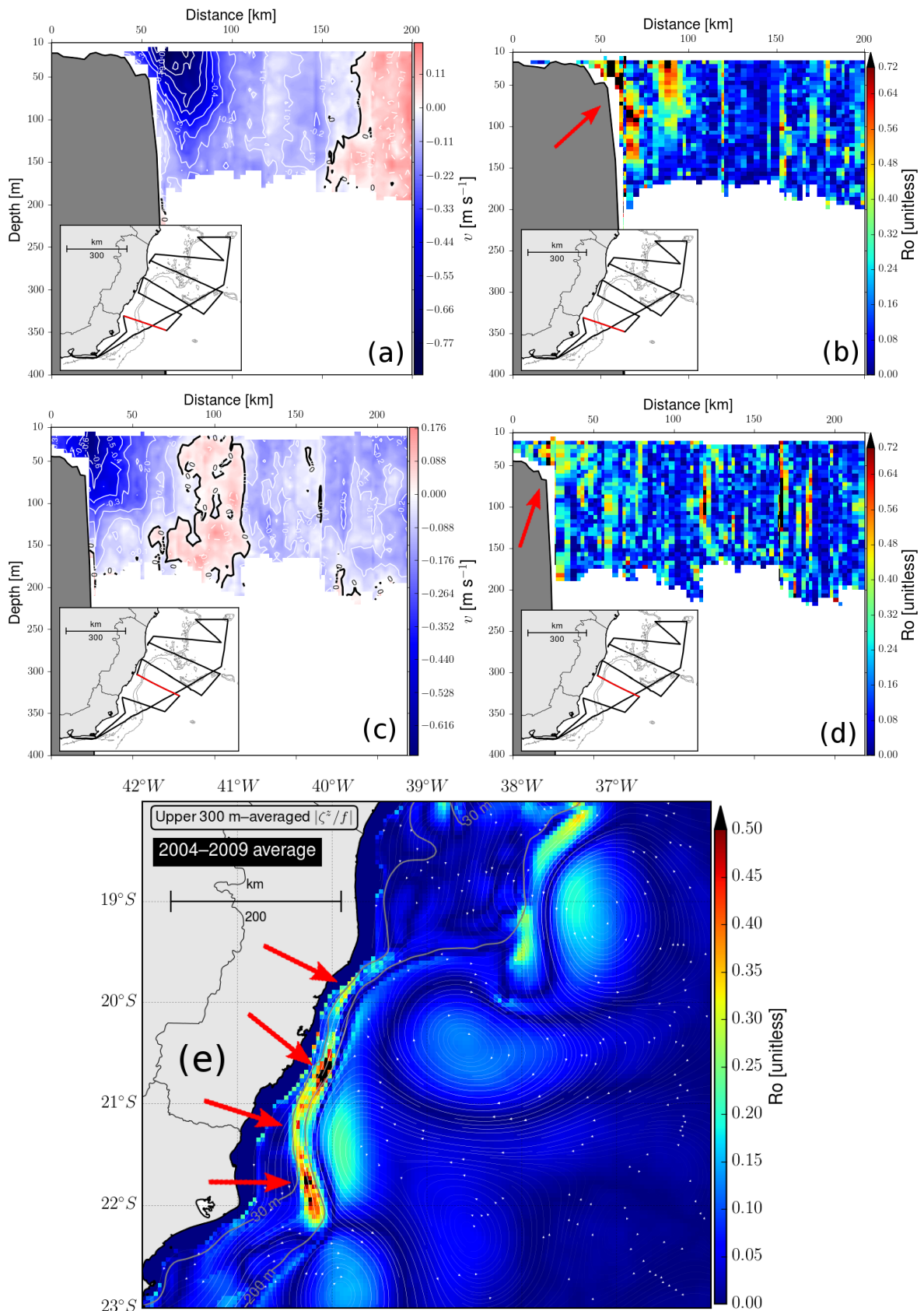


Figure 2.18: Distributions of model velocity and relative vorticity normalized by the local inertial frequency, $Ro = |\zeta/f|$, demonstrating the proneness of shelf edge locations to the effect of shelf encroaching of the BC. (a,b,c,d): Examples of observation-derived cross-transect velocity (a,c) and Ro (b,d) along two transects occupied in the OCT12 survey. The red lines on the map inserts indicate the location of the transects. (e): 2004–2009 average of depth-averaged (within the upper 300 m) velocity (white streamlines) and Ro (color shading) from the realistic HYCOM simulation. The gray lines are the 30 m and 200 m isobaths. The arrows indicate areas of large relative vorticity, located mostly around the shelf edge, following the inshore lobe of the BC jet.

where f is the Coriolis parameter, v is the along-shelf velocity, h is the upper layer thickness and $g' \equiv g(\rho_2 - \rho_1)/\rho_2$ is a reduced gravity based on the total acceleration due to gravity g and the densities of the upper (ρ_1) and lower (ρ_2) layers. The subscript x indicates partial differentiation in the cross-shelf direction. Multiplying [Equation 2.7](#) by h and integrating from the shelf edge ($x = x_c$) to the offshore limit of the western boundary layer ($x = x_o$) gives

$$\int_{x_c}^{x_o} hv \, dx = \frac{g'}{f} \int_{x_c}^{x_o} h_x h \, dx. \quad (2.8)$$

The left-hand side of [Equation 2.8](#) is the total along-shelf volume transport Q in the upper layer. Manipulating the right-hand side using the product rule yields

$$Q = \frac{g'}{f} \int_{x_c}^{x_o} (h^2/2)_x \, dx, \quad (2.9)$$

or, in terms of the thermocline depths at the outer limit of the BC (h_o) and at the shelf edge (h_c),

$$Q = \frac{g'}{2f} (h_o^2 - h_c^2). \quad (2.10)$$

[Equation 2.10](#) establishes a relationship between the along-shelf transport of the BC and how much it uplifts the thermocline in the cross-shelf direction. Solving [Equation 2.10](#) for h_c gives

$$h_c^2 = h_o^2 - \frac{2fQ}{g'}. \quad (2.11)$$

Let us now seek a crude estimate of the along-shelf pressure gradient force at the shelf edge (PGF_y^β) caused in response to this effect. We assume that the BC jet conserves mass ($Q = \text{constant}$) between two along-shelf locations $y_{\text{north}} = 19^\circ\text{S}$ and $y_{\text{south}} = 22^\circ\text{S}$, and that the offshore thermocline depth h_o does not vary between those locations. Plugging approximate values for Q , g' , h_o , f_{north} and f_{south} in [Equation 2.11](#) yields

$$(h_c)_{\text{north}} - (h_c)_{\text{south}} \approx -8 \, \text{m}, \quad (2.12)$$

that is, the thermocline is predicted to be ≈ 8 m shallower in the north end of the TB shelf, which is consistent with the existence of a northward PGF_y^β and an onshore geostrophic flow across the shelf edge. We may use Equation 2.12 to estimate the magnitude of this force:

$$\text{PGF}_y^\beta = -g' \left[\frac{(h_c)_{\text{north}} - (h_c)_{\text{south}}}{y_{\text{north}} - y_{\text{south}}} \right] = 5.6 \times 10^{-7} \text{ m s}^{-2}. \quad (2.13)$$

This acceleration is comparable to the total pressure gradient force per unit mass modeled in the BC-only scenario (Figure 2.13b). It drives an onshore depth-averaged geostrophic velocity PGF_y^β/f of $\approx -1 \text{ cm s}^{-1}$.

An evaluation of the accuracy of the estimate in Equation 2.12 and the assumption that h_o does not vary in the along-shelf direction is desirable. To achieve this, we examined the thermocline depth distribution derived from the annual WOA13 objectively-analyzed (OA) Temperature (T) and Salinity (S) fields. The result does show an ≈ 10 m shallower thermocline at 19.5°S relatively to 21°S (Figure 2.20a). We point out, however, that an accuracy estimate for this dataset is not straightforward in this case. This is because the objective analysis technique used to produce the WOA13 fields does not provide information on the spatial distribution of the variance of the interpolation error, unlike other objective analysis techniques commonly employed in the spatial mapping of oceanographic variables (e.g., *Bretherton et al., 1976*). In the WOA13 case, the standard error about the statistical mean and the difference between the OA fields and the statistical mean fields ($\text{OA} - \bar{X}$) are the natural measures of uncertainty. However, the analysis of the thermocline depth distribution derived from the statistical mean fields of T and S gives rise to another problem. The number of T and S observations per 0.25° square is so small in the ESB (Figure 2.20b) that the thermocline depth distribution derived from the statistical mean (and hence the $\text{OA} - \bar{X}$ map) is excessively patchy (not shown). Due to its statistical limitations, we consider the OA WOA13 fields only as a suggestive experimental verification of the PGF_y^β .

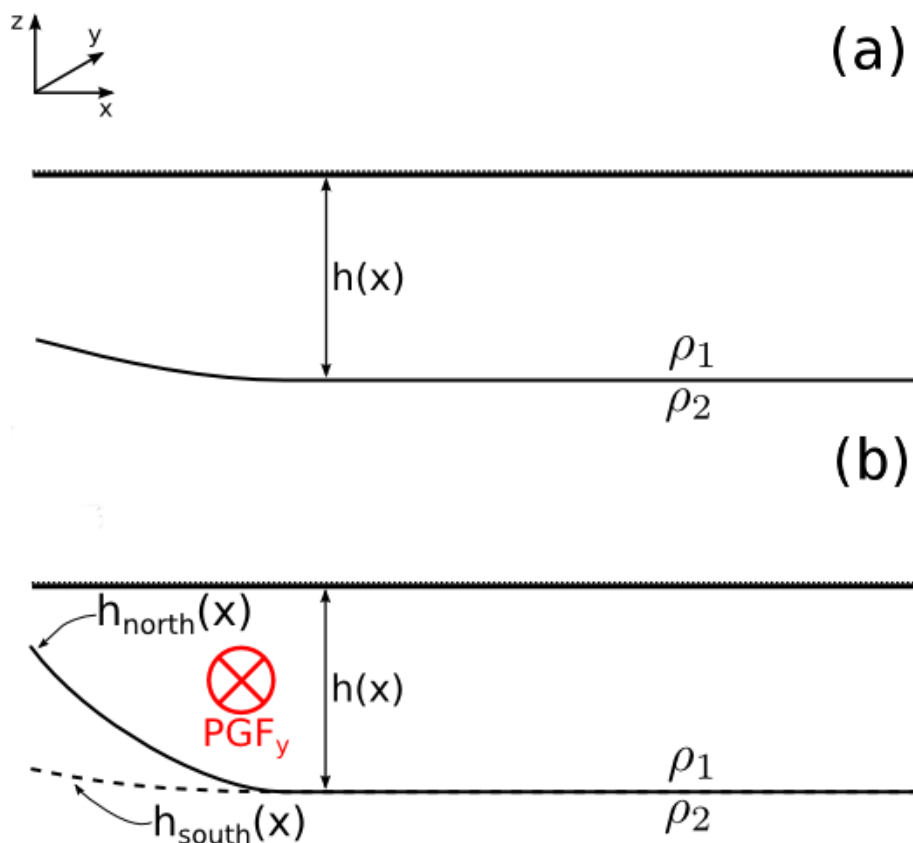


Figure 2.19: Schematic representation of a single-layer reduced gravity model for the BC. **(a)**: Geometry of the model, showing the cross-shelf (x), along-shelf (y) and vertical (z) coordinate axes, the variable thickness of the upper layer (h) and the densities of the upper (ρ_1) and lower (ρ_2) layers. **(b)**: Schematic representation of an equatorward along-shelf pressure gradient force (PGF_y) linked to an along-shelf gradient in the upper layer thickness induced by the planetary β -effect.

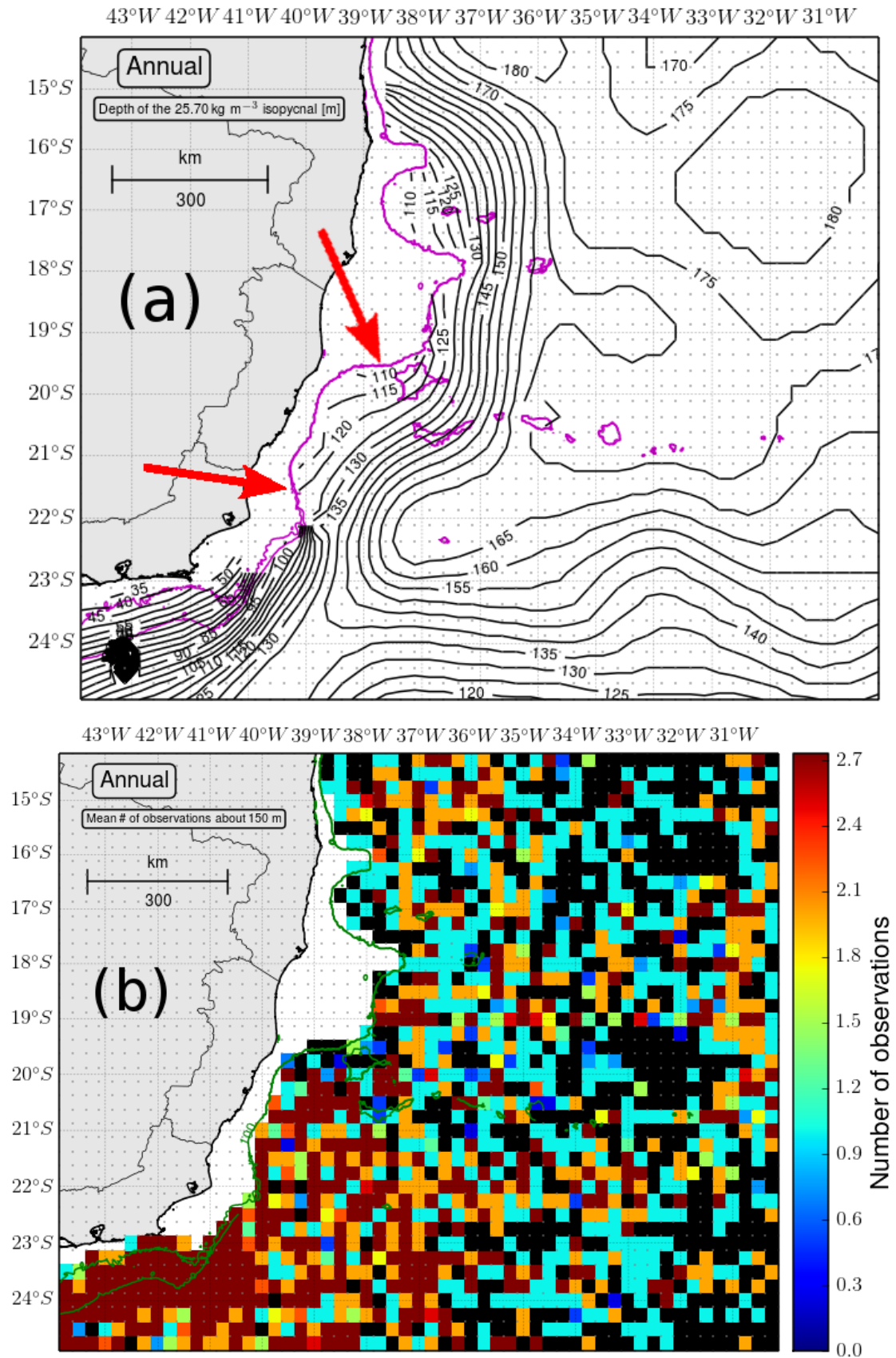


Figure 2.20: Climatological thermocline depth estimated from the WOA13 dataset. (a): Depth of the 1025.7 kg m⁻³ isopycnal (black contours), chosen as representative of the main thermocline. The red arrows indicate the hypothetical south and north ends of the reduced gravity model. The magenta contours are the 100 m and 200 m isobaths. (b): Horizontal map of number of observations at the depth of the 1025.7 kg m⁻³ isopycnal within each 0.25-degree square. Black means no data. The green contours are the 100 m and 200 m isobaths.

2.7 Summary and conclusions

The goal of the present study is to investigate the intrusion pathways and the associated physical mechanisms involved in the intrusions of South Atlantic Central Water (SACW) onto the Espírito Santo Basin (ESB) shelf, with emphasis on the Tubarão Bight (TB) area. We employ a combination of realistic and simplified numerical experiments and an analysis of available observations to examine the effects of bottom topography, wind-driving and the Brazil Current (BC). A schematic overview of our findings is presented in [Figure 2.21](#).

SACW appears to enter the model shelf through preferential pathways which coincide with along-shelf locations where a geostrophically-balanced equatorward (*i.e.*, intrusion-favorable) along-isobath pressure gradient force (PGF_{y^*}) exists, as consistently suggested by the simplified and realistic numerical experiments. The geostrophic balance in the along-isobath direction is modified by momentum advection at mid-depth and by friction in the bottom Ekman layer. Both wind- and BC-forced scenarios are found to produce an equatorward PGF_{y^*} . However, the BC-induced PGF_{y^*} is about half as intense as its wind-induced counterpart (which is $\approx 2 \times 10^{-6} \text{ m s}^{-2}$), and has a periodic along-shelf pattern, alternating areas of onshore and offshore geostrophic flow. The net effect is an equatorward PGF_{y^*} throughout most of the TB, with local maxima at the preferential intrusion sites.

Typical magnitudes of the model time-mean, depth-averaged onshore velocities are $1\text{--}5 \text{ cm s}^{-1}$. The dominance of the model onshore geostrophic flow extends beyond the shelf edge area, apparently contributing to the SACW transport also on the shelf proper. Estimates of the slope Burger number from the five available hydrographic datasets yield values between 0.32 and 0.92. The associated buoyancy arrest time scales suggest that the system might be more likely to experience buoyancy arrest during vigorous SACW intrusions. The vertical structure of the onshore velocity at the shelf edge is consistent with theoretical predictions for $S = O(1)$, suggesting the interpretation that the cross-isobath velocity structure in the TB is modulated by the intensity of the SACW intrusions.

Wind forcing alone is both required and sufficient to reproduce the main features of coastal upwelling in the TB. Among the next-order effects, the uplifting of the thermocline by the BC results in the outcropping of water $\approx 1.4^\circ\text{C}$ colder under steady, upwelling-favorable wind forcing (compared to a flat stratification, BC-free scenario). The BC also affects the SACW intrusions by inertially overshooting the shelf edge, consistent with what is expected for the estimated Rossby numbers of ≈ 0.3 – 0.5 along the shelf edge. Finally, the planetary β -effect is also found to account for a background equatorward PGF_{y^*} .

It was not our intention to accurately represent the coastal and deep-ocean circulation of the ESB, nor to develop a detailed understanding of all the physical processes involved in the problem. Therefore, many open questions remain. Future work should be aimed at the effects on SACW intrusions of coastal trapped waves, internal waves, and the energetic mesoscale eddy field associated with the BC, among other processes. From an observational viewpoint, additional and better-resolved quasi-synoptic and moored observations on the middle shelf and shelf edge areas would allow for experimental testing of the model predictions discussed in the present study.

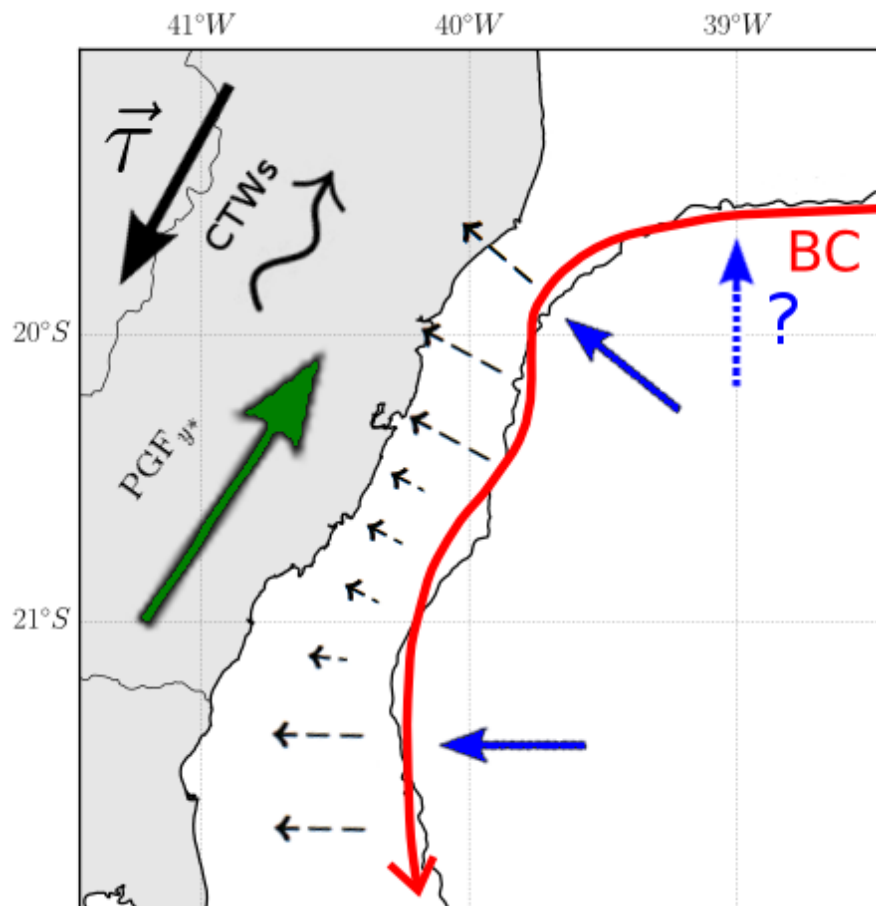


Figure 2.21: Schematic representation of the proposed South Atlantic Central Water (SACW) intrusion pathways and physical mechanisms in the Espírito Santo Basin (ESB). The solid black arrow indicates the direction of prevailing wind and shelf mean flow. The wiggly arrow indicates the direction of propagation of long Coastal Trapped Waves (CTWs). The thick red line indicates the BC flow along the shelf edge and areas of local inertial overshooting. The blue arrows indicate preferential pathways for SACW intrusions. The dashed blue arrow indicates the possible pathway along the southern flank or the AB. The long (short) dashed black arrows over the shelf indicate areas of stronger (weaker) onshore flow. The green arrow indicates the direction of the total time-mean along-isobath pressure gradient force (PGF_{y^*}) on the shelf.

Chapter 3

Steady cross–shelf circulation

induced by a periodic slope current:

Analytical and numerical solutions

for the Tubarão Bight (Southeast

Brazil)

Abstract

The steady response of the continental shelf to a periodic (in the along–shelf direction) pressure forcing at the shelf edge is compared with primitive–equation numerical solutions for a narrow shelf in the Tubarão Bight (TB, 19.5°S–22°S, Southeast Brazil). The Brazil Current (BC) flows along the TB shelf edge, transporting cold South Atlantic Central Water and imparting a pressure gradient that was found to extend throughout the shelf in the numerical solutions discussed in [Chapter 2](#). In this study, a simple Arrested Topographic Wave (ATW) analytical model is found to be successful in representing the general qualitative and quantitative features of these numerical solutions. The cross–shelf e –folding scales of the cross–shelf velocity estimated from the numerical solutions agree in order of magnitude with the cross–shelf penetration scale $q^{-1} = \sqrt{-2r/(lfs)} = 10$ km predicted by the ATW, where r is a linear bottom resistance parameter, l is the along–shelf wavenumber of the forcing at the shelf edge, f is the Coriolis parameter and s is the bottom slope. The numerical e –folding scales decrease with increasing forcing amplitude, and are found to be partially within the predicted range for q^{-1} , especially for stronger ($> 60 \text{ cm s}^{-1}$) BC core velocities. Furthermore, the use of quadratic bottom stress accounts for some of the relative

increase in the numerical onshore penetration scales, which are predicted to be $q_{\text{quadratic}}^{-1} = \sqrt{-2C_D/(lfs)} \times \sqrt{U_{\text{bot}}}$, where C_D is a quadratic bottom friction parameter and U_{bot} is the near-bottom velocity magnitude. The kind of steady response to periodic deep-ocean forcing examined here may provide insight into other continental shelves under the influence of western boundary currents or other deep-ocean pressure gradients.

Keywords: *Arrested Topographic Wave, deep-ocean forcing, coastal dynamics, cross-shelf transport, Brazil Current.*

3.1 Introduction

Much understanding on the time-mean circulation of the coastal ocean has been gained with the classic Arrested Topographic Wave (ATW) model (*Csanady, 1978*). The simplest forms of this model describe the steady-state response of the coastal ocean to pressure perturbations imparted by wind, river runoff or deep-ocean pressure gradients. The effects of the coastal boundary, friction and rotation combine to diffuse the pressure perturbations throughout the shelf and produce along-shelf pressure gradients that are in partial geostrophic balance, giving rise to cross-shelf transport.

Different versions of the ATW model have been used to rationalize observations and primitive-equation model results. *Schlichtholz (2002)* showed that a modified version of the ATW is consistent with hydrographic observations and inverse solutions of the near-bottom flow in Fram Strait. *Miller et al. (2011)* derived a matched shelf-slope ATW model to rationalize primitive-equation numerical results obtained by *Matano & Palma (2008)* in the context of shelfbreak upwelling in the Patagonian shelf. *Miller et al. (2011)* showed that quantitative agreement was found between the nonlinear, stratified primitive-equation solutions and the much simpler linear, homogeneous ATW solution in their case.

In [Chapter 2](#), process-oriented numerical experiments were analyzed to investigate the effects of forcing mechanisms related to the Brazil Current (BC) on intrusions of cold, nutrient-rich South Atlantic Central Water (SACW) on the continental shelf of the Tubarão Bight (TB) area (19.5°S–22°S), off southeast Brazil. With the neglect of wind forcing, the bulk of the onshore transport of SACW was

related to a geostrophically–balanced pressure gradient force in the along–isobath direction, but the actual mechanisms behind the generation of this force were unclear. In the present study, an ATW model forced by a sinusoidal pressure field at the shelf edge is used to rationalize some features of the numerical solutions discussed in [Chapter 2](#). The modified ATW solution is derived in [Section 3.2](#) and compared to the numerical solutions in [Section 3.3](#). Conclusions are presented in [Section 3.4](#).

3.2 The analytical model

We consider the idealized domain of a continental shelf in the southern hemisphere that is infinite in the meridional direction, with a solid coastal boundary at $x = 0$. A steady western boundary current flows poleward along the shelf edge, which is placed at $x = L$. The current has a periodic structure with wavelength $2\pi/l$ in the along–shelf direction. No wind forcing is prescribed.

Under the long–wave (*e.g.*, [Gill & Schumann, 1974](#)) and f –plane approximations, the depth–averaged equations of motion in the steady, linear and barotropic limits are (*e.g.*, [Csanady, 1978](#)):

$$-fv = -\frac{1}{\rho}p_x \quad (3.1a)$$

$$fu = -\frac{1}{\rho}p_y - \frac{rv}{h} \quad (3.1b)$$

$$(uh)_x + (vh)_y = 0, \quad (3.1c)$$

where p is the depth–averaged pressure, u and v are the cross– and along–shelf depth–averaged velocities, f is the Coriolis parameter, $\rho = 1025 \text{ kg m}^{-3}$ is density, r is a linear bottom resistance coefficient and h is depth. A linear cross–shelf depth profile of the form $h = h_0 + sx$ is chosen, with $h_0 = 0 \text{ m}$ and $s > 0$. Subscripts with respect to the independent variables (x,y) indicate partial differentiation.

Equations [3.1a–c](#) may be combined into a single parabolic partial differential

equation for pressure, *i.e.*,

$$p_{xx} + \frac{fs}{r}p_y = 0. \quad (3.2)$$

As pointed out by [Csanady \(1978\)](#), [Equation 3.2](#) is analogous to the one-dimensional heat equation. In this analogy, p is like temperature, the y direction is like time, and the quantity $r/(fs)$ is like thermal conductivity but has units of length. As wind forcing is not included here, the boundary condition of no cross-shelf flow at the coast ($uh = 0$ at $x = 0$) that follows from [Equations 3.1a](#) and [3.1b](#) is

$$p_x = 0. \quad (3.3)$$

The boundary condition at the shelf edge ($x = L$) is chosen to approximate the sinusoidal shape of the pressure field obtained in the numerical solutions ([Figure 3.1](#)):

$$p = a \sin (ly), \quad (3.4)$$

where a and l are the amplitude and along-shelf wavenumber of the pressure field, respectively.

The boundary condition in the y direction is more elaborate. It is analogous to the initial condition of the heat equation, which represents the initial temperature distribution along a one-dimensional iron slab. In the present problem, it represents the cross-shelf shape of the pressure field at a known along-shelf position. The rationale for neglecting this boundary condition is that we do not aim to study the along-shelf spreading of an arbitrary cross-shelf pressure perturbation like $p(x, 0) = \varphi(x)$. Rather, we are concerned with the onshore penetration of a prescribed sinusoidal pressure field at the shelf edge. Defining $k \equiv -r/(fs)$, the problem becomes

$$p_y = kp_{xx} \quad (3.5a)$$

$$p_x(0, y) = 0 \quad (3.5b)$$

$$p(L, y) = a \sin (ly) \quad (3.5c)$$

in the domain $0 < x < L, -\infty < y < +\infty$. Assume a periodic solution of the form

$$p^\pm(x, y) = \phi^\pm(x)e^{\pmily}, \quad (3.6)$$

Such that the full solution is $p(x, y) = p^+(x, y) + p^-(x, y)$. Then plug [Equation 3.6](#) into [Equations 3.5a–c](#). Using the fact that $a \sin (ly) = \frac{ia}{2}(e^{-ily} - e^{+ily})$, the following pair of boundary value problems is obtained:

$$\phi_{xx}^\pm \mp \frac{il}{k}\phi^\pm = 0 \quad (3.7a)$$

$$\phi_x^\pm(0) = 0 \quad (3.7b)$$

$$\phi^\pm(L) = \mp \frac{ia}{2} \quad (3.7c)$$

We solve the problems for the unknowns ϕ^+ and ϕ^- separately. The general solution for the ϕ^+ problem has the form

$$\phi^+(x) = C_1 e^{\sqrt{\frac{il}{k}}x} + C_2 e^{-\sqrt{\frac{il}{k}}x}. \quad (3.8)$$

Using boundary condition [3.7b](#), it follows that $C_1 = C_2$. For a non-trivial solution, we must have $C_1 = C_2 \neq 0$. Next, using boundary condition [3.7c](#) yields

$$C_1 = C_2 = -\frac{ia}{2}(e^{\sqrt{\frac{il}{k}}L} + e^{-\sqrt{\frac{il}{k}}L})^{-1}. \quad (3.9)$$

Plugging [Equation 3.9](#) into [Equation 3.8](#) gives the solution for ϕ^+ :

$$\phi^+(x) = -\frac{ia}{2} \left(\frac{e^{\sqrt{\frac{il}{k}}x} + e^{-\sqrt{\frac{il}{k}}x}}{e^{\sqrt{\frac{il}{k}}L} + e^{-\sqrt{\frac{il}{k}}L}} \right). \quad (3.10)$$

The general solution for the ϕ^- problem has the form

$$\phi^-(x) = C_3 e^{-i\sqrt{\frac{l}{k}}x} + C_4 e^{i\sqrt{\frac{l}{k}}x} \quad (3.11)$$

Using boundary condition 3.7b, it follows that $C_3 = C_4$. As in the previous case, a non-trivial solution requires $C_3 = C_4 \neq 0$. Boundary condition 3.7c then yields

$$C_3 = C_4 = \frac{ia}{2} (e^{-i\sqrt{\frac{l}{k}}L} + e^{i\sqrt{\frac{l}{k}}L})^{-1}. \quad (3.12)$$

Plugging Equation 3.12 into Equation 3.11 gives the solution for ϕ^- :

$$\phi^-(x) = +\frac{ia}{2} \left(\frac{e^{-i\sqrt{\frac{l}{k}}x} + e^{i\sqrt{\frac{l}{k}}x}}{e^{-i\sqrt{\frac{l}{k}}L} + e^{i\sqrt{\frac{l}{k}}L}} \right). \quad (3.13)$$

Adding together the separate solutions for p^+ and p^- results in the full solution for $p(x, y)$, *i.e.*,

$$p(x, y) = \frac{ia}{2} \left[\left(\frac{e^{+ibx} + e^{-ibx}}{e^{+ibL} + e^{-ibL}} \right) e^{-ily} - \left(\frac{e^{+bx} + e^{-bx}}{e^{+bL} + e^{-bL}} \right) e^{+ily} \right], \quad (3.14)$$

with $b \equiv \sqrt{il/k} = (1+i)\sqrt{l/(2k)}$. Manipulating the exponents in Equation 3.14:

$$p(x, y) = \frac{ia}{2} \left[\left(\frac{e^{+(1-i)qx} + e^{-(1-i)qx}}{e^{+(1-i)qL} + e^{-(1-i)qL}} \right) e^{-ily} - \left(\frac{e^{+(1+i)qx} + e^{-(1+i)qx}}{e^{+(1+i)qL} + e^{-(1+i)qL}} \right) e^{+ily} \right]. \quad (3.15)$$

Or, in a more compact form,

$$p(x, y) = \frac{ia}{2} \left\{ \left[\frac{\cosh(\bar{z}qx)}{\cosh(\bar{z}qL)} \right] e^{-ily} - \left[\frac{\cosh(zqx)}{\cosh(zqL)} \right] e^{+ily} \right\}. \quad (3.16)$$

with $z \equiv (1+i)$, $\bar{z} \equiv (1-i)$ and $q \equiv \sqrt{l/(2k)} = \sqrt{-lfs/(2r)}$, recalling that $k \equiv -r/(fs)$. We note that the e -folding scale of p in the cross-shelf direction (the real quantity q) depends not only on the conductivity parameter (k), but also on the wavenumber of the forcing (l). q does not depend on the amplitude of the forcing (a). It is seen that the distance q^{-1} scales the onshore extent of the deep-ocean influence in the case of periodic forcing at the shelf edge. This result is analogous to that of the periodic along-shelf wind stress ATW problem,

where l represents the along-shelf wavenumber of the along-shelf wind stress field (Csanady, 1978; Winant, 1979).

The choice of parameters a, l, f, s, r and L (Table 3.1) was guided by the numerical solutions from experiment EXP-smoo-2¹ (Chapter 2) and the approximate geometry of the TB shelf. Although the solution is meridionally infinite, the finite shelf length L^y considered here is intended to roughly match that of the TB shelf. The choice of pressure amplitude a corresponds to a reference amplitude of the numerical pressure gradient force ($6.9 \times 10^{-7} \text{ m s}^{-2}$). The along-shelf wavenumber $l = 3\pi/L^y \text{ m}^{-1}$ is set so as to simulate the numerical shelf edge pressure field (Figure 3.1). The linear drag coefficient r is picked from a range that has been found to agree well with observations (e.g., Pringle, 2002). The predicted cross-shore scale of deep-ocean influence associated with these parameters is $q^{-1} = \sqrt{-2r/(lfs)} = 10 \text{ km}$. For reference, the internal Rossby radius of deformation at the 70 m isobath is $L_d = NH/f = 18 \text{ km}$, using the mean N value for the TB shelf obtained in Chapter 2 (see Table 2.2).

The ATW solutions for the pressure and flow fields are shown in Figure 3.2. The form of the solution is a mirror image of the solution to the periodic along-shelf wind stress ATW problem. The alternating high and low pressure centers are associated with bands of onshore and offshore flow, which cause onshore transport of oceanic water through preferential pathways on the shelf. The flow field is slanted in the direction of propagation of long coastal trapped waves (hereafter the downwave direction).

Table 3.1: Parameters used in the ATW model.

Parameter	Value
a	-16 N m^{-2}
l	$4.42 \times 10^{-5} \text{ m}^{-1}$
f	$-5.10 \times 10^{-5} \text{ s}^{-1}$
s	2.68×10^{-3}
r	$3 \times 10^{-4} \text{ m s}^{-1}$
L	25 km
L^y	214 km

¹See Figure 2.15 for an example of the shelf-wide spreading of the periodic along-isobath pressure gradient force.

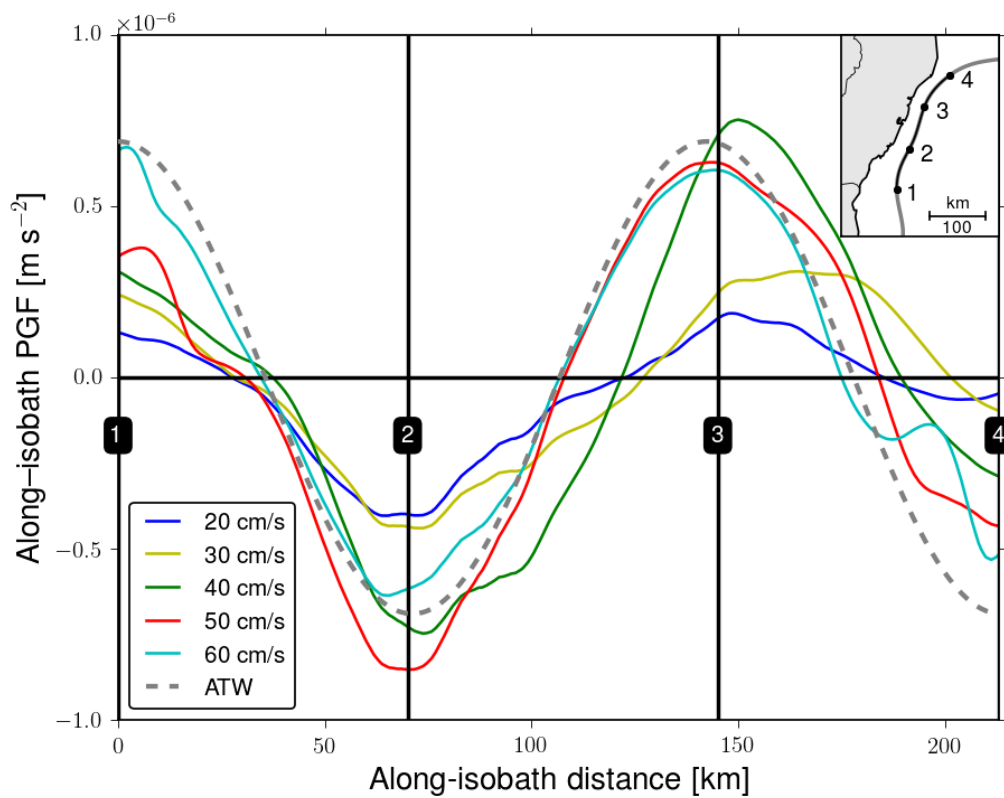


Figure 3.1: Numerical time-averaged (30 days) depth-averaged along-isobath Pressure Gradient Force (PGF) at the shelf edge (70 m isobath) as a function of along-isobath distance. Each line represents a numerical solution for a different Brazil Current (BC) core velocity. The gray dashed line is a least-squares sinusoidal fit representing the idealized forcing prescribed at the shelf edge of the ATW model. The vertical lines labelled 1–4 indicate along-isobath locations, which correspond to the numbered dots on the map insert.

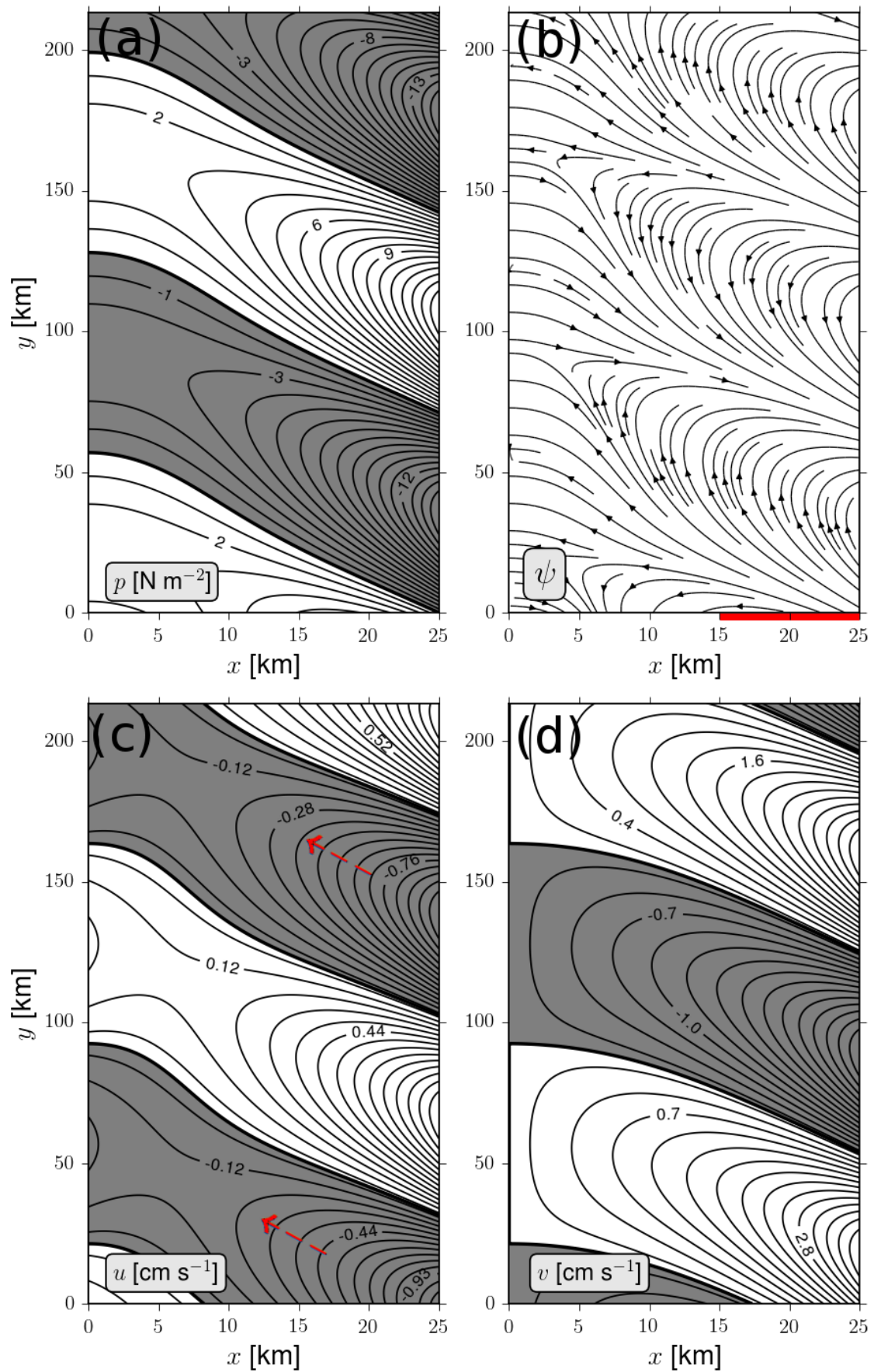


Figure 3.2: Solution to the Arrested Topographic Wave problem (Equation 3.16). **(a):** Pressure $p(x, y)$. **(b):** Streamlines. The red bar in the lower right corner indicates the cross-shore length scale of deep-ocean influence $\sqrt{-2r/(lfs)} = 10$ km predicted by the ATW model. **(c):** Cross-shelf velocity $u(x, y)$. **(d):** Along-shelf velocity $v(x, y)$. The red arrows indicate areas of onshore transport of water supplied at the shelf edge.

3.3 Comparison with primitive–equation numerical solutions

We begin with a qualitative comparison between the ATW solution and the numerical solutions from Chapter 2. Figure 3.3 shows the time–averaged depth–averaged flow field from an experiment with a simplified (smoothed) topography, no wind forcing and a BC jet flowing along the shelf edge. The flow pattern on the shelf bears qualitative similarities with the ATW solution (Figure 3.2), in that there are closed streamlines and the isotachs are slanted in the downwave direction.

As a consequence of the periodic nature of the forcing, any quantitative comparison of shelf–averaged quantities is highly sensitive to the choice of along–shelf averaging length (assuming the wavenumber l of the forcing is held fixed). We therefore compare the analytical and numerical solutions in terms of the cross–shelf penetration scales. Figure 3.4 shows two examples of cross–shelf profiles of depth–averaged cross–isobath velocity (u), and the associated exponential fits. The length scale $q^{-1} = \sqrt{2k/l} = \sqrt{-2r/(lfs)}$ predicted by the ATW for values of the linear bottom friction parameter r in the canonical range $2\text{--}5 \times 10^{-4} \text{ m s}^{-1}$ (e.g., Pringle, 2002) is consistent with the numerical results in terms of order of magnitude.

For a bulk comparison, we averaged all of the fit e –folding scales for each of the ten cross–shelf lines in Figure 3.3b to obtain a mean value and a standard deviation for each BC flow amplitude. Figure 3.5 shows that q has a poorly defined decreasing dependence on the forcing amplitude, meaning that a stronger incoming BC flow tends to penetrate farther onshore. Predictions for q underestimate the numerical exponential fits by $\approx 0\text{--}40\%$, with better agreement obtained under stronger forcing. Evidently, the non–constancy of the numerical penetration scales is partly attributable to the complexity of the primitive–equation model.

Another important source of disagreement, however, is that the numerical solutions use a quadratic bottom stress parameterization, meaning that the equiva-

lent of the linear bottom friction parameter r is the quantity $C_D U_{\text{bot}}$, where C_D is a unitless quadratic bottom friction parameter (set to 3.0×10^{-3} in the numerical solutions) and U_{bot} is the near-bottom velocity magnitude. Physically, this means that the predicted onshore penetration scale becomes a function of the forcing amplitude (*i.e.*, the BC core velocity). This new penetration scale is thus

$$q_{\text{quadratic}}^{-1} = \sqrt{\frac{-2C_D}{lf_s}} \times \sqrt{U_{\text{bot}}}, \quad (3.17)$$

meaning that the onshore extent of deep-ocean influence over the shelf increases with the square root of U_{bot} . Assuming for simplicity that U_{bot} is proportional to the BC core velocity, we used Equation 3.17 to estimate the predicted increments in $q_{\text{quadratic}}$ (relative to the first numerical solution, with a BC core velocity of 20 cm s^{-1}) and compared the result to the numerical e -folding scales (Figure 3.5).

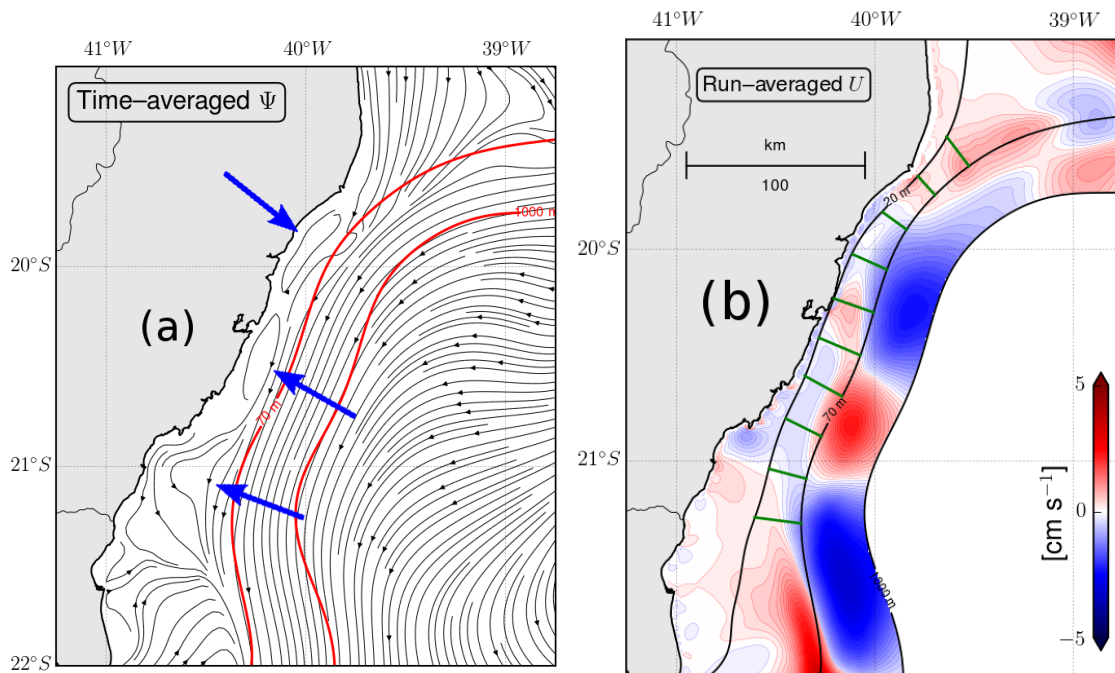


Figure 3.3: Time-averaged (30 days) flow fields from the numerical solution with a 60 cm s^{-1} BC. **(a)**: Depth-averaged velocity streamlines. The blue arrows indicate closed-cell circulation features on the shelf. **(b)**: Depth-averaged cross-isobath velocity U . Blue means onshore flow, red means offshore flow. Note the slant of the isotachs in the direction of long coastal trapped wave propagation (*i.e.*, equatorward). The green lines indicate the cross-shelf profiles used to estimate the numerical cross-shelf e -folding scales.

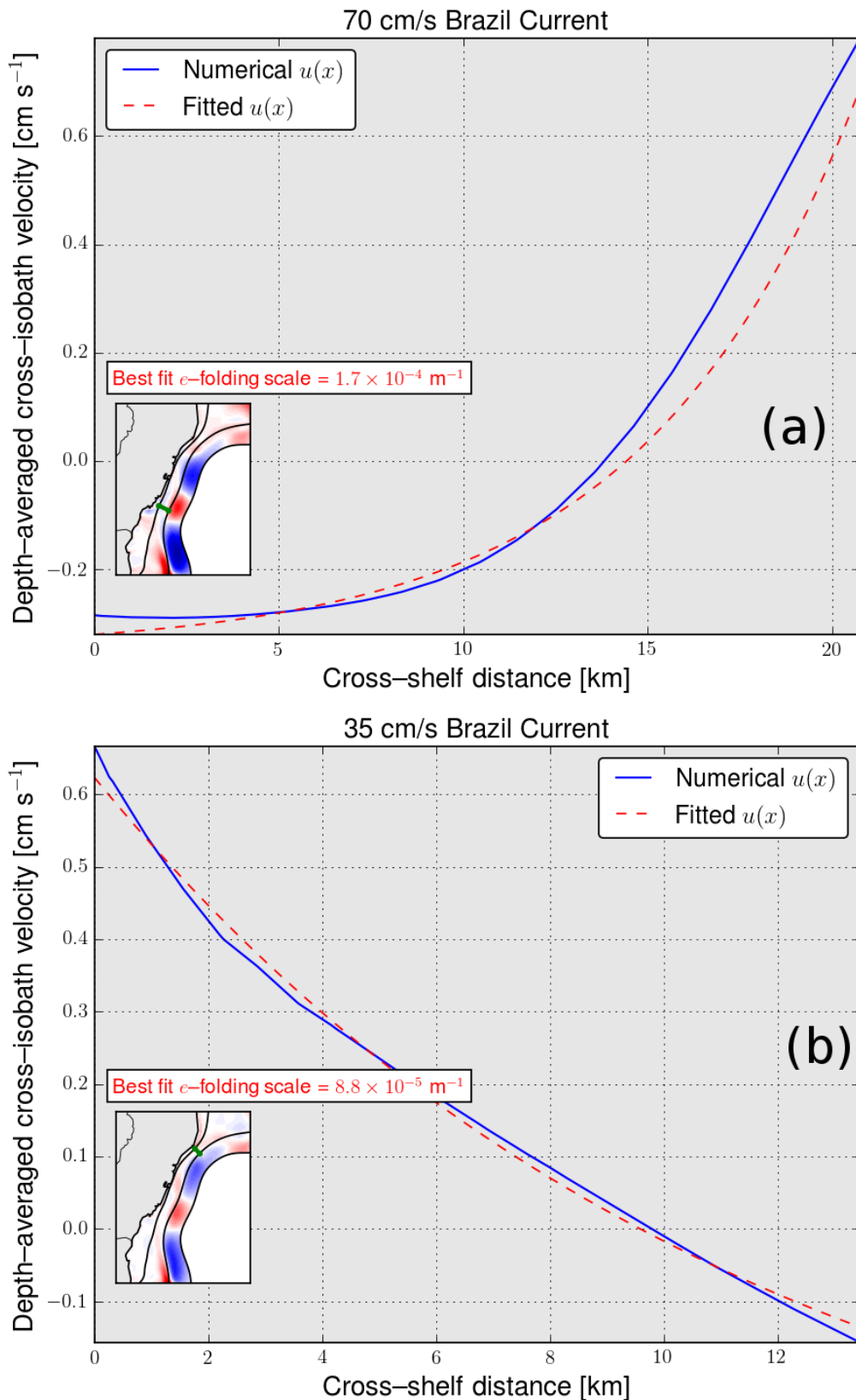


Figure 3.4: Examples of cross-shelf profiles of depth-averaged, cross-isobath velocity from the time-averaged (30 days) numerical solutions (blue lines) and associated exponential fits (dashed red lines). The numerical e -folding scales estimated with a nonlinear least-squares technique are shown. The range of e -folding scales $q = \sqrt{l/(2k)}$ predicted by the analytical model is $7.8 \times 10^{-5} \text{ m}^{-1}$ – $1.2 \times 10^{-4} \text{ m}^{-1}$, considering a canonical range for the linear bottom friction parameter $r = 2$ – $5 \times 10^{-4} \text{ m s}^{-1}$. The map inserts show the location of each cross-shelf profile (green lines) and the spatial distribution of u (color shading). Blue means onshore flow, red means offshore flow. **(a)**: 70 cm s^{-1} BC, south line. **(b)**: 35 cm s^{-1} BC, north line.

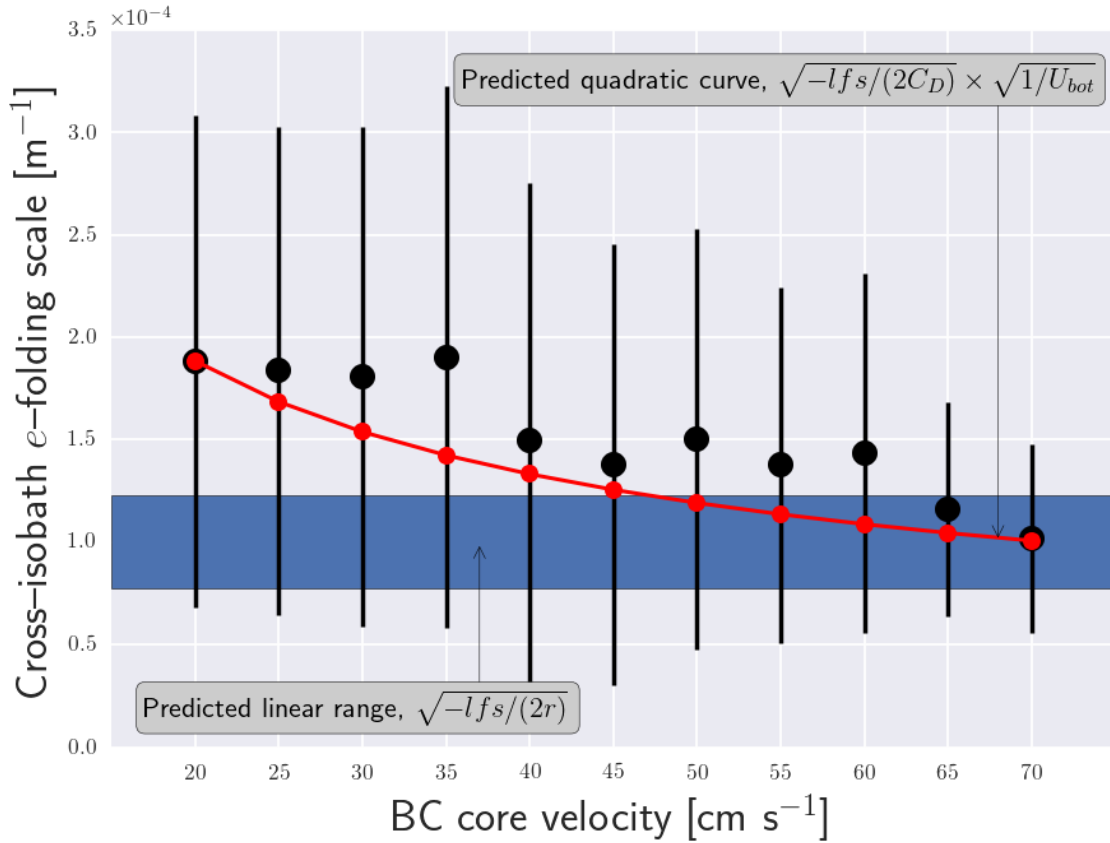


Figure 3.5: Shelf-averaged cross-shelf e -folding scales for cross-shelf velocity (black dots) estimated from the numerical solutions as a function of forcing amplitude (Brazil Current core velocity). The error bars indicate one standard deviation above and below each mean. The blue shading marks the analytical predicted range of linear onshore penetration scales $q = \sqrt{l/(2k)} = \sqrt{-lfs/(2r)}$, considering a canonical range for the linear bottom friction parameter $r = 2\text{--}5 \times 10^{-4} \text{ m s}^{-1}$. The red dots mark the analytical curve of quadratic onshore penetration scales $q_{\text{quadratic}} = \sqrt{-lfs/(2C_D)} \times \sqrt{1/U_{\text{bot}}}$, where $C_D = 3.0 \times 10^{-3}$ is the quadratic bottom friction parameter used in the numerical solutions and U_{bot} is the magnitude of the near-bottom velocity (assumed to be equal to the model BC core velocity for simplicity). $q_{\text{quadratic}}$ represents increments relative to the first numerical e -folding scale ($U_{\text{bot}} = 20 \text{ cm s}^{-1}$) rather than absolute values. Representative values for the TB are used: Bottom slope $s = 2.68 \times 10^{-3}$, inertial frequency $f = -5.10 \times 10^{-5} \text{ s}^{-1}$, and an along-shelf wavenumber $l = 4.42 \times 10^{-5} \text{ m}^{-1}$ for the forcing at the shelf edge.

3.4 Conclusions

Process-oriented numerical experiments discussed in [Chapter 2](#) revealed a time-mean periodic pressure field along the shelf edge in the TB area. Here, we presented evidence suggesting that the steady response of the coastal circulation to this deep-ocean forcing imparted by the BC can be rationalized as a manifestation of the physics contained in a simple ATW model. The use of quadratic bottom stress in the ATW onshore penetration scale expression accounts for some of the decrease of the numerical e -folding scales, improving the agreement between the analytical predictions and the numerical solutions. The weak, shelf-wide ≈ 0.2 – 1.0 cm s^{-1} cross-isobath ATW circulation could account for part of the onshore transport of cold, nutrient-rich SACW all the way to the inner shelf, provided that other physical processes have already transported it across the shelfbreak (*e.g.*, inertial overshooting of the BC). This process could therefore be an additional supporting mechanism to the more energetic wind-driven cross-shelf circulation of SACW in the TB.

Chapter 4

Final remarks

4.1 Thesis summary

This thesis investigates the pathways of and the physical mechanisms associated with the intrusions of South Atlantic Central Water (SACW) onto the Espírito Santo Basin (ESB) shelf (18°S–22°S, Brazil) by employing a combination of observational, numerical and analytical approaches to distill the physical basis of the phenomenon. In [Chapter 2](#), a set of simplified, process-oriented, primitive-equation numerical experiments is used in conjunction with a more complete numerical model and available observations to disentangle the kinematics and dynamics underlying the SACW intrusions. It is found that wind drives the shelf circulation at leading order, in accord with previous findings. Preferential pathways of SACW intrusion are recognized in the model experiments off Aracruz ($\approx 20^\circ\text{S}$, where the shelf is narrowest) and in the area between Marataízes and Cape São Tomé (21°S–22°S). These locations are collocated with areas where an equatorward along-isobath pressure gradient force (PGF_{y^*}) consistently forms at the shelf edge in both the simplified and realistic model experiments. The PGF_{y^*} is found to be nearly in geostrophic balance and to spread over most of shelf, thereby accelerating a geostrophic onshore flow. The along-isobath geostrophic balance is modified by nonlinear momentum advection at mid-depth and by friction within the bottom Ekman layer. Typical magnitudes for the model time-mean, depth-averaged PGF_{y^*} are $5 \times 10^{-7} \text{ m s}^{-2}$ – $5 \times 10^{-6} \text{ m s}^{-2}$, associated with

onshore velocities of $\approx 1\text{--}5 \text{ cm s}^{-1}$. Buoyancy arrest might be important during vigorous SACW intrusions, owing to the observed range of values for the slope Burger number¹ (0.32–0.92). Three higher-order deep-ocean physical processes are identified and quantified. Specifically, the intrinsic thermocline uplifting effect of the model Brazil Current (BC) is found to bring $\approx 1.4^\circ\text{C}$ colder water to the surface under steady, upwelling-favorable wind forcing (relative to a flat, BC-free scenario). Moreover, the $\approx 0.3\text{--}0.5$ values estimated for the Rossby number along the shelf edge suggest that the BC is prone to inertial overshooting, giving rise to local intrusions of SACW at the shelf edge. Finally, the planetary β -effect is estimated to account for an additional background $O(10^{-7} \text{ m s}^{-2})$ equatorward PGF_{y^*} along the shelf edge.

In [Chapter 3](#), the question of the onshore transmission of the time-mean pressure perturbations imparted by the BC at the shelf edge is further examined under the framework of an analytical Arrested Topographic Wave (ATW) model. Comparison with the primitive-equation numerical solutions discussed in [Chapter 2](#) suggests that the physics contained in the ATW model is indeed a plausible rationalization for most of the features obtained in the numerical solutions. Specifically, the cross-shelf e -folding scales estimated from the numerical solutions are found to agree in order of magnitude with the cross-shelf onshore penetration scale $\sqrt{-2r/(lfs)} = 10 \text{ km}$ predicted by the ATW, where r is a linear bottom resistance parameter, l is the along-shelf wavenumber of the shelf edge forcing, f is the Coriolis parameter and s is the bottom slope. The numerical penetration length scales are found to generally increase with BC amplitudes. Best agreement between numerical and theoretical penetration scales are found for stronger ($>60 \text{ cm s}^{-1}$) BC core velocities. Furthermore, agreement improves when quadratic bottom stress is introduced. In the quadratic case, the relative increase in the numerical onshore penetration scales is roughly predicted. The quadratic cross-shelf length scale becomes $q_{\text{quadratic}}^{-1} = \sqrt{-2C_D/(lfs)} \times \sqrt{U_{\text{bot}}}$, where C_D is a quadratic bottom friction parameter and U_{bot} is a near-bottom velocity magnitude.

¹The slope Burger number can be defined as $S \equiv \alpha N/f$, where α is the bottom slope, N is the stratification frequency and f is the Coriolis parameter.

4.2 Future work

The regional picture that emerges from this study is that of a scale-dependent cross-isobath coastal circulation, which is wind-driven at leading order, but modulated by deep-ocean processes at next order. Further investigation of a number of open questions is key to better understanding, modeling and predicting the regional coastal ocean in the Espírito Santo Basin. Some of the questions that future work on this subject should address are:

1. *How important to the South Atlantic Central Water intrusions is the Brazil Current mesoscale eddy field in the Espírito Santo Basin? What are the physical mechanisms involved?*
2. *What is the role of coastal-trapped waves in the cross-shelf circulation in the Espírito Santo Basin? Are there important resonant effects with the deep-ocean forcings?*
3. *What is the effect of internal waves in the intrusions of South Atlantic Central Water in the Tubarão Bight?*
4. *Does buoyancy arrest inflict strong constraints on intrusions of South Atlantic Central Water in the Espírito Santo Basin?*
5. *What are the physical mechanisms involved in the intrusions of Tropical Water in the Espírito Santo Basin?*
6. *Are cross-shelf intrusions and extrusions in the Espírito Santo Basin associated with submesoscale processes (e.g., mixed layer instabilities and filaments) comparable in magnitude with their mesoscale counterparts?*

Finding answers to these questions will probably entail a variety of methods. Personally, I feel that the thoughtful combination of process-oriented primitive-equation numerical modeling and observations (both *in situ* and remote) is a powerful approach for developing a mechanistic view of the core physics of a system, which may in turn be rationalized in terms of much simpler models.

Bibliography

- Aguiar, A., M. Cirano, J. Pereira, & M. Marta-Almeida (2014), Upwelling processes along a western boundary current in the Abrolhos–Campos region of Brazil, *Cont. Shelf Res.*
- Allard, P. (1955), Anomalies dans les températures de l'eau de la mer observées au Cabo Frio au Brésil, *Bull. Inf. Com. cent. Océanogr. Étude Côtes*, 7(2), 58–63.
- Arruda, W. Z., E. J. Campos, V. Zharkov, R. G. Soutelino, & I. C. Da Silveira (2013), Events of equatorward translation of the Vitória Eddy, *Cont. Shelf Res.*, doi: <http://dx.doi.org/10.1016/j.csr.2013.05.004>.
- Beckmann, A., & D. B. Haidvogel (1993), Numerical simulation of flow around a tall isolated seamount. Part I: Problem formulation and model accuracy, *J. Phys. Oceanogr.*, 23(8), 1736–1753.
- Boebel, O., R. Davis, M. Ollitrault, R. Peterson, P. Richardson, C. Schmid, & W. Zenk (1999), The intermediate depth circulation of the western south atlantic, *Geophys. Res. Lett.*, 26(21), 3329–3332.
- Bretherton, F. P., R. E. Davis, & C. Fandry (1976), A technique for objective analysis and design of oceanographic experiments applied to mode-73, em *Deep Sea Research and Oceanographic Abstracts*, vol. 23, pp. 559–582, Elsevier.
- Brink, K. H. (1998), Deep–sea forcing and exchange processes, em *The Sea*, vol. 10, Edited by K. H. Brink & A. R. Robinson, cap. 6, pp. 151–167, Wiley and Sons, New York.
- Brink, K. H. (2012), Buoyancy arrest and shelf-ocean exchange, *J. Phys. Oceanogr.*, 42(4), 644–658.
- Brink, K. H., & S. J. Lentz (2010), Buoyancy arrest and bottom Ekman transport. Part I: Steady flow, *J. Phys. Oceanogr.*, 40(4), 621–635.
- Calado, L., I. C. A. Silveira, A. Gangopadhyay, & B. M. Castro (2010), Eddy-induced upwelling off Cape São Tomé (22°S, Brazil), *Cont. Shelf Res.*, 30(10–11), 1181–1188.
- Campos, P. C., O. Möller, A. R. Piola, & E. D. Palma (2013), Seasonal variability and coastal upwelling near Cape Santa Marta (Brazil), *J. Geophys. Res.*, 118(3), 1420–1433, doi:10.1002/jgrc.20131.
- Carbonel, C. A. A. H. (2003), Modelling of upwelling–downwelling cycles caused by variable wind in a very sensitive coastal system, *Cont. Shelf Res.*, 23, 1559–1578.

- Casey, K. S., T. B. Brandon, P. Cornillon, & R. Evans (2010), The past, present, and future of the avhrr pathfinder sst program, em *Oceanography from Space*, Edited by V. Barale, J. Gower, & L. Alberotanza, pp. 273–287, Springer, doi: 10.1007/978-90-481-8681-5_16.
- Castelão, R. M., & J. A. Barth (2006), Upwelling around Cabo Frio, Brazil: The importance of wind stress curl, *Geophys. Res. Lett.*, 33.
- Castelão, R. M. (2012), Sea surface temperature and wind stress curl variability near a cape, *J. Phys. Oceanogr.*, 42(11), 2073–2087.
- Castro, B. M., & L. B. Miranda (1998), Physical Oceanography of the Western Atlantic Continental Shelf located between 4°N and 34 °S, em *The Sea*, vol. 11, Edited by A. R. Robinson & K. H. Brink, cap. 8, pp. 209–251, John Wiley and Sons.
- Castro, B. M., J. A. Lorenzetti, I. C. A. Silveira, & L. B. Miranda (2006), O Ambiente Oceanográfico da Plataforma Continental e do Talude na Região Sudeste-Sul do Brasil, 1st ed., cap. 1, pp. 11–120, Edusp, in Portuguese.
- Castro, B. M., M. Dottori, & A. F. Pereira (2013), Subinertial and tidal currents on the Abrolhos Bank shelf, *Cont. Shelf Res.*, 70, 3–12.
- Cerda, C., & B. M. Castro (2014), Hydrographic climatology of South Brazil Bight shelf waters between Sao Sebastiao (24°S) and Cabo Sao Tome (22°S), *Cont. Shelf Res.*, 89, 5–14.
- Charney, J. G. (1955), The gulf stream as an inertial boundary layer, *Proc. Natl. Acad. Sci. U. S. A.*, 41(10), 731.
- Clarke, A. J., & K. Brink (1985), The response of stratified, frictional flow of shelf and slope waters to fluctuating large-scale, low-frequency wind forcing, *J. Phys. Oceanogr.*, 15(4), 439–453.
- Csanady, G. T. (1978), The arrested topographic wave, *J. Phys. Oceanogr.*, 8(1), 47–62.
- Csanady, G. T. (1982), *Circulation in the Coastal Ocean*, 1st ed., D. Reidel Publishing Company.
- Dottori, M., & B. M. Castro (2009), The response of the Sao Paulo Continental Shelf, Brazil, to synoptic winds, 59(4), 603–614.
- Emílsson, I. (1961), The shelf and coastal waters off Sourthern Brazil, *Bolm. Inst. Oceanogr.*, 11(2), 101–112.
- Evans, D. L., S. R. Signorini, & L. B. Miranda (1983), A note on the transport of the Brazil Current, *J. Phys. Oceanogr.*, 13(9), 1732–1738.
- Firing, E., J. Ranada, & P. Caldwell (1995), Processing ADCP data with the CODAS software system version 3.1, *Technical report*, Joint Inst. for Mar. and Atmos. Res./NODC, University of Hawaii at Manoa, Honolulu.
- Franchito, S. H., T. O. Oda, V. B. Rao, & M. T. Kayano (2008), Interaction between Coastal Upwelling and Local Winds at Cabo Frio, Brazil: An Observational Study, *J. Appl. Meteor. Climatol.*, 47, 1590–1598.

- Gaeta, S. A., J. A. Lorenzetti, L. B. Miranda, S. M. Susini-Ribeiro, M. Pompeu, & C. E. Araujo (1999), The Vitória Eddy and its relation to the phytoplankton biomass and primary productivity during the austral fall of 1995, *Arch. Fish. Mar. Res.*, 47(2/3), 253–270.
- Gan, J., A. Cheung, X. Guo, & L. Li (2009), Intensified upwelling over a widened shelf in the northeastern South China Sea, *J. Geophys. Res.*, 114(C9).
- Gan, J., H. San Ho, & L. Liang (2013), Dynamics of intensified downwelling circulation over a widened shelf in the northeastern South China Sea, *J. Phys. Oceanogr.*, 43(1), 80–94.
- Gangopadhyay, A., & A. Robinson (2002), Feature-oriented regional modeling of oceanic fronts, *Dynam. Atmos. Oceans*, 36(1), 201–232.
- Garrett, C., P. MacCready, & P. Rhines (1993), Boundary mixing and arrested Ekman layers: Rotating stratified flow near a sloping boundary, *Annu. Rev. Fluid. Mech.*, 25(1), 291–323.
- Gibbs, M. T., J. H. Middleton, & P. Marchesiello (1998), Baroclinic response of Sydney shelf waters to local wind and deep ocean forcing, *J. Phys. Oceanogr.*, 28(2), 178–190.
- Gill, A., & E. Schumann (1974), The generation of long shelf waves by the wind, *J. Phys. Oceanogr.*, 4(1), 83–90.
- Haney, R. L. (1991), On the pressure gradient force over steep topography in sigma coordinate ocean models, *J. Phys. Oceanogr.*, 21(4), 610–619.
- Houry, S., E. Dombrowsky, P. De Mey, & J.-F. Minster (1987), Brunt-Väisälä frequency and Rossby radii in the South Atlantic, *J. Phys. Oceanogr.*, 17(10), 1619–1626.
- Hsueh, Y., H.-J. Lie, & H. Ichikawa (1996), On the branching of the kuroshio west of kyushu, *J. Geophys. Res.*, 101(C2), 3851–3857.
- Ikeda, Y., L. B. Miranda, & N. J. Rock (1976), Observations on stages of upwelling in the region of Cabo Frio (Brazil) as conducted by continuous surface temperature and salinity measurements., *Bolm. Inst. Oceanogr.*, 23, 33–46.
- Large, W. G., & S. Pond (1981), Open Ocean Momentum Flux Measurements in Moderate to Strong Winds, *J. Phys. Oceanogr.*, 11, 324–336.
- Legeais, J.-F., M. Ollitrault, & M. Arhan (2013), Lagrangian observations in the intermediate western boundary current of the South Atlantic, *Deep-Sea Res.*, 85, 109–126.
- Lentz, S. J., & D. C. Chapman (2004), The Importance of Nonlinear Cross-Shelf Momentum Flux during Wind-Driven Coastal Upwelling, *J. Phys. Oceanogr.*, 34(11), 2444–2457.
- Locarnini, R., A. Mishonov, J. Antonov, T. Boyer, H. Garcia, O. Baranova, M. Zweng, C. Paver, J. Reagan, D. Johnson, et al. (2013), World ocean atlas 2013. vol. 1: Temperature, A. Mishonov, Technical Ed. NOAA Atlas NESDIS, 73, 40.

- Loder, J. W., W. C. Boicourt, & J. H. Simpson (1998), Western ocean boundary shelves coastal segment (w), em *The Sea*, vol. 11, Edited by K. H. Brink & A. R. Robinson, pp. 3–27.
- Lopes, R. M., & B. M. Castro (2013), Oceanography, ecology and management of Abrolhos Bank, *Cont. Shelf Res.*, 70(Complete), 1–2.
- Lozano, C. J., A. R. Robinson, H. G. Arango, A. Gangopadhyay, Q. Sloan, P. J. Haley, L. Anderson, & W. Leslie (1996), An interdisciplinary ocean prediction system: Assimilation strategies and structured data models, *Elsevier Oceanography Series*, 61, 413–452.
- Matano, R. P., & E. D. Palma (2008), On the upwelling of downwelling currents, *J. Phys. Oceanogr.*, 38(11), 2482–2500.
- Mazzini, P., & J. Barth (2013), A comparison of mechanisms generating vertical transport in the Brazilian coastal upwelling regions, *J. Geophys. Res.*, 118(11), 5977–5993.
- McCabe, R. M., B. M. Hickey, E. P. Dever, & P. MacCready (2015), Seasonal Cross-Shelf Flow Structure, Upwelling Relaxation, and the Alongshelf Pressure Gradient in the Northern California Current System, *J. Phys. Oceanogr.*, 45(1), 209–227.
- McTaggart, K. E., G. Johnson, M. Johnson, F. Delahoyde, & J. Swift (2010), Notes on CTD/O₂ data acquisition and processing using Sea-Bird hardware and software (as available), *Technical report*.
- Miller, R. N., R. P. Matano, & E. D. Palma (2011), Shelfbreak upwelling induced by alongshore currents: analytical and numerical results, *J. Fluid. Mech.*, 686, 239–249.
- Miranda, L., & B. Castro (1982), Geostrophic flow conditions of the Brazil Current at 19°S, *Cienc. Interam.*, 22(1-2), 44–48.
- Palma, E. D., & R. P. Matano (2009), Disentangling the upwelling mechanisms of the South Brazil Bight, *Cont. Shelf Res.*, 29(11), 1525–1534.
- Palma, E. D., R. P. Matano, & A. R. Piola (2008), A numerical study of the Southwestern Atlantic Shelf circulation: Stratified ocean response to local and offshore forcing, *J. Geophys. Res.*, 113(C11).
- Palóczy, A., I. C. A. Silveira, B. M. Castro, & L. Calado (2014), Coastal upwelling off Cape São Tomé (22°S, Brazil): The supporting role of deep ocean processes, *Cont. Shelf Res.*, 89, 38–50.
- Pereira, A. F., A. Belém, B. M. Castro, & R. Geremias (2005), Tide–topography interaction along the eastern Brazilian shelf, *Cont. Shelf Res.*, 25(12), 1521–1539.
- Pringle, J. M. (2002), Enhancement of Wind-Driven Upwelling and Downwelling by Alongshore Bathymetric Variability, *J. Phys. Oceanogr.*, 32(11), 3101–3112.
- Pringle, J. M., & E. P. Dever (2009), Dynamics of wind-driven upwelling and relaxation between Monterey Bay and Point Arena: Local-, regional-, and gyre-scale controls, *J. Geophys. Res.*, 114(C7).

- Rocha, C. B., I. C. Silveira, B. M. Castro, & J. A. M. Lima (2014), Vertical structure, energetics, and dynamics of the Brazil Current System at 22°S–28°S, *J. Geophys. Res.*
- Rodrigues, R. R., & J. A. Lorenzetti (2001), A numerical study of the effects of bottom topography and coastline geometry on the Southeast Brazilian coastal upwelling, *Cont. Shelf Res.*, 21, 371–349.
- Rodrigues, R. R., L. M. Rothstein, & M. Wimbush (2007), Seasonal variability of the South Equatorial Current bifurcation in the Atlantic Ocean: A numerical study, *J. Phys. Oceanogr.*, 37(1), 16–30.
- Roughan, M., & J. H. Middleton (2002), A comparison of observed upwelling mechanisms off the east coast of Australia, *Cont. Shelf Res.*, 22(17), 2551–2572.
- Schaeffer, A., M. Roughan, & B. D. Morris (2013), Cross-shelf dynamics in a western boundary current regime: Implications for upwelling, *J. Phys. Oceanogr.*, 43(5), 1042–1059.
- Schlichtholz, P. (2002), On a modified arrested topographic wave in Fram Strait, *J. Geophys. Res.*, 107(C11), 10–1.
- Schmid, C. (2014), Mean vertical and horizontal structure of the subtropical circulation in the South Atlantic from three-dimensional observed velocity fields, *Deep-Sea Res.*, 91, 50–71.
- Schmid, C., H. Schäfer, G. Podestà, & W. Zenk (1995), The Vitória eddy and its relation to the Brazil Current, *J. Phys. Oceanogr.*, 25(11), 2532–2546.
- Scott, J., & G. Csanady (1976), Nearshore currents off Long Island, *J. Geophys. Res.*, 81(30), 5401–5409.
- Shchepetkin, A. F., & J. C. McWilliams (2005), The regional oceanic modeling system (ROMS): a split-explicit, free-surface, topography-following-coordinate oceanic model, *Ocean Model.*, 9(4), 347–404.
- Silveira, I., J. Lima, A. Schmidt, W. Ceccopieri, A. Sartori, C. Francisco, & R. Fontes (2008), Is the meander growth in the Brazil Current system off Southeast Brazil due to baroclinic instability?, *Dynam. Atmos. Oceans*, 45(3), 187–207.
- Smith, W. H. F., & D. T. Sandwell (1997), Global sea floor topography from satellite altimetry and ship depth soundings, *Science*, 277(5334), 1956–1962.
- Soutelino, R., A. Gangopadhyay, & I. da Silveira (2013), The roles of vertical shear and topography on the eddy formation near the site of origin of the Brazil Current, *Cont. Shelf Res.*, 70, 46–60, doi:http://dx.doi.org/10.1016/j.csr.2013.10.001.
- Soutelino, R. G., I. C. A. Silveira, A. Gangopadhyay, & J. A. Miranda (2011), Is the Brazil Current eddy-dominated to the north of 20°S?, *Geophys. Res. Lett.*, 38(3), L03,607.
- Stech, J. L., & J. A. Lorenzetti (1992), The response of the South Brazil Bight to the passage of wintertime cold fronts., *J. Geophys. Res.*, 97(C6), 9507–9520.
- Stramma, L., & M. England (1999), On the water masses and mean circulation of the South Atlantic Ocean, *J. Geophys. Res.*, 104(C9), 20,863–20,883.

- Stramma, L., Y. Ikeda, & R. G. Peterson (1990), Geostrophic transport in the Brazil current region north of 20°S, *Deep-Sea Res.*, 37(12), 1875–1886.
- Talley, L. D., G. L. Pickard, W. J. Emery, & J. H. Swift (2011), *Descriptive physical oceanography: An introduction*, Academic press.
- Teixeira, C. E., G. C. Lessa, M. Cirano, & C. A. Lentini (2013), The inner shelf circulation on the Abrolhos Bank, 18°S, Brazil, *Cont. Shelf Res.*, 70, 13–26.
- Trenberth, K. E., W. G. Large, & J. G. Olson (1990), The mean annual cycle in global ocean wind stress, *J. Phys. Oceanogr.*, 20, 1742—1760.
- Vélez-Belchí, P., L. R. Centurioni, D.-K. Lee, S. Jan, & P. P. Niiler (2013), Eddy induced Kuroshio intrusions onto the continental shelf of the East China Sea, *J. Mar. Res.*, 71(1-2), 83–107.
- Walsh, J. J. (1988), *On the nature of continental shelves*, 508 pp., Academic Press New York.
- Wijesekera, H., J. S. Allen, & P. Newberger (2003), Modeling study of turbulent mixing over the continental shelf: Comparison of turbulent closure schemes, *J. Geophys. Res.*, 108(C3).
- Winant, C. D. (1979), Comments on “The Arrested Topographic Wave”, *J. Phys. Oceanogr.*, 9(5), 1042–1043.
- Xu, J., R. J. Lowe, G. N. Ivey, N. L. Jones, & R. Brinkman (2015), Observations of the shelf circulation dynamics along Ningaloo Reef, Western Australia during the austral spring and summer, *Cont. Shelf Res.*, 95, 54–73.
- Zhang, H., J. Bates, & R. Reynolds (2006), Assessment of composite global sampling: Sea surface wind speed, *Geophys. Res. Lett.*, 33(17), L17,714.
- Zweng, M., J. Reagan, J. Antonov, R. Locarnini, A. Mishonov, T. Boyer, H. Garcia, O. Baranova, D. Johnson, D. Seidov, & M. Biddle (2013), World ocean atlas 2013, volume 2: Salinity, S. Levitus, Ed., A. Mishonov Technical Ed.; NOAA Atlas NESDIS, 74, 39.